Evaluating The Response Of
Polyvinyl Toluene Scintillators
Used In Portal Detectors

THESIS

Kelly D. Rakes, Captain, USAF

AFIT/GNE/ENP/08-M04

DEPARTMENT OF THE AIR FORCE
AIR UNIVERSITY

AIR FORCE INSTITUTE OF TECHNOLOGY

Wright-Patterson Air Force Base, Ohio

AFIT/GNE/ENP/08-M04

EVALUATING THE RESPONSE OF POLYVINYL TOLUENE SCINTILLATORS USED IN PORTAL DETECTORS

THESIS

Presented to the Faculty

Department of Engineering Physics

Graduate School of Engineering and Management

Air Force Institute of Technology

Air University

Air Education and Training Command

In Partial Fulfillment of the Requirements for the

Degree of Master of Science in Nuclear Engineering

Kelly D. Rakes, BS

Captain, USAF

March 2008

AFIT/GNE/ENP/08-M04

EVALUATING THE RESPONSE OF POLYVINYL TOLUENE SCINTILLATORS USED IN PORTAL DETECTORS

Kelly D. Rakes, BS
Captain, USAF

Approved:

/signed/	25 Mar 2008
James C. Petrosky (Chairman)	Date
/signed/	25 Mar 2008
Larry W. Burggraf (Member)	Date
/signed/	25 Mar 2008
George John (Member)	Date

AFIT/GNE/ENP/08-M04

Abstract

The goal of this research work was to determine if there exists, and to what extent, variability in the pulse-height spectrum, and resolution produced by γ-photon induced scintillation events in polyvinyl toluene scintillators.

Scintillator panels of the same type as those used in portal detector units currently operated by the Department of Homeland Security, made of polyvinyl toluene and measuring $12 \times 15 \times 2$ in were purchased from three vendors. Each vendor supplied two scintillators, one wrapped by the vendor with aluminum foil coated mylar, and two unwrapped. The scintillators where exposed to an $\approx 8\mu Ci$ source collimated ^{137}Cs source which decays with a 662 keV γ-ray 85% of the time. A Hamamatsu R329-02 photomultiplier tube was optically mated to the 12×2 in surface of the scintillator. The pulse height spectrum was recorded with the source placed at different positions across the surface of the scintillator.

Analysis of the pulse height spectrum was performed to determine efficiency and resolution differences across the surface of the scintillation panels. The resolution was found to have values that ranged from 23% at the corner furthest from the PMT to 33% an inch away from the PMT. The absolute efficiency ranged from 0.02 to 0.027 % for the majority of the measurements. The location and height of the Compton edge had noticeable trends, with the height being the greatest at the center and dropping off on the sides, but the peak location having a maximum in the corner along the axis of the PMT.

Acknowledgements

I would like to acknowledge my advisor Dr. Petrosky for his challenging encouragement, guidance and great conversation.

Next, I would like to thank Dr. Burggraf for pragmatism about my misguided approaches.

Then I would like to thank Dr. John for helping me get started and giving me good feedback.

Additionally I would like to thank LTC Lagraffe for his excellent instruction.

Mr. Eric Taylor for his invaluable help around the lab.

And I would like to thank my wife who has put up with me not only for the last year and a half, but for the past thirteen years. Finally, my two boys that have been left wanting fatherly interaction for the past year and a half, and have grown immeasurably in my absence.

Kelly D. Rakes

Table of Contents

List of Figures

List of Tables

List of Symbols

List of Abbreviations

EVALUATING THE RESPONSE OF
POLYVINYL TOLUENE SCINTILLATORS
USED IN PORTAL DETECTORS

I. Introduction

It is the goal of this study to determine the existence and extent of differences in detection capabilities of polyvinyl toluene based scintillators produced from different manufacturers and between different samples from the same manufacturer. In support of that goal some background information on the development of scintillators is given here.

1.1 Background

Since the development of nuclear power the number of states and institutions possessing the technology to produce a nuclear device that could pose a threat to the national security of the United States has grown. Though the threat of nuclear war is perhaps less likely than it once was the availability of nuclear technology has not ended with the Cold War. The nefarious uses of nuclear technology are many: from the cloak and dagger style use of polonium-210 in the poisoning of Alexander Litvinenko [16], to dirty-bombs-style radiological dispersion devices(RDD), to nuclear bombs. The methods of using nuclear technology to do harm is as diverse as the imagination of those that would employ them.

Whether by intent or not, the consequences of nuclear technology are on a far grander scale than most. Compounding any physical effect there is a significant amount of anxiety that accompanies nuclear technology. The first introduction to nuclear technology is often in discussions of the intense destructive power it delivered

to Japan or within the context of accidents at Chernobyl or Three Mile Island. Independent of physical damage, or danger posed to the people or infrastructure of the United States, prudent stewardship of nuclear technology also includes stewardship of public opinion as well.

The primary roadblock to nuclear weapon development is in the availability of materials. Thus monitoring and regulation receive significant attention in US agencies, and especially the Department of Energy. Monitoring methods have, for a large part, depended on the integrity of those using and creating radiologic materials. The events of 9/11 and terrorist activities around the world lead one to believe that such honesty can not be assumed for all entities that own, or create nuclear material internationally. Thus the need to verify the disposition of cargo entering and leaving the borders.

The need to monitor the disposition of cargo entering and leaving the United States has been handed to the Department of Homeland Security. This task requires fast and accurate identification of radioactive sources of interest without hindering the transportation system. The number of cargo containers entering the U.S., is somewhere on the order of 16500 per day. The blockages created by a poorly designed radiologic monitoring procedure could produce significant constriction or blockage in the economic life giving flow of cargo from the ports of entry. Thus the need for monitoring must not place significant blockage in the cargo flow.

The ubiquity of radionuclides produce a large number of radiation sources, that can be found in commercial materials. Naturally-occurring sources of radiation are present all over the globe, and are dispersed about the globe fairly evenly. As a result, many industrial products contain significant quantities of radionuclides. Such industrial products include: coal, concrete, gypsum, fertilizer, kitty litter, ceramics, and granite, to list only a few. Further, a cardiac stress test typically administers 10-30 mCi ^{99m}Tc [11] which is virtually indistinguishable from uranium on some

spectrometers. These diverse criteria and detection needs imply the need for a robust and effective use of technology to monitor and detect radio-nuclides.

1.2 Problem Definition

1.2.1 Hypothesis. Polyvinyl toluene scintillators produced from different companies, or even produced from the same company with the same production processes may differ significantly in response. These differences can be observed in total counts and pulse height spectrum measured by an appropriately constructed measurement system.

1.3 Research Objectives

The objective of this research work was to:

1. Determine if there exists variability in the pulse-height spectrum for PVT grown by different methods and manufacturers.

2. Measure absolute efficiency of the detector system across the scintillator panel from two different manufacturers.

3. Measure the energy resolution across the scintillator panel from two different producers.

1.4 Scope

Measurements made in this work are limited to those that can be performed at of the Air Force Institute of Technology. No radiation sources were purchased for the completion of this work, which leaves the selection of measurement techniques to be determined somewhat by the performance of the scintillator and the equipment on hand. The measurements were conducted at ambient temperature. Several researchers have used the technique discussed by Clark [10] to measure intrinsic efficiency of the scintillators. This requires very active sources, the likes of which are not on hand at the Air Force Institute of Technology(AFIT).

1.5 Approach

The approach to this topic included the use of modeling, experiment, and theory validation. The modeling was completed using Geant4, a Monte Carlo based Tool-kit developed to simulate the effects of particles passing through matter. Specifically, it was used to simulate the passage of gamma-rays through the scintillator material, the production of Compton electrons, and the transport of the lower-energy scintillation photons through the scintillator. There is a large variety of information that accompanies the simulation. Only the energy and count data were used.

The experiments were designed to occur in phases. First, an experimental system was constructed. Second, the electronics where added. Once the electronics where assembled, sample scintillators where exposed to mono-energetic γ sources, and an energy pulse height spectrum acquired. The supply voltage was adjusted to determine an optimal operating voltage for each photomultiplier tube (PMT). Third, the gain settings on the various circuits where adjusted to place the Compton edge at channel 507 out of 8191. Finally, scintillator panels where added to the system and the photomultiplier tubes optically mated to the small face of the panel with the gain settings being modified to bring the voltage higher.

The scintillator panel's composition matched those used in portal detector units purchased by the Department of Homeland Security. They are polyvinyl with small amounts of light-producing compounds. They were cast, cut, and polished to produce panels measuring $12 \times 15 \times 2$ in. Two vendors supplied three scintillator panels each. One was wrapped by the vendor with aluminum and then coated with Mylar, and two were unwrapped. The incident angle of mono-energetic γ-photons was reduced using a collimator constructed of Cerrobend®, to yield a solid angle of 0.553 steradians and area of 1.26 cm^2 at the surface of the scintillator. Spectrographic measurements where completed and the pulse height spectrum analyzed to determine resolution and absolute efficiency by moving the collimator to different positions on the scintillator panel. Application of statistical techniques were applied to ascertain

variations in efficiency across the scintillator between different scintillators from the same producer and between producers.

1.6 Assumptions

1. Ambient light contributions to the counts recorded were sufficiently suppressed with the experimental setup so they had consistent, negligible effect on the pulse height spectrum.

2. The scintillator and photomultiplier tube's performance stays constant during the course of measurements on the single scintillator panel.

1.7 Results

The measurements of efficiency and resolution did not have sufficient repeatability to discriminate between scintillator panels. The resolution of the scintillators was found to vary spatially from a value of 23% when the source was adjacent to the PMT, and decreased with the distance from the photomultiplier tube. The poorest resolution was when the source was placed furthest from the photomultiplier tube and was found to be 40%. The efficiency varied spatially as a function of the proximity to a side, and distance from the photomultiplier tube. A partial understanding of the differences in efficiency and resolution can be grasped through the application of a light capture fraction factor.

1.8 Sequence of Presentation

This document is divided into six chapters with multiple appendices. The first chapter gives the background and discusses the problem statement. The second chapter reviews much of the published material relevant to the research. The third chapter covers the methodology used. The fourth chapter presents a subset of the results obtained, then chapter five holds a discussion on the trends, and six holds recommendations.

II. Literature Review

2.1 Purpose

Two questions are to be answered in the following literature search;

- Is there a deficiency in understanding of polyvinyl toluene's (PVT) response to gamma radiation sufficient to warrant further investigation?
- Does research already exist that precludes the need to conduct further research?

2.2 Measurment

The *dawn* of nuclear measurement began by measuring x-rays with a phosphorescent screen. In his work with Ernest Rutherford, Hans Geiger developed the gas filled detector, while working with W. Mueller he produced the instrument commonly known as the *Gieger Counter*. The *Gieger-Mueller* tube responds to the presence of ionizing radiation by giving an electrical pulse when radiation interacts with gas in the detector. In addition to identifying the presence of radiation, researchers also desired the ability to distinguish the energy of the radiation, leading to the development of ion chambers. The science of determining the energy of radiation came to be known as spectroscopy. The quest for improved resolution has produced several devices to suit this goal. Two main groups of device exist, semiconductors and scintillators. The semiconductors group produce an electrical signal when ionizing radiation interacts with the material. Scintillators produce light when ionizing radiation interacts with the material. The resulting scintillation light can then be converted to an electrical charge with a photo-multiplyer tube.

2.3 Scintillators

Scintillators are materials that produce light when exposed to radiation. According to Knoll [21], the ideal scintillator should have the following characteristics:

1. High efficiency for converting energy from radiation into scintillation light that can be detected by the photocathode of a photomultiplier.

2. Behave linearly to the quantity of energy that creates light.

3. Not absorb the scintillation light that it produces.

4. The induced luminescence should have a short decay time to facilitate timing applications.

5. Be of sufficient purity and absent of non-scintillating material, and producible in the size desired;

6. Have a refraction index that matches the Photomultiplier Tube.

The ability to meet the above criteria is a measure of the quality of the material for use as a scintillator. Scintillators can be broken into two groups, stemming from differences in their chemical makeup. First, inorganic scintillators are frequently alkali halides, the most widely used is sodium iodide (NaI). Inorganic scintillators tend to have linear response and superior light output when compared to organic scintillators. On the other hand they typically have slow response times. Organic scintillators make up the second group, they tend to have a lower light yield but faster response [21].

The first organic scintillator on record was crystal naphthalene, developed by Kallman and Broser in 1947. Many organic scintillators followed including pure crystal, liquid and plastic, with a variety of dopants to tailor the scintillator's response. Some of the common scintillator solvents and ingredients used in organic scintillators are given in Table 2. Some of the popular compositions are listed in Table 1. A notable entry in Table 2 is anthracene, because its light output has had extensive characterization and is a widely used benchmark. The fast response and low cost of production have made the organic scintillators such as polyvinyl toluene(PVT) a logical choice where large detectors are necessary. Several applications have employed organic scintillators with volumes as large as a 1 m^3 [36] and response times

Table 1: Some common plastic scintillator compositions [37]

Bulk	$1^{st} fluor$	$2^{nd} fluor$
Polystyrene	2% TP	0.1% POPOP
Polyvinyl xylene	2% TP	0.1% POPOP
Polyvinyl toluene	2% TP	0.1% POPOP
Polystyrene	1.5% TP	-
Polystyrene	1.5% DF	-
Polystyrene	1.5% BPO	-
Polystyrene	1.5% PPO	-
Polystyrene	1.5% BαNE	-
Polystyrene	1.5% BPO	-
Polystyrene	1.5% TP	-
Polystyrene	2.0% TP	0.1% POPOP
Polystyrene	2.0% TP	0.1% BBO
Polystyrene	2.0% TP	0.1% 3P-Δ^2
Polystyrene	2.0% TP	0.4% BBE

as low as $\sim$ 200 ns. As the size of a scintillator increases, so does the probability that incident radiation will interact and be measured.

2.4   PVT Uses

The application of PVT to different sensing needs is varied. The majority, 80%, of the plastic scintillator market is the general-purpose PVT scintillator [28] such as the BC-404 or EJ-204. The trade names and use of several common PVT scintillators, originating from two major producers, are presented in Table 3. These products are designed to minimize the attenuation of scintillation photons and have been used to make sensors that are more than a square meter in area. When doped with ^{10}B they can be employed as effective thermal neutron detectors. Pulse-shape discrimination can be used to distinguish between neutron and γ radiation as described in Pope's thesis [31]. Fast neutron detectors such as BC-720 are formulated to be transparent to γ-rays with a phosphor, ZnS[Ag], that responds to recoil protons produced from knock-on reactions. Other formulations for neutron detection exploit boron's large neutron cross section. The scintillation rise-times of BC-422,

Table 2:   A partial list of popular scintillator ingredients adapted from Brook's [36]

	Compound	Formula	Application[a]
1	Benzene	C_6H_6	S
2	Toluene	$C_6H_5(CH_3)$	S
3	p-Xylene	$C_6H_4(CH_3)_2$	S
4	1,2,4 Trimethylbenzene (psuedo-comene)	$C_6H_3(CH_3)_3$	S
5	Hexamethylbenzene	$C_6(CH_3)_6$	S
6	Styrene monomer	$C_6H_5(C_2H_3)$	S
7	Vinyltoluene monomer	$C_6H_4(CH_3)C_2H3$	S
8	Napthalene	$C_{10}H_8$	S',C
9	Anthracene	$C_{14}H_{10}$	C
10	Biphenyl	$C_{12}H_{10}$	S'
11	TP[p-Terphenyl]	$C_{18}H_{14}$	C,PS
12	p-Quarterpenyl	$C_{24}H_{18}$	C
13	trans-Stilbene	$C_{14}H_{12}$	C
14	Diphenylacetylene	$C_{14}H_{10}$	C
15	1,1',4,4'-tetraphenylbutadiene	$C_{28}H_{22}$	SS
16	Diphenylstilbene	$C_{26}H_{20}$	SS
17	PPO [2,5-diphenyloxazole]	$C_{15}H_{11}NO$	PS
18	α-NPO[2-(1-Naptyl),5-phenyloxazole]	$C_{19}H_{13}NO$	PS
19	PBD [2-Phenyl,5-(4-biphenylyl)-1,3,4-oxadiazole]	$C_{20}H_{14}N_2O$	PS
20	BBO[2,5-Di(4-biphenyl)-oxazole]	$C_{27}H_{19}NO$	SS
21	POPOP[1,4-Bis(2-(5-phenloxazolyl))-benzene]	$C_{24}H_{16}N_2O_2$	SS
22	TOPOT[1,4-Di-(2-(5-p-tolyloxazolyl))-benzene	$C_{26}H_{20}N_2O_2$	SS
23	BiMePOPOP [1,4-Di(2-(4-methyl-5-phenyloxazolyl))-benzene]	$C_{26}H_{20}N_2O_2$	SS
24	DF [2-(diethoxylphenyl)-5-phenyl-1,3,4-oxadiazole]		PS
25	BPO[2-phenyl-5-(4-biphenyl)-1,3-oxazole]		PS,SS
26	3P-Δ^2[1,3,5-triphenyl-Δ^2-pyrazoline]		SS
27	BBE[1,2-di-(4-biphenylol)-ethylene]		SS
28	BαNE[1-(4-biphenylyl)-2-(α-naphthyl-ethlene]		PS

[a] S-primary solvent; S'-secondary solvent; PS-Primary solute;
SS-secondary solute; C-crystal scintillator

2-3 nanoseconds, make it a natural choice for count-rate measurements. Spectral light collection applications make use of the BC-428 and BC-430 plastics because they have flourescent spectra at longer wavelengths than other plastic scintillators. The temperature resilience of BC-434 and BC-438 make them effective in elevated temperature environments. Other formulations include tin and lead in the mixture to increase sensitivity to x and γ-rays.

Table 3:   Commercial scintillators and usage

St Gobain	Eljen	St. Gobain-NE	Use
BC-400	EJ-212	NE-102A	general purposes, TOF counters, large area
BC-404	EJ-204	NE-104	general use
BC-408	EJ-200	Pilot F	thin films, general purpose, α, β, γ, fast neutrons
BC-412	EJ-208	NE-110	general purpose, large area, β
BC-416	EJ-208B	-	lower cost version of BC-412/EJ-208
BC-720	-	-	neutron detectors
BC-422	EJ-232	-	fast counting applications
BC-428,BC-430	-	-	light collection applications
BC-434,BC-438	EJ-248	-	high temperature operation

The Large Acceptance Spectrometer at T. J. Laboratory will use 4 m long BC-412 plastic scintillators. Massive $1 \times 1 \times 0.2$ meter plastic scintillators are being used to detect high energy neutrons via knock-on reactions of $^1H(n,p)$ and $^{12}C(n,p)$ [26]. The Northern Illinois Center for Accelerator and Detector Development (NICADD) proposed a detector for use in a future Linear Collider Detector (LCD) using a stack of twelve PVT scintillators that acts in a digital format providing energy resolution sufficient to determine the invariant masses of the hadronic final states of W and Z bosons [12]. Though the list in Table 1 is large, not all plastics make good scintillators. Though the application and composition of organic scintillators is varied, the scintillation process that results in measurable light is common.

2.5 Polyvinyl Toluene

PVT scintillators are made up of long chain vinyl toluene molecules. Toluene is a benzene ring bonded to a methyl(CH_3) and a vinyl group (CH_2-CH-) [35]. A common feature to most organic scintillators is the benzene ring. It is characterized by the delocalization of three π-bonds. The π-bonds give rise to a cloud of electrons above and below the molecular plane. The polyvinyl toluene molecules are oriented in the same direction and held together by van der Waals forces instead of existing in a well ordered crystal matrix and bound together with covalent bonds.

2.6 Scintillation In Organics

The first step in the scintillation process is the excitation of the PVT molecule.

2.7 Absorption

Aromatic hydrocarbons typically exhibit absorption in the visible and ultra-violet region of the spectrum via the excitation of singlet π-electron states. Three or more absorption bands are typical, corresponding to transitions from the singlet ground state to the excited π-electronic states. The intensity of the first transition $S_0 \rightarrow S_1$ is relatively small when compared to the $S_0 \rightarrow S_2$, and $S_0 \rightarrow S_3$. The relationship can be quantified using the correlation

$$I = I_0 10^{-\varepsilon c d} \tag{1}$$

where ε is the molar extinction coefficient, c is the molar concentration of absorbing species, and d is the thickness of the specimen. The first transition tends to be on the order of $\varepsilon \sim 10^3$ with $\varepsilon \sim 10^5$ for the second and third transitions.

2.8 Luminescence

After energy is absorbed it is emitted through several processes. The luminescence of simple organic molecules has three parts:

1. Fluorescence,

2. Phosphorescence,

3. Delayed Fluorescence.

2.8.1 Fluorescence. Fluorescence is the radiative transition after excitation from the first excited singlet π-state, S_1, to vibrational states of the π-electron ground state S_0 [8]. Though the absorption may be to any of a number of excited π-electron states, S_1, S_2, S_3 . . . as illustrated in the figure borrowed from Knoll's book on radiation detection [21], Figure 1(a), the radiative transitions are only seen from the S_1 state (Figure 1(c)). The absence of radiative transitions from the higher level singlet π-electron states are accounted for by a rapid, $\sim 10^{-10} sec$, and efficient non radiative internal conversion (Figure 1(b)). The internal conversion quickly drops the energy of the higher excited π-electron states to the S_{1n} excited state, with n representing a vibrational substate of the S_1 π-electron state. The more energetic vibrational states quickly lose their energy in $\sim 10^{-12}$ sec, and come to equilibrium to settle into the S_{10} state. Once in the S_{10} state the radiative lifetime is on the order of $\sim 10^{-8}$ to $\sim 10^{-9}$ sec. Fluorescence emission intensity decays from its original value according to (2),

$$I = I_0 e^{-t/\tau} \tag{2}$$

where I_0 and I are the initial intensity and intensity at a time t respectively, with τ being the fluorescence decay time. Transitions starting at the S_{10} level can end up at any of the the vibrational sub levels of the ground state, S_{00}, S_{01}, S_{02} and so on, making up the fluorescence spectrum. Commonly the fluorescence spectrum is a

mirror of the $S_0 \rightarrow S_1$ absorption spectrum. For wavelengths where absorption and emission can occur the scintillator will experience significant self absorption.
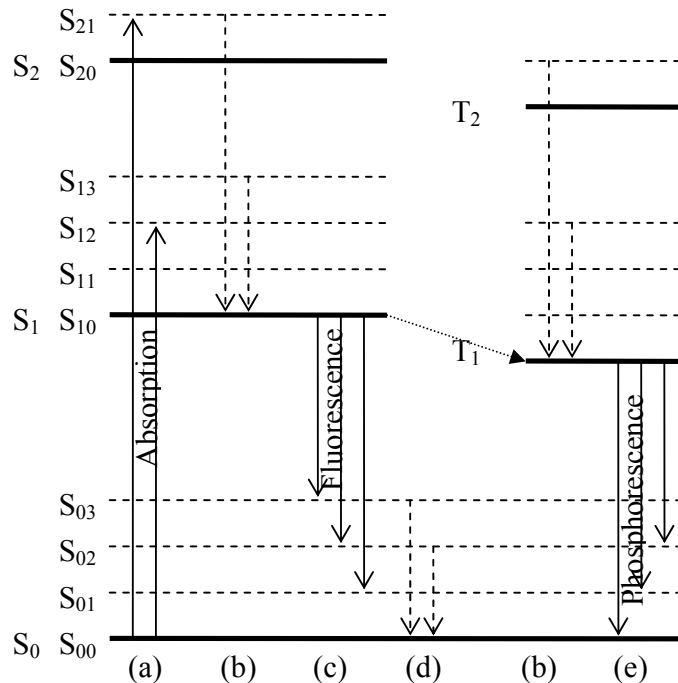
Figure 1: Diagram of energy transitions for polyvinyltoluene: Radiative transfer transitions are represented by solid lines; non-radiative transitions are represented by dashed lines, adapted from [21].

2.8.2 Phosphorescence and Delayed Fluorescence. Phosphorescence describes the process whereby a longer wavelength emission occurs with an exponential decay having a decay time of $\sim 10^{-4}$ sec or more. Delayed fluorescence has an identical spectrum to fluorescence, but does not obey exponential decay and has a longer decay period. Occasionally, a molecule that is in an excited singlet state, S_1, will transition into an excited triplet state, T_1, through a process known as inter-system crossing. The phosphorescence comprises the $T_1 \rightarrow S_0$ transition. The vibrational spectrum observable in phosphorescence is similar to that of fluorescence. As in the singlet states, the triplet states experience quick non-radiative decay to the lowest triplet state T_1(d). The decay of the excited triplet state is strongly forbidden and

14

gives rise to the long lived phosphorescence. Instead of direct decay the triplet state most frequently occurs via combination with another excited triplet state to produce an excited singlet state, a singlet ground state, and phonons as described in Equation 3.

$$T_1 + T_1 \longrightarrow S_1 + S_0 + phonons \tag{3}$$

2.8.3 Solutes. The wavelength of fluorescent emission from the organic solute is typically in the UV. The typical transition as shown in Figure 1 contains less energy than that required to excite an electron to an elevated state, making self-absorption improbable. Further, resistance to self-absorption can be created by adding up to 1% by weight of a "primary fluor" solute species. The transfer of energy to the lower energy excited state of the fluor allows for the re-radiation at a wavelength where the bulk material is more transparent [19]. Further, a second solute species is often added in lower concentrations $\approx 0.05\%$ by weight to further lengthen the wavelength of the fluorescence.

The efficiently-designed scintillator solution consists of one or more additional species, Y, into the solution to produce excited electronic states that are of lower energy than the excited states of the solvent. In these mixtures, the first steps of scintillation occur as they do in the pure organic, but when the excited S_1 and T_1 states are reached, the excited states of the solute compete for energy transfer represented by,

$$S_{X,1} + S_{Y,0} \longrightarrow S_{X,0} + S_{Y,1}, \tag{4}$$

$$T_{X,1} + S_{Y,0} \longrightarrow S_{X,0} + T_{Y,1}. \tag{5}$$
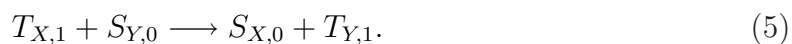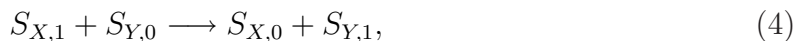
The transfer of energy occurs through the resonant dipole-dipole interactions [15] [33]. Any remaining vibrational energy decays to the lowest energy excited solute states, $S_{Y,1}$ and $T_{Y,1}$ respectively. The lowest energy singlet state promptly fluoresces, producing ground state solute molecule ,$S_{Y,1}$. The annihilation of the excited solute

15

triplet states occurs over a longer time period, and is like that of the solvent species resulting in an excited singlet state, $S_{Y,1}$, over a relatively long period of time [36].

The prompt decay can be represented by

$$P_Y(T) = \left[\frac{K}{K-1}\right]\left(e^{-T} - e^{-KT}\right),\tag{6}$$

where $T = t/\tau_{0Y}$, τ_{0Y} is the decay time of the solute $S_{Y,1}$, t is time. The ratio of extinction lifetimes K is $k_x\tau_{0Y} = \tau_{0Y}/\tau_x$ and

$$k_x = 1/\tau_x = 1/\tau_{0x} + k_{YX}[S_{Y,1}],\tag{7}$$

where $[S_{Y,1}]$ is the molar concentration of solute and the term $k_{YX}[S_{Y,1}]$ represent the rate of energy transfer depicted in Equation 4.

2.8.4 The Scintillation Process.   Consider a fast electron incident on an efficient scintillator that dissipates the whole of its energy, E, inside the scintillator. A fraction of that energy, S, is converted to N fluorescence photons with an average energy, E_p. The value S is the absolute scintillation efficiency.

The emission spectrum of a single component scintillator is equivalent to its fluorescence spectrum. In a binary system the energy from the excited solvent is transferred to the solute making the scintillation spectrum equal to the fluorescence spectrum of the solute. The designer of a multiple-component scintillator frequently adds multiple solutes so that energy is transferred to a molecule with the desired emission spectrum; usually well below the absorbtion spectrum of the bulk scintillator molecule.

The fluorescent time of a single component scintillator, apart from self-absorption, is approximately equal to that of the fluorescent decay arising from excitation via an ultraviolet source. For binary and ternary systems the emission timing is approximately that of the photofluorescence decay of the emitting solute [8]. The rise

16

time, however, may be lengthened, due to the finite time of energy transition from the solvent to the emitting species. The fast scintillation decay time is then on the order of 2 to 30 nsec [8]. For many scintillators about $\sim 10\%$ of the decay, is slow scintillation, and does not decay exponentially, having a duration that lasts $\sim 10^{-3}$ sec [36].

The number of scintillation photons produced is strongly dependant on the particle type and its energy. Heavy particles will damage the molecules of a scintillator as they interact with the scintillator. Multiple damaged molecules often combine locally to reduce the number of excited π-electron states in a process called quenching. If no quenching occurs the relationship between scintillation response and light yield can be represented by

$$\frac{dL}{dx} = S\frac{dE}{dx} \tag{8}$$

where L is the scintillation response and S is the absolute scintillation efficiency. An *ionization-quenching* effect occurs in plastic scintillators for heavy particles that create a large ion density. Non-linearities in response, L, arise from the non-linearity in energy loss dE/dx and ionization density from different particles and energies. A good model for this deviation from linearity is the introduction of the quenching term kB in the formula attributed to Birks [8]. The relation of light yield to energy loss is then

$$\frac{dL}{dx} = \frac{S\frac{dE}{dx}}{1 + kB\frac{dE}{dx}}, \tag{9}$$

with the kB term used as a fitting parameter. Further, a quadratic term has been suggested by Smith *et al.* to make Equation (10),

$$\frac{dL}{dx} = \frac{S\frac{dE}{dx}}{1 + kB\frac{dE}{dx} + C\left(\frac{dE}{dx}\right)^2}, \tag{10}$$

17

where both kB and C are used as fitting parameters. Ionization quenching makes the most dramatic impact on the intensity of the fast scintillation component, though there is a measurable effect on the slow component. Though energy loss does not effect timing, ionization potential does. The timing impact from ionization potential then translates to changes in the pulse shape and leads to the ability to discriminate between particles. This effect on timing then ultimately changes the pulse shape. The effects lead to techniques that can distinguish between incident particles based on the pulse shape, i.e. pulse-shape discrimination.

2.9 Solute Materials

Noting similarities between liquid and plastic scintillators Birks [8] identifies several primary fluors as p-terphenyl(TP), 2,5-diphenyloxazole (PPO), and 2-Phenyl,5-(4-biphenylyl)-1,3,4-oxadiazole(PBD). With effective secondary fluors being 1,4-Bis(2-(5-phenloxazolyl))-benzene(POPOP) as wavelength shifters. Notable differences are: that unlike the liquid cousins, plastic scintillators are somewhat dependant on the method used to prepare them. The quantum efficiency is appreciably higher in plastic scintillators than in liquids and higher solute concentrations are needed to get optimum efficiency. A comparison between the pulse heights produced by various sources in plastic and liquid is presented in Table 4.

Table 4:   Relative Scintillation Efficiency of Polystrene solutions [8]

γ-ray	E (MeV)	Plastic scintillator		Liquid scintillator	
		Pulse height of peak (arbitrary units)	Half - resolution $\eta_{1/2}$ %	Pulse height of peak (arbitrary units)	Half - resolution $\eta_{1/2}$ %
^{137}Cs	0.66	9.7	26	12.0	33
^{60}Co	1.17	21.3	26 (combined peak)	26.6	24 (combined peak)
	1.33				
^{40}K	1.46	26.1	14.5	32.4	16
^{22}Na	1.28			29.2	18.5
	0.51			8.4	43

18

The two standard solutes that are used to decrease the energy of fluorescent light are p-terphenyl as a primary, and 3-hydroxyflavone. Christian [14] mentions p-terphenyl, which increases the scintillation from high energy photons, and 1,4-bis(2-methylstyryl) benzene as a wavelength shifter. Some standard formulations are listed in Table 5. The attenuation of emitted light depends on the wavelength of the emission, and thus the attenuation length differs with species. A comparison of the attenuation effects on several compositions of scintillator was presented by Birk's and is recreated in Table 6.

Table 5: Comparison of most effective Organic Scintillators [8]

Solvent (or Crystal)	Primary solute (conc. g/l)	Secondary solute (conc. g/l)	Relative pulse height
Anthracene	-	-	100
trans-stilbene	-	-	82
PVT	TP(36)	DPS(0.9)	53.5
PVT	TP(36)	POPOP	52.5
p-Xylene (dissolved O_2)	PBD(10)	-	59
p-Xylene (de-oxygenated)	PBD(10)	-	73.5
Toluene (dissolved O_2)	TP(5)	POPOP(0.5)	50
Toluene(de-oxygenated)	TP(5)	POPOP(0.5)	62.5

Table 6: Relative Scintillation Efficiency of Polystrene solutions [8]

Solute	Concentration (% by wt.)	Photomultiplier					
		FEU-19				FEU-1C	
		Specimen thickness (mm)					
		10	20	30	75	20	30
p-terphenyl + 3PP	2 + 0.04	50	50	50	50	50	30
TP + TPB	3 + 0.03	50	48	47	-	49	34
TP + QP	3 + 0.1	56	49	45	33	38	34
PPO	1.3	54	46	43	24	37	34

TP = p-terphenyl, TPB = 1,1',4,4'-tetraphenylbutadiene, QP = p-quaterphenyl, PPO = 2,5-diphenyloxazole

2.10 Response

A particular combination of photomultiplier and scintillator will have an energy resolution dependant on the photocathode response function and the scintillation emission spectrum. The absolute spectral sensitivity of the photocathode $\phi(\lambda)$ integrated over the wavelength spectrum $F(\lambda)$ produces the photocathode response function, equation (11).

$$\eta = \int \phi(\lambda)F(\lambda)/ \int F(\lambda)d\lambda \tag{11}$$

The number of electrons from the photocathode per keV of incident energy is the efficiency ε of a particular scintillator, PMT combination. The efficiency combines the emission spectrum from the scintillator and the response from the photomultiplier. The collection of multiple scintillation photons result in a voltage pulse proportional to the number of photons collected. Radiation that strikes the scintillator with equal energy will not produce the same number of photons each time. A measure of the voltage distribution produced by a constant energy source is the pulse-height resolution. The pulse-height resolution is often cited for scintillation materials to characterize and compare response. St. Onge *et al.* [30] observed the pulse-height resolution from two Compton edges of the 1.17 and 1.33 MeV gamma-rays from ^{60}Co and recorded a $\sim 7\%$ full width half max with a 44.4 mm diameter $\times$ 19.1 mm deep liquid scintillator NE213. Many measurements of plastic scintillator resolution choose to use half width half max (HWHM) of the Compton feature to define the 1/2 Resolution ($R_{1/2}$) as,

$$R_{1/2} = \frac{HWHM}{\bar{W}} \tag{12}$$

were $\bar{W}$ is the location on the abscissa where the Compton feature is at its maximum. A cartoon of the technique is depicted in Figure 2.
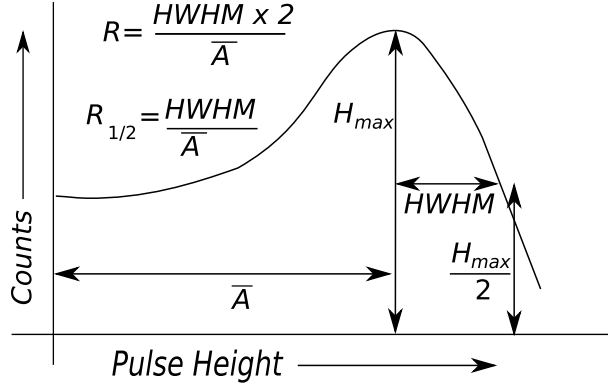
Figure 2:   A depiction of how to determine the the Half Width Half Max from the peak of the Compton edge.

2.11   Modeling

The use of computer modeling has addressed many issues in the development of effective PVT detectors. Neal *et al.* [29] used Detect 2000, and to MCNP-PoliMi to model the percentage of photons recorded versus those emitted, i.e. absolute efficiency of detectors. They varied the reflection coefficient to determine the number of photons recorded versus the reflection coefficient. They then modeled the elapsed time from excitation to the end of the photon history. Further, Neal's group modeled the mean flight time as a function of reflection coefficient, then the mean number of encountered surfaces as a function of reflection coefficient. Mukhopadhayay [28] used MCNP to calculate γ-ray attenuation coefficients for BC-400, which included the photoelectric effects, compton scattering, and pair production. In the same paper he calculates the γ-ray pulse height spectrum from BC-400. Further, the response to several neutron energies from ^{10}B conversion interactions were calculated with the resulting recoil photons. Jordan *et al.* [20] used Geant4 and Detect 98 to calculate the effects of surrounding the scintillator with various materials, adding multiple photomultiplier tubes, positioning of photomultiplier tubes, and the effects of adding light guides. Both codes used by Jordan *et al.* indicated that the most effective coating was loose foil wrapping as opposed to tight foil wrapping, diffuse coating, or air exposure. The modeling efforts also indicate that more PMTs give

better light collection efficiency but that the collection efficiency is not dependant on positioning of the additional PMTs, i.e. PMT's placed opposite each other vs side-by-side. Also Jordan's group found that increasing the size of the PMT's increases the amount of light collected. Jordan also found that the models of the light guides using Geant4 produced a reduction in light collection efficiency of up to 30%. Further, investigations by Jordan's team found that cutting a 45° chamfer on the corner of the scintillator and mating a square PMT to the chamfer reduces the light collection efficiency by 30% to 40%. Williams *et al.* [38] used MCPT to determine the ratio, α, of light output from the detector, L_{det}, to the dose absorbed by the detector, D_{det}, at a particular wavelength, once the sensitivity, ε, was known for a particular wavelength. In equation form, the relationship is $\alpha_\lambda = [L_{det}/D_{det}]_\lambda$. Measured response is related to the MCPT calculated energy absorbtion $[D_{det}/K_{air}]^{MC}_\lambda$ via Equation 13.

$$\varepsilon^{meas}_\lambda = [L_{det}/K_{air}]^{meas}_\lambda = \alpha_\lambda[D_{det}/K_{air}]^{MC}_\lambda \tag{13}$$

A summary table of modeled parameters and the researchers that have modeled them is presented in Table 7.

2.12 *Experimental Spectroscopic Gamma Detection*

Experimental characterization of polyvinyl toluene scintillators has been carried out by many researchers [28] [27] [18] [28] [8] [29]. Only a fraction of the available work described is referenced to illustrate the type and trend of information available.

A review of the literature provides a glimpse of pulse height spectra obtained from many researchers. Mukhopadhayay *et al.* [28] present spectra from ^{60}Co sources on BC-400 scintillators. Miyajama *et al.* [27] presents a pulse height from ^{207}Bi on NE-102A. Hall [18] includes a pulse hight spectrum from the neutron, gamma reactions induced by placing a 10 Ci PuBe source on one side of a barrel of coal and

Table 7:   Modeled efforts from various researchers

Independant Variable	Dependant Variable	Software
Photons Emmited†	Recorded	DETECT2000
Reflection Coefficient†	Photons Recorded	DETECT2000
Distribution of Elapsed Time†	–	DETECT2000
Reflection Coefficient†	Mean Flight Time	MCNP-PoliMi
Distribution of Number of Contacted Surfaces†	–	DETECT2000
Reflection Coefficient‡	Photons Recorded	–
Detector Response*	Ratio Light Output to Absorbed Dose	MCPT MCPT
Scintillator Coating**	Light Collection Efficiency	Geant4 & Detect 98
Position of PMTs**	Light Collection Efficiency	Geant4 & Detect 98
Number of PMTs**	Light Collection Efficiency	Geant4 & Detect 98
Light Guide**	Light Collection Efficiency	Geant4 & Detect 98
Chamfered Corners and Mated Square PMT**	Light Collection Efficiency	Geant4 & Detect 98 Geant4 & Detect 98
γ-ray attenuation coefficient§	–	MCNP

†Neal *et al.* [29], ‡Miyajama *et al.* [27], * Williams *et al.* [38], ** Jordan *et al.* [20], §Mukhopadhayay *et al.* [28]

a 5×5 inch cylindrical Pilot Y scintillator from New England Nuclear Corporation on the other side. The majority of γ-ray interactions with plastic scintillators are via Compton scattering resulting in a pulse-height spectrum with poor resolution and Compton edges as the only discernible feature. The pertinent equation for the location of the compton edge is

$$T_{CE} = \frac{E_\gamma^2}{255.5 + E_\gamma} \quad [\text{KeV}], \tag{14}$$

where T_{CE} is the maximum recoil Compton electron energy, and E_γ is the energy of the incident γ-ray.

Though the full energy peak is typically used to correlate energy deposited in a detector, several researchers have made use of the the Compton edge for energy calibration. Both Mukhopadhayay and Miyajama present graphs of an energy calibration using multiple mono-energetic gamma sources. Hall [18] discusses the

calibration but does not present it in his report. Of the three researchers that mention energy calibrations using the Compton edge, Mukhopadhayay is the only one to mention non-linearities, though they are to be expected as described in section 2.8.4 [21]. Miyajama indicates that the sources used where ^{54}Mn, ^{207}Bi, ^{60}Co, ^{22}Na, and ^{208}Tl. Hall, when making an energy calibration with PuBe, ^{228}Th, and ^{60}Co, did not mention non-linearities.

Hall's, Miyajima's, and Neal's group attempted to characterize the efficiencies in plastic scintillators [18] [27] [29]. Neal *et al.* produced a plot of absolute efficiency on a $1 \times 1 \times 0.08$ m slab of PVT. Hall's group investigated the relationship between the height of the Compton edge and the trough of the Compton continuum, as well as the 1/2 Resolution in PVT scintillators; see Figure 2 for a depiction of how to determine the 1/2 Resolution. Hall also investigated the effects of different sized scintillators, and number of PMTs; some of his results are given in Table 8. In general, smaller size scintillators have better 1/2 Resolutions, and larger peak-to-valley ratios, while adding more PMT's improves resolution and leaves the peak-to-trough ratio constant. Hall concluded that plastic scintillators where not suitable for a complex gamma spectrum. A comparison between the number of scintillation photons created by NaI and PVT was made by Miyajima *et al.* using commercially available NaI(Tl) and NE-102A scintillators.

Table 8:   1/2 Resolution from various sources using one and two PMTs Hall *et al.* [18]

PMTs	1PMT		2PMT	
Size	5x5	5x10	5x5	5x10
PuBe	11.1	20.5	7.7	12.2
^{228}Th	10.9	20.8	8.4	8.2
^{60}Co	19.6	25.1	17.5	29.2

Hall *et al.* analyzed the (n,γ) produced emission from sulfur in coal, and exposed coal to a 10 Ci PuBe sources. Peaks where observed at 2.23 MeV from hydrogen, 4.43 MeV from carbon, and 7.6 MeV from iron, but he was unable to

find the 5.4 MeV peak from sulfur. The efficiency of the Pilot Y scintillators were determined to be ≈0.93%. Unlike typical pulse-height spectra the discernible features arose from Compton scattering and not from full energy peaks.

Zao *et al.* [23] studied the effects of radiation on the commercially available PVT based scintillators, BC-408, BC-404, and EJ-200. They present the emission spectra and light yield spectra before and after irradiation by two ^{60}Co sources, one with an activity of 1 Ci and the other with an activity of 5 MCi. Zao *et al.* did not find a significant change in the emission spectrum after exposing the samples to 1.44×10^4 Gy. The light output did however degrade significantly. The number of observed photoelectons per unit energy deposition (in MeV) is taken to be the light yield as defined by Equation 15, where E_γ is the energy of the γ-ray from ^{241}Am, P_{SPE} is the position of single photoelectron from a Gaussian fit of the thermal noise spectrum, and P_p is the full energy peak location.

$$LY = \frac{P_p}{P_{SPE} \times E_\gamma} \qquad (15)$$

They also found that rapid light yield decreases were found after exposures to > 50 Gy. After exposure to 600 Gy, the light yield for BC-408 was found to decrease by 14.1% from its pre-radiation value, while the decrease was 13.4%, and 10.6% for BC-404, and EJ-200 respectively. They also found that there was not a significant recovery of light yield after 100 hours for doses of 0.57 Gy.

Research continues in the formulation of PVT-based scintillators in order to exploit particular traits. Some of the recent results are presented here. Albrecht *et al.* [6] mixed and tested several mixtures of compounds and found that there were at least two compounds that have similar emission spectra to that of the reference scintillator EJ200. The compounds, described as DSB1 and DSB2, where found to have faster response than a typical dye Y11. The PVT solvent was identified to have fluorescent decay times of 1.67 ns, the Y11 solute to have decay times of

8.3 ns, while the DSB1 and DSB2 solutes where found to have decay times of 1.8 and 2.2 ns. Campbell and Crone [9] found that the light yield of PVT could be increased by adding a phosporescent dopant to the PVT mixture. Iridium in the form of $irdium(III)tris[2-(4-totyl)pyridinato-NC^2]$, or $[Ir(mppy)_3]$, was added to the solution in concentrations of up to 35 weight percent. The fluorescence yield was found to be about $\approx 200\%$ that of anthacene (32000 photons/MeV) with a 20 weight percent addition of $Ir(mppy)_3$. Williams *et al.* [38] analyzed the response of pure PVT, BC-400 and a custom-made scintillator. The Williams group added 4 weight percent 4-chlorostyrene, butyl-PBD at 20 g/l and BBOT at 1 g/l to PVT in order to find low energy experimental support for Birk's sensitivity reduction due to ionization quenching, and the unimolecular quenching model. They found that sensitivity was increased with addition of Cl in the form of 4-chlorostyrene,butyl-PBD to the mixture, making the mixture with the approximate sensitivity of water. Further, they found that sensitivity was depressed by ionization quenching, but the unimolecular quenching model, Equation 9, did not fit their measurements.

2.13   Detector Production

The steps necessary to produce a scintillator panel from styrene monomers is quite similar to that used to produce polyvinyl toluene, which makes the discussion from Birks [8] on the polymerization of styrene useful for gaining a cursory understanding of the steps that go into producing a scintillator panel.

Monomers of the styrene molecule can be polymerized when heated to form a thermoplastic polymer of polystyrene. The ethylene, or vinyl groups, are the major players in the polymerization process. Several ways of producing the plastic scintillator are to:

- add p-terphenyl(TP) to molten pholystyrene;

- use a benzoyl peroxide catalyst (0.1-1%) to polymerize styrene at low temp $\approx 50^o C$.

- use a catalyst to polymerize styrene at temperatures in the range of $125-140^oC$

- polymerize it at higher temperatures $\approx 200^oC$ without a catalyst over the course of 12-15 hours.

The best scintillators were obtained from the benzoyl peroxide method, although its presence reduces light transport. A variant of the molten polystyrene method has been used in pressure and injection style casting processes. The technique with the widest use is polymerization at higher temperature.

Application of the high-temperature technique is somewhat size dependant. For small samples, the polystyrene is vacuum distilled multiple times before mixing with the solute. It is then vigorously shaken and de-gassed by multiple freeze and thaw cycles. The contents are then sealed and placed in a furnace at 125^oC for 7 days. For larger scintillators, for example, to produce a 45-inch diameter by 3 inch scintillator, the following procedure has was used [8].

1. Nitrogen is bubbled throughout the monomer to remove any dissolved oxygen.

2. The mixture is thoroughly mixed to insure a homogeneous solution.

3. Polymerization is initiated by heating.

4. The polymerization temperature is controlled to prevent damage to the organic molecules.

5. The complete polymerization is insured by maintaining the temperature.

6. The sample is quickly cooled to make removing from the vessel easier.

7. The plastic is annealed to heal damage caused by instant sharp cooling.

8. The scintillator is machined to the desired dimensions.

The vessel is coated with PTFE to ease removal. Sticking is reduced by zinc stearate in the solution at concentrations of approximately 0.036 %, although this can cause a 5% decrease in scintillation efficiency. The reaction is conducted in a

nitrogen atmosphere and reflux is returned to the solution by way of several reflux condensers fitted to the reaction vessel. Nitrogen is bubbled through the monomer to get ride of the oxygen. The exothermic reaction ensues once the solution reaches 140^oC. After the heat from polymerization has subsided, the reaction product is boiled three times and heating is continued for 22 hrs. The scintillators are then annealed at 120^oC for 5 hours, then cooled 50^oC over a 12 hr period. Finally, when the reaction ends, the volume will have been reduced by 15%.

The production of intermediate sized scintillators can be achieved by performing multiple vacuum distillations. As with the larger scintillators, nitrogen is bubbled through the monomer for 30 min with the reflux being returned to the solution. The vessel is sealed and the gasses vacuumed out. The vessel is then brought to 200^oC. A formula for polymerization time is t = 0.02 U, with U being the styrene volume in ml. The polymerized reaction product is cooled to 100^oC over the course of several hours.

2.14   Portal Detectors

Several studies have been performed to analyze the function of portal detectors and the relative merits of using PVT verses other scintillators. The detection of radiation depends on many factors. Three key factors are the amount of radiation, the type of radiation, and the detector. These aspects work together to determine the effectiveness of a detection system. The first factor to consider is the amount of radiation. Many detectors in operation record only the presence of radiation as discussed in the Section 2.2. Though radiation may be present, it takes a quantity that is greater than the background to be identified. In isolation almost any radioactive material is detectable by even the simplest of detectors, but when background is included in a measurement detection becomes more difficult.

As an example, vehicle portal detectors using PVT scintillation registers counts from background radiation when no vehicle is present. When an automobile enters

the detection region of the detector the counts from background decrease. The extent of suppression and the techniques to handle the resulting decreased background is the topic of the paper by Lo Presti *et al.* [24]. Though I would refer the reader to the paper for details a short background is appropriate. Detectors of the size common in portal detectors, $2 \times 14 \times 48$ or larger, will record a large number of counts from naturally-occurring radiation background. When a vehicle enters a portal detector its presence acts as a partial shield for background radiation. The shielding effect reduces the counts per second the portal detector registers. The size and makeup of the automobile determine the amount of count rate depression. The effect this has on the detectors ability to identify a radiation *source of interest* is dramatic. The radiation source needs to produce enough radiation to make up for the background count rate depression. Further, the background count rate must be exceeded to produce an alarm. Unless the automobile caries a particularly active source, the amount of counts registered will not be as great as the background registered when the automobile is not shielding the detectors.

Some of the detection issues listed above can be ameliorated if a system is employed that can distinguish the energy and, to some extent, the type of radiation. The science of spectroscopy has given copious tools for determining the composition of a radiation source. If energy information were available, it could be compared to spectroscopic databases, lending support for identification of a source of interest. The combined count rate information as well as energy information could be used to reduce errors in detection, allow the detectors to identify the presence of a radiation source more confidently, and improve confidence.

There is a large selection of materials that can be used to make detectors that can resolve energy. Among those of note are sodium iodide doped with thallium (NaI(Tl)), and high purity germanium. Since gamma radiation interacts partially by photoelectric effect with these detectors, they produce pulse-height spectrum with peaks corresponding to different energies. In contrast, pulse-height spectrum from

PVT are broad distributions because γ-rays interact primarily by Compton effect with low atomic weight elements such carbon and hydrogen. Even the most active sources result in little more than inflections in the normally recorded background spectrum [13]. Given a material capable of resolving the energy of radiation, an algorithm could be employed to compare the number of counts under the peak of interest to the number of counts in other regions of the energy spectrum. Ely *et al.* suggest the application of a similar algorithm to the pulse height spectrum from PVT [13] and concludes that three sections of the spectrum can be taken in ratio to discriminate between commercial goods that include radiation, background and man-made nuclear materials.

The efficiency of a material is a measure of its ability to detect the radiation that strikes it. Some materials are able to detect a large fraction of the radiation that strikes it. The efficiency of a scintillation material is energy dependant but as a reference the NaI(Tl) has an intrinsic efficiency as high as 90%, where intrinsic efficiencies for PVT have been calculated by Siciliano *et al.* [32] to be in the 30-40%. The absolute efficiency of a detection system, includes multiple factors two of the factors of note are the intrinsic efficiency of the detector, and the other is the solid angle subtended by the detector. Though the intrinsic efficiency of NaI(Tl) is three fold greater than that of PVT, the absolute efficiency of the system can be made equivalent by the large size of PVT scintillators and hence the absolute solid angle subtended by the detector. Suciliano *et al.* have modeled and tested the detection characteristics of portal monitors made of NaI(Tl) and PVT. His team concluded that portal detectors made of PVT where effective as a first screening device, but that NaI(Tl) was more effective under a secondary screening.

III. Methodology

3.1 Problem Definition

3.1.1 Goals.   The first goal of this research is to determine the light collection efficiency and resolution of polyvinyl toluene(PVT) based scintillators with a composition equivalent to that of the BC-408 plastic scintillator available from Saint-Gobain. Secondly, to determine if there is significant variation in these measurements within a plastic scintillator, between multiple scintillators from the same manufacturer, or variation between manufacturers. The third goal of this research is to demonstrate the use of polyvinyltoluene as an efficient means to determine the energy of incident gamma radiation.

3.1.2 Hypothesis.   There will be significant variation in the resolution and efficiency from panel to panel and from manufacturer to manufacturer and that these differences will be quantifiable using straight forward statistics.

3.1.3 Approach.   To pursue these research goals scintillators from different manufacturers were exposed to collimated mono-energetic gamma radiation to determine if there is a difference in the efficiency and resolution as determined by the number of counts recorded by the spectroscopic system, and the 1/2 Resolution of the Compton edge.

3.2 Experimental Setup

The polyvinyl toluene Scintillator Test System (PSTS) was constructed to test PVT-based scintillators. The boundaries of the system, Figures 3, and 4, include the scintillator, housing box, the timing circuit, the light collection system, and the data acquisition computer. First, the $12 \times 15 \times 2$ in scintillator was wrapped in an appropriate reflective coating in an attempt to optimize light collection. Next, the housing box was constructed with a Uni-Strut jig to hold the scintillator and provide

31

for convenient replacement of the scintillator. The box was designed to be light-tight, blocking ambient light from interacting with the scintillator. The light collection system was a Hamamatsu model R329-02 photomultiplier tube (PMT) with a 50 mm diameter face connected to a counting and spectrographic system. The voltage pulse signal, created by a photon interaction with the PMT, traveled through the pre-amp to the spectroscopic amplifier then into the multi-channel analyzer. Finally, a computer recorded the voltage events that made it through the light collection system and timing circuit.
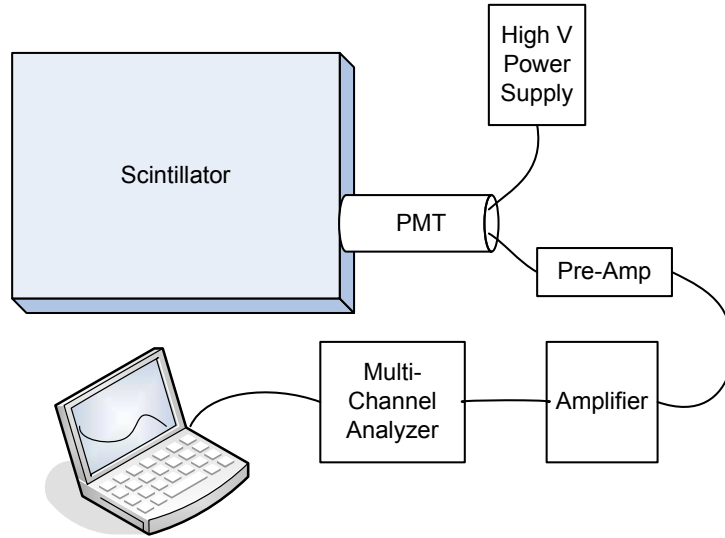
Figure 3:   Experimental Circuit Setup

3.3 System Response

The PMT does not respond to a single incident photon, but instead produces multiple electrons from multiple incident photons, and the voltage pulse is a combined response to all incident photons. The number of photons incident on the PMT face ultimately determines the size of the pulse. The more photons that interact, the larger the pulse. The number of photons produced from a scintillation event
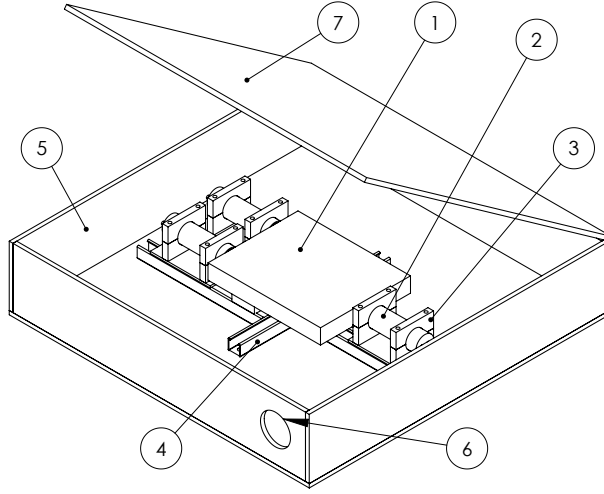
Figure 4: Experimental setup 1) scintillator; 2) photo multiplying tube; 3) mounting brackets; 4) Uni-Strut jig; 5) light box; 6) holes for air flow and temperature flow; 7) lid.

is typically correlated to the energy of the incident particle. Thus, a pulse-height spectrum can frequently have its abscissa replaced with energy instead of channel.

3.4 Workload

The polyvinyl toluene (PVT) scintillator was exposed to a collimated beam of $\approx 662 keV$ gamma radiation from ^{137}Cs of approximately 5.01 μCi. The collimator shown in Figure 5 provides a solid angle of 0.5528 steradian as calculated by the Bessel function approximation Knoll [21]. The incident gamma flux was calculated to be 6931 $photons/cm^2 s$ across the $2.83 cm^2$ bottom of the collimator (Figure 5). The fluorescence decay time of scintillations with BC-408 and others of comparable compositions is 2.1 ns. The response of the photomultiplier tubes has a rise time of 0.7 ns and a transit time spread of 16 ns.
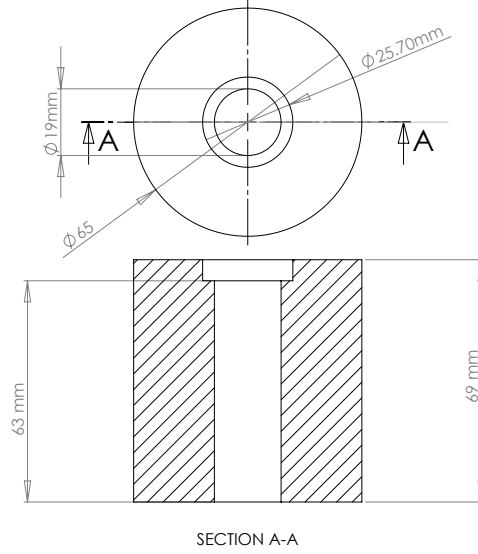
Figure 5: Collimator made of poured Cerrobend® with depression to hold a standard sized 25mm button source.

3.5 Performance Metrics

The quantity of photons emitted from the source was related to the activity of the source. A collimator, cast from Cerrobend®, was used to localize the area of γ-interactions and reduced backscatter. There where two main measurements of performance used in this study. First, the efficiency, and secondly the 1/2 Resolution of the Compton edge.

3.6 Parameters

3.6.1 System Parameters. The PSTS was constructed of several parts, each with its own impact on the performance of the system. The following are system parameters that were kept constant while conducting the experiment. The influential system parameters where:

1. Power Supply Voltage
2. Pre-Amplifier Resistance
3. Amplifier
   - Coarse Gain

34

- Fine Gain
- Pulse Shaping Time

4. Number Of Analog To Digital Converter Channels
5. Source Activity
   - Energy Of Decay
   - Percent Of Decay By This Mode
   - Activity Of This Decay

In preparation for the main course of experimentation, a reference piece of BC-408 was optically mated to the individual photomultiplier tubes to ascertain the appropriate settings for system parameters.

3.6.2 Workload Parameters.   The workload parameters were the items changed in order to observe a change in the system performance. The workload parameters included:

1. Position Of The Source
2. Scintillator Panel

3.7 Evaluation Technique

The evaluation technique was direct measurement of scintillation events using photomultiplier in a energy circuit.

3.8 Experimental Design

The experimental design was a full factorial approach. Sample measurements were taken at a handfull of positions across the scintillator surface. After becoming familiar with the data trends, the collimator was placed at 42 positions and a pulse height spectrum recorded for each location. The scintillators were two $12 \times 15 \times 2$ in polyvinyl toluene based BC-408 from Saint-Gobain [17], and two EJ-200 scintillators from Eljen [34]. Each panel was placed inside the Uni-Strut mounting rail, and mated to the photomultiplier tubes. The 5.01 μCi NIST-traceable source of

^{137}Cs was placed inside the collimator and the collimator placed on the surface of the PVT scintillator panel (Figure 6). The panel was marked with a 2×2 grid and measurements where performed by placing the collimator and source at a grid position, closing the lid, and recording the pulse height spectrum from 42 positions per scintillator. Each pulse-height spectrum was exploited to yield two pieces of data, the pulse-height spectrum, and, if the counts where summed, total counts.
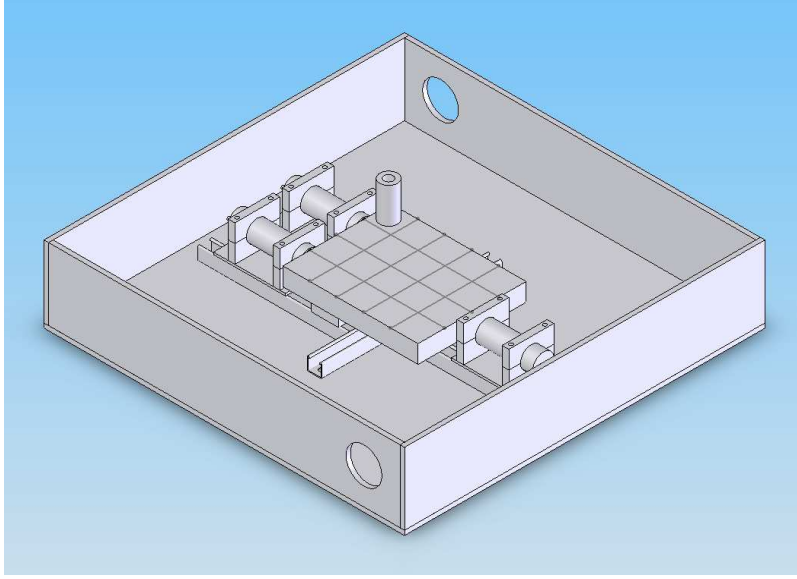
Figure 6:   Light box with scintillator mounted on the Unistrud mounting rail and a grid scribed on the scintillator.

3.9   Initial Tests

The gain settings from the sample BC-408 piece were used as a starting point for the gain settings in the PSTS. A polished piece of 1.5 inch diameter by 0.75 thick BC-408, coated on one side with TiO_2, was used. The side not coated with TiO_2 was polished and mated to the Hamamatsu PMT with optical grease. A ^{137}Cs source was taped to the side with the TiO_2 coating. The whole assembly was triple wrapped with 0.4 mm aluminium foil with the seams taped with electrical tape. An example of the pulse-height spectrum obtained is shown in Figure 7. The gain was adjusted to place the Compton edge feature at about 5V for each PMT.
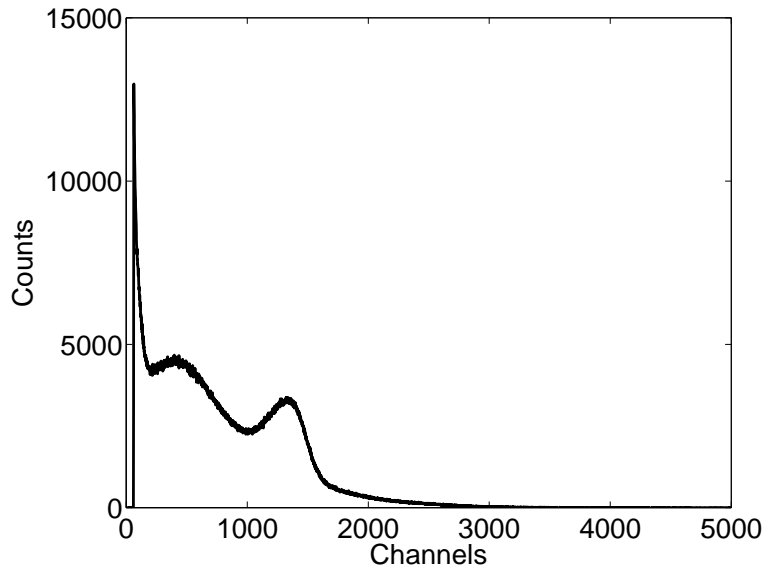
Figure 7: Pulse-height spectrum from a polished piece of 1.5 inch diameter by 0.75 thick BC-408, coated on one side with TiO_2 sandwiched between a button source and the PMT.

Several experiments were conducted to determine the effectiveness of the light box. Several pulse-height spectrum were collected, both with the room lights on and with the room lights off. The spectrum was recorded with the power supply voltage set to 1500V, the Pulse Shaping time set to 1.5 μs, the course gain set to 50, the fine gain set to 10.4, collimator and source placed axially to the PMT 5 in from the face. The results of the lights-on measurements, shown in Table 9, indicated that for the system settings indicated there was as much as a 50% increase in the count rate. Therefore all subsequent measurements were taken with the room lights off.

Table 9: Determination of the effects of ambient light on pulse-height spectrum

Lighting Condition	Average Counts	Counting Time	Std Dev
Room Lights On	1.728×10^6	60 s	8.5×10^4
Room Lights Off	1.115×10^6	60 s	2.1×10^4

A second series of tests where performed, with the same experimental settings, to determine the effects of opening the door to the room for 5 seconds while recording

37

the pulse-height spectra. The standard deviation of the door opening experiments was 2.5×10^4.

A series of power supply voltage setting experiments where conducted. Spectra were taken for one minute, leaving all the experimental settings constant except for the power supply voltage. The power supply was stepped up in increments of -50 V from -700 to -2000 V, while leaving all other factors constant. The pulse-height spectrum was recorded for each -50 V increment, paying particular attention to the dead-time and voltage signal from the pre-Amp on an oscilloscope. At -1600 V, dead-time started to appear. Then at -1800 V the dead time exceeded 40%. Ultimately, a power supply voltage of -1500 V was used for all subsequent measurements.

Experiments where conducted to determine the effects of the pulse-shaping time. Each setting was tested to determine the minumum dead time. It was found that the minimum dead time occured when the pulse shaping time was set to $0.25\mu s$. All subsequent measurements where made with the $0.25\mu s$ setting.

3.10   Methodology Summary

The efficiency and resolution variation among polyvinyltoluene scintillators was examined by placing scintillator panels inside the PSTS and placing a collimated mono-energetic γ-source at various positions.

3.11 Modeling Approach

A simulation was constructed to simulate the exposure of a polyvinyl toluene scintillator to ionizing gamma radiation using photons, and electrons.

3.12 Modeling Experimental Setup

The simulation consisted of a square *experimental hall* three meters on a side filled with air. All the interactions that originate from the particle gun were tracked from creation to absorption or escape from the hall.

| (a) | (b) |
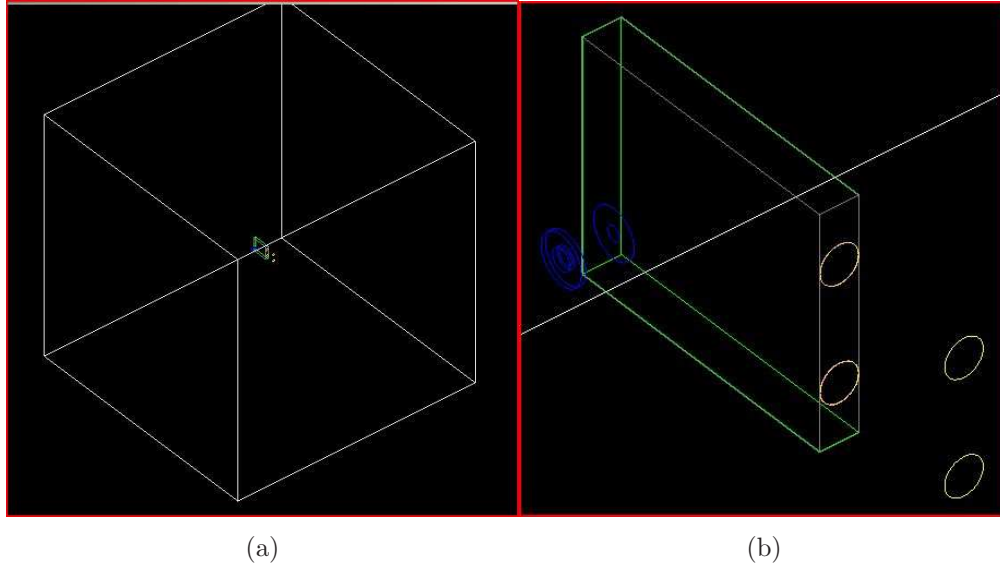
Figure 8:   A visualization showing experimental hall with the PVT scintillator in the middle: (a) experimental hall; (b) zoom of PVT detector.

3.13 System Response

The simulated system recorded a hit when a photon "hit" one of the PMTs. The energy of each photon striking the PMT was also recorded.

3.14 Workload

The simulations created and tracked thirty thousand $\approx 662keV$ photons from the point of origin, the center of the collimator and ≈ 6.3 cm from the scintillator surface. The was angle varied by multiplying the maximum angle by a 0 to 1 random number yielding a random distribution of photon directions across the 0.558 steradian solid angle.

3.15 Performance Metrics

The recorded information for the simulation were the number of "hits" per channel and the energy of the incident photons.

3.16 Parameters

3.16.1 System Parameters. The portion of the simulated system that did not change over the course of the experiment where the five objects and materials inside the *experimental hall* and the particle, in this case photons.

1. Collimator
   - Shape & Size
   - Material
   - Optical Properties
     - Absorption Length
     - Refractive Index
2. polyvinyl toluene scintillator
   - Shape & Size
   - Composition
   - Density
3. Aluminum wrapping
   - Absorption Length
   - Refractive Index
   - Density
   - Optical Properties

- – Absorption Length
- – Refractive Index

4. Optical Grease
    - Composition
    - Density
    - Optical Properties
        - – Absorption Length
        - – Refractive Index

5. Photomultiplier Tube
    - Material
    - Shape & Size
    - Optical Properties
        - – Absorption Length
        - – Refractive Index

6. Particle
    - Type
    - Energy

Each of these properties can be individually set and manipulated to match the experimental environment. Further, physical processes were modeled to simulate the response of the experimental system. The processes included:

1. Gamma Conversion,
2. Compton Scattering,
3. photo-electric effect,
4. ionization,
5. Bremsstrahlung,
6. multiple scattering,
7. optical Rayleigh scattering, and
8. boundary Processes.

These parameters were kept constant throughout the simulations.

3.16.2 Workload Parameters. The items that were manipulated to produce a change in the number of "hits" recorded or their energy, was:

1. Optical Properties
   - Absorption Length
   - Refractive Index
2. Scintillation Properties
   - Scintillation Yield
   - Fast Scintillation Spectrum
   - Slow Scintillation Spectrum
   - Resolution Scale
   - Yield Ratio
3. Gun Direction
4. Gun Position
5. Collimator Position

The Optical properties were taken as a best guess from available materials. The refractive index was set to values ranging from 1.34 to 1.36 for photon energies 2.0 through 4.1 eV. The absorption length was taken from the NIST web site [4] which gave the x-ray attenuation coefficients for PVT. The scintillation yield was taken from Knoll [21] as a reference to anthracene. The fast and slow emission spectra where set with the same intensity and spectrum derived from the emission spectrum from BC-408 [17], noting that the fast and slow emission spectrum are identical, just of different probability (Section 2.8.2). The resolution scale was set to one, and the yield ratio set to 0.8, representing the ratio of fast to slow component scintillation.

3.17 Evaluation Technique

The evaluation technique was simulation. The effects of thirty thousand $\approx$ $662keV$ gamma rays incident on a polyvinyl toluene scintillator panel were *simulated* as secondary radiation passed through the scintillator and ultimately struck the photomultiplier tube.

3.18   Experimental Design

The fate of thirty thousand particles were tracked until they were absorbed by the scintillator, left the Experimental Hall, or entered the PMT. The first simulation was done for the source and collimator placed one inch from the PMT face along the centerline of the PMT. For subsequent simulations, the collimator was moved further away, at distances 3, 5, 7 . . . 13. inches from the PMT face.

These experiments were designed to be qualitative in nature, yielding subjective support for trends created by the physical processes measured. As a result the collimator and particle source where not placed at all the 42 positions used in the experimental study.

3.19   Initial Tests

An incremental approach to performing simulations was taken. The initial simulations were smaller, firing 1, 5, and 10 gamma rays at the scintillator. The process was observed using the visualization environment. The visualizations allowed verification of the proper position of both the collimator, and the source of $662keV$ photons. After firing a handfull of photons, the perspective was changed to see the simulation from all sides.

Next, several tests were made by moving the source and collimator to some extreme positions to see how it effected the pulse-height spectrum. Then some of the Workload parameters were changed to observe the effects of changing attenuation length, resolution scale, and light yield. After seeing that the results fit with the presumed physics of the simulation, more extensive batch simulations were preformed.

3.20   Simulation Methodology Summary

The effects of a collimated beam of $\approx 662keV$ gamma rays incident on an aluminum-wrapped polyvinyl toluene scintillating detector were simulated using Geant4. Geometries of the scintillator, its wrapping, the collimator and photo-

multiplier tube were included in simulations which tracked thirty thousand gamma rays. The number of photons that struck each photomultiplier tube were recorded, along with their incident energy.

IV. Results

The positions at which the collimator and source where placed for measurements are depicted graphicly in Figure 9. The photomultiplier tube was placed on the 12 inch side 3 inches from the bottom. The centerline of the collimator was positioned at 2×2 inch grid positions. The first point was positioned 1 in from the side and 1.25 in from the bottom, subsequent positions where 2 in away in either direction.
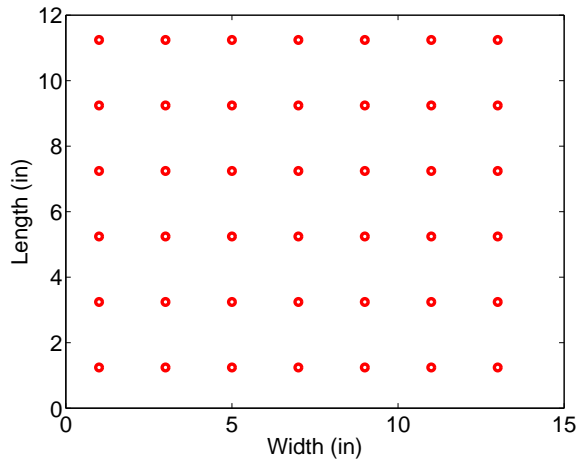
Figure 9: Spacial representation of the positions where pulse height spectrum where collected.

4.1 Experimental Results

The zero to ten volt response from the multi channel analyzer was divided into 8191 channels. An example of the spectrum recorded is shown in Figure 10. The PSTS was left in the same configuration for each panel measured using the experimental settings in Appendix D.

Figure 10 shows that the largest peak had significantly more counts than the other features of the Compton continuum. Background spectra were taken immediately after each spectrum was measured. A combined log plot of a spectrum taken 5 in from the PMT's face and along its axis is shown in Figure 11. Spectral comparisons where made using only the information from the Compton region, which
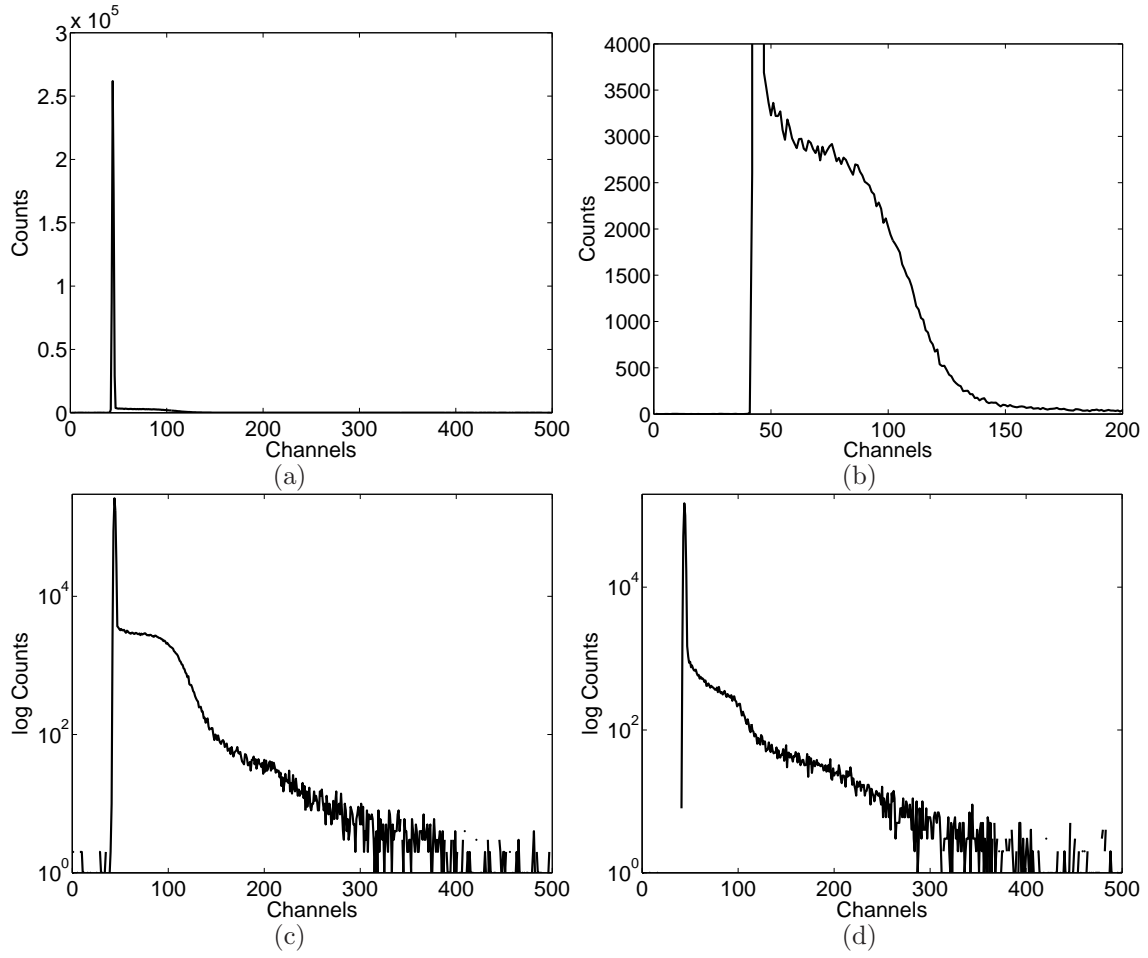
Figure 10: Typical pulse height spectrum (a) Typical pulse height spectrum (b) semi-log plot of the pulse height spectrum, and (c) magnified pulse height spectrum, and (d)the background immediately after measurement.

was defined by the channel where the largest peak ended, channel 47, and where the counts dipped below 40 counts per channel. The pulse-height spectrum from panel to panel differed significantly, although attempts were made to be consistent in the placement of the scintillation panel and attachment of the photomultiplier tubes. The shape of the Compton continuum was however very similar. This led to the need to normalize the total counts in the Compton region of the spectrum before producing the plots in Figure 12.

46
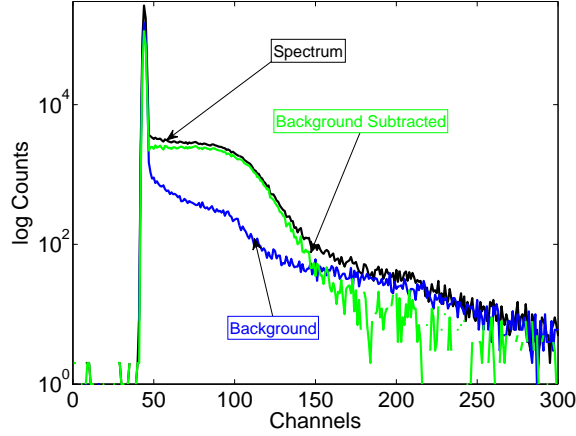
Figure 11: Pulse-height, background, and backgrond subtracted pulse-height spectra plotted on the same axis.

The resulting spectra from the factory wrapped Eljen scintillator is shown in Figure 13, with the balance of the spectra presented in Appendix F. The peak of the Compton edge was located using a non-linear fit to a composite Gaussian curve and a negative exponential. The heights of the Compton edge for the spectra obtained at each position across the panels are presented graphicly in Figure 14. The location of the Compton edge is similarly presented in Figure 15, here the edge is taken to mean the peak of the Compton feature. The half-width half-max obtained from the Compton edge of the spectra recorded at each location across the scintillator panel is presented in Figure 16. The 1/2 Resolution of the Compton edge feature of each scintillator panel is presented in Figure 17. The background was subtracted from the pulse height spectrum to determine the efficiency at a location. The efficiency is presented for the four panels in Figure 18.

4.2 Simulation Results

The simulation of $\approx 662 keV$ gamma rays incident on a $12 \times 15 \times 2$ in panel of polyvinyl toluene was performed using the Geant4 Toolkit. Some of the visualizations are presented in Figures 19a-c. A representation of the pulse-height spectrum obtained from tracking the movement of 30,000 gamma photons from creation to

47
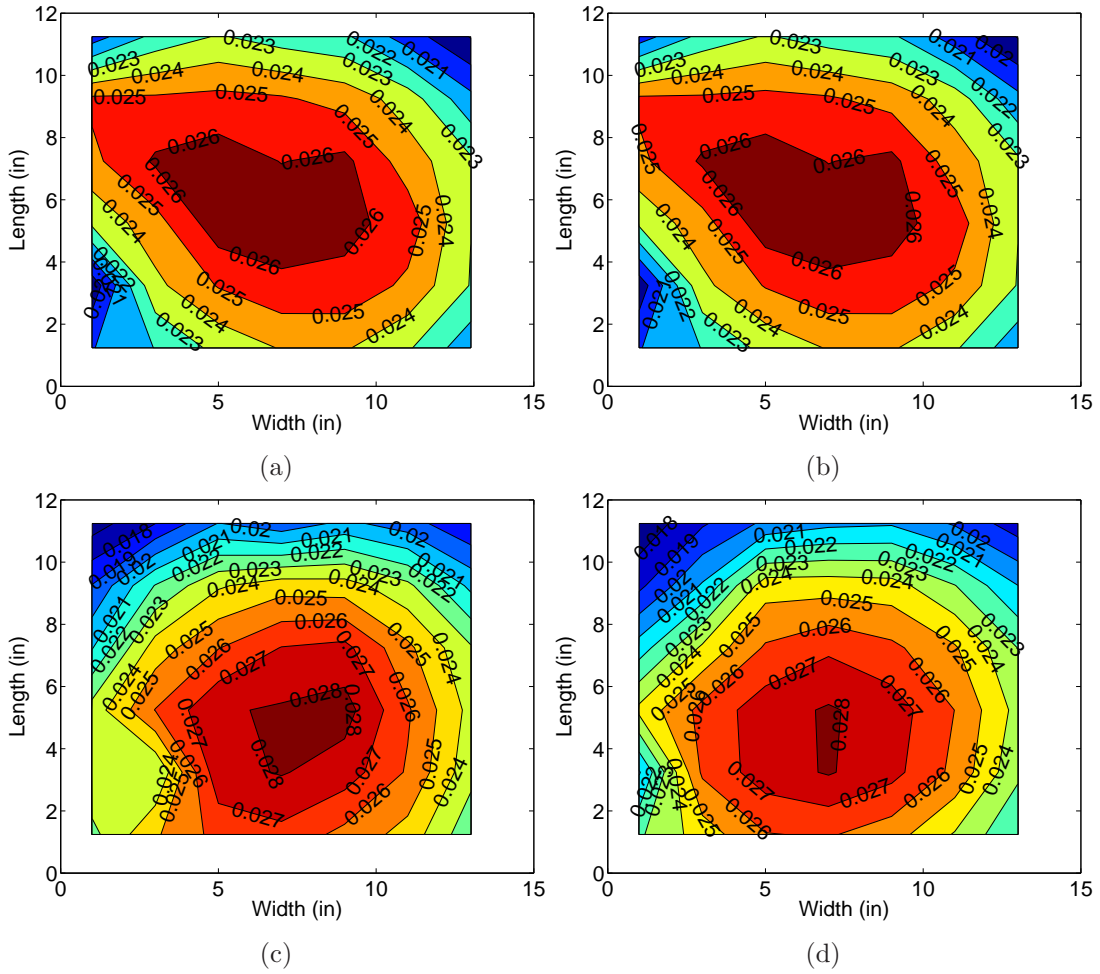
Figure 12: Normalized contour plots of total counts in the Compton region of the spectrum with of the background removed: (a) factory wrapped BC-408; (b) researcher wrapped BC-408; (c) factory wrapped EJ-200; and, (d) researcher wrapped EJ-200.

loss is presented in Figure 20, the plots are for the collimator placed 1, 5 and 13 inches from the PMT. The direction of the photons was randomly distributed over the 0.5528 steradian angle of the opening of the collimator as seen from the position of the source.

48
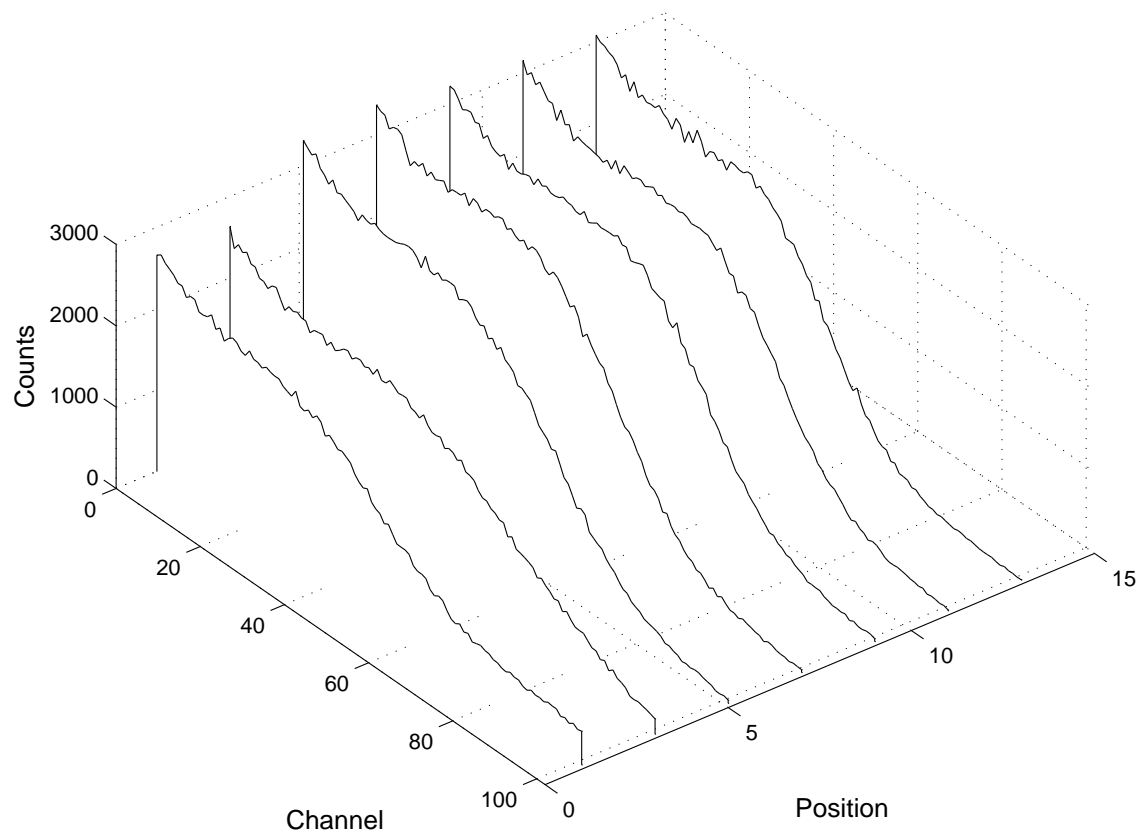
Figure 13: Stacked spectrum from factory wrapped EJ-200 scintillator panel for each position in a row.
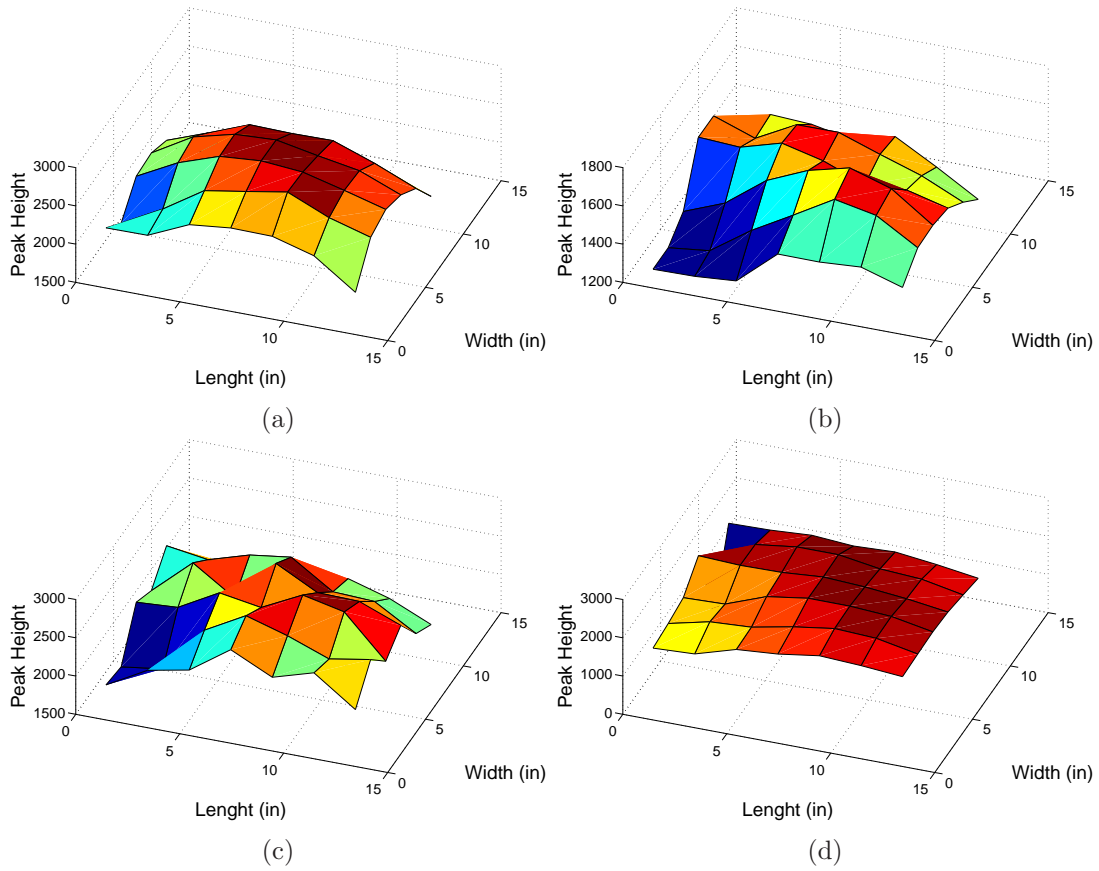
Figure 14: Height of the Compton edge: (a) factory wrapped BC-408; (b) researcher wrapped BC-408; (c) factory wrapped EJ-200; and, (d) researcher wrapped EJ-200.
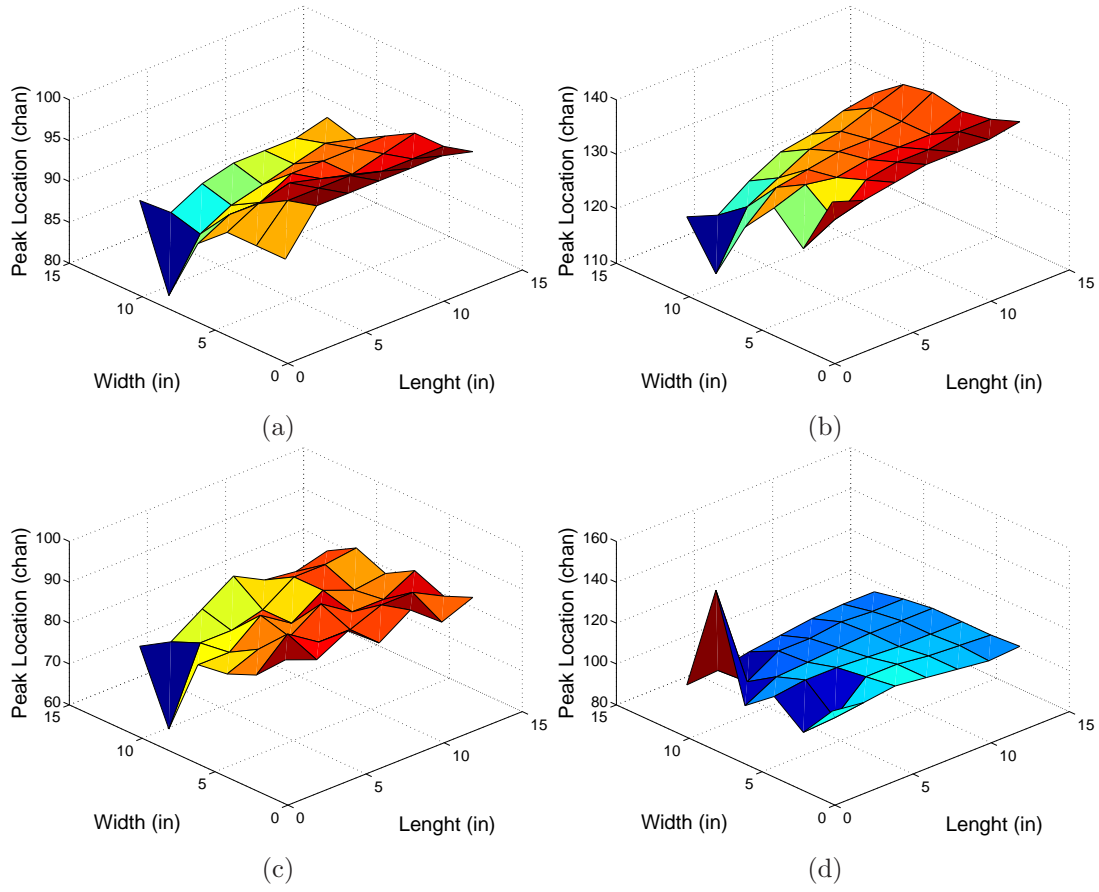
Figure 15: Channel location of the Compton edge in the pulse height spectrum: (a) factory wrapped BC-408; (b) researcher wrapped BC-408; (c) factory wrapped EJ-200; and, (d) researcher wrapped EJ-200.
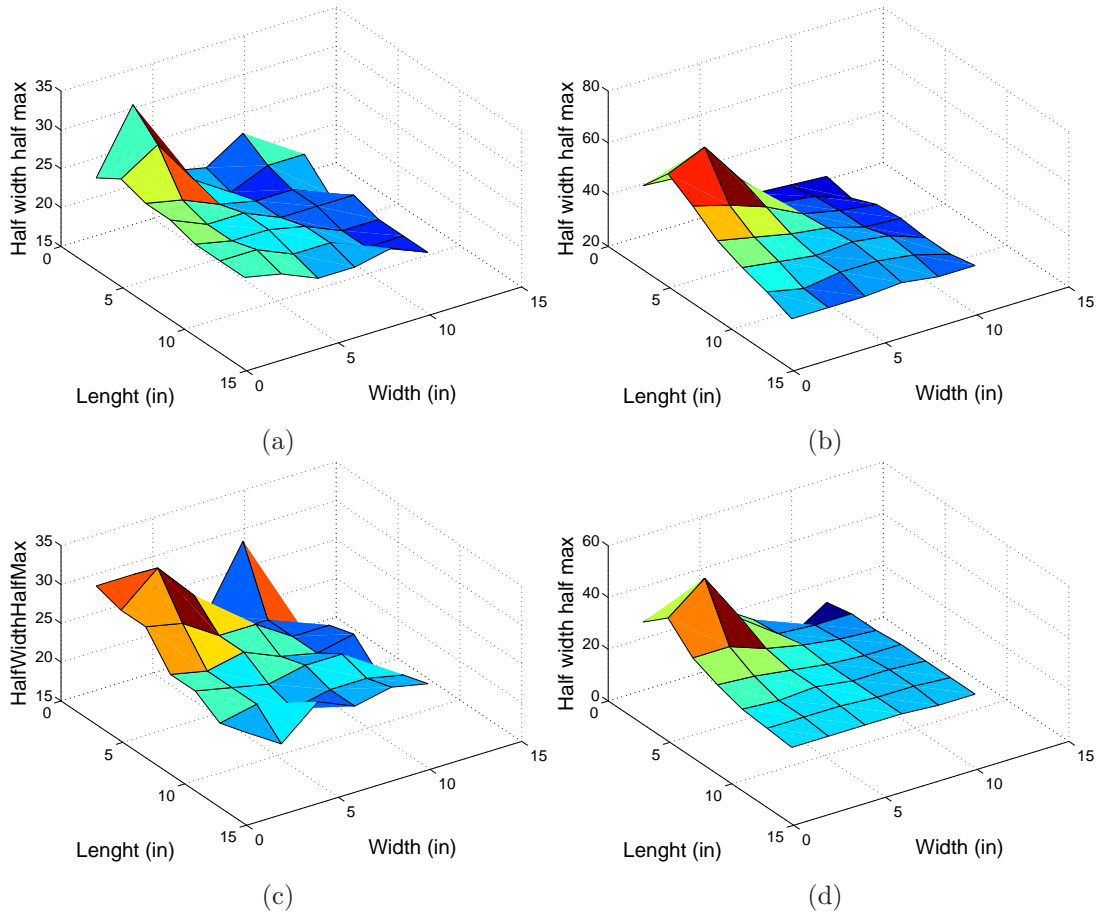
Figure 16: Half width half max of Compton edge: (a) factory wrapped BC-408; (b) researcher wrapped BC-408; (c) factory wrapped EJ-200; and, (d) researcher wrapped EJ-200.
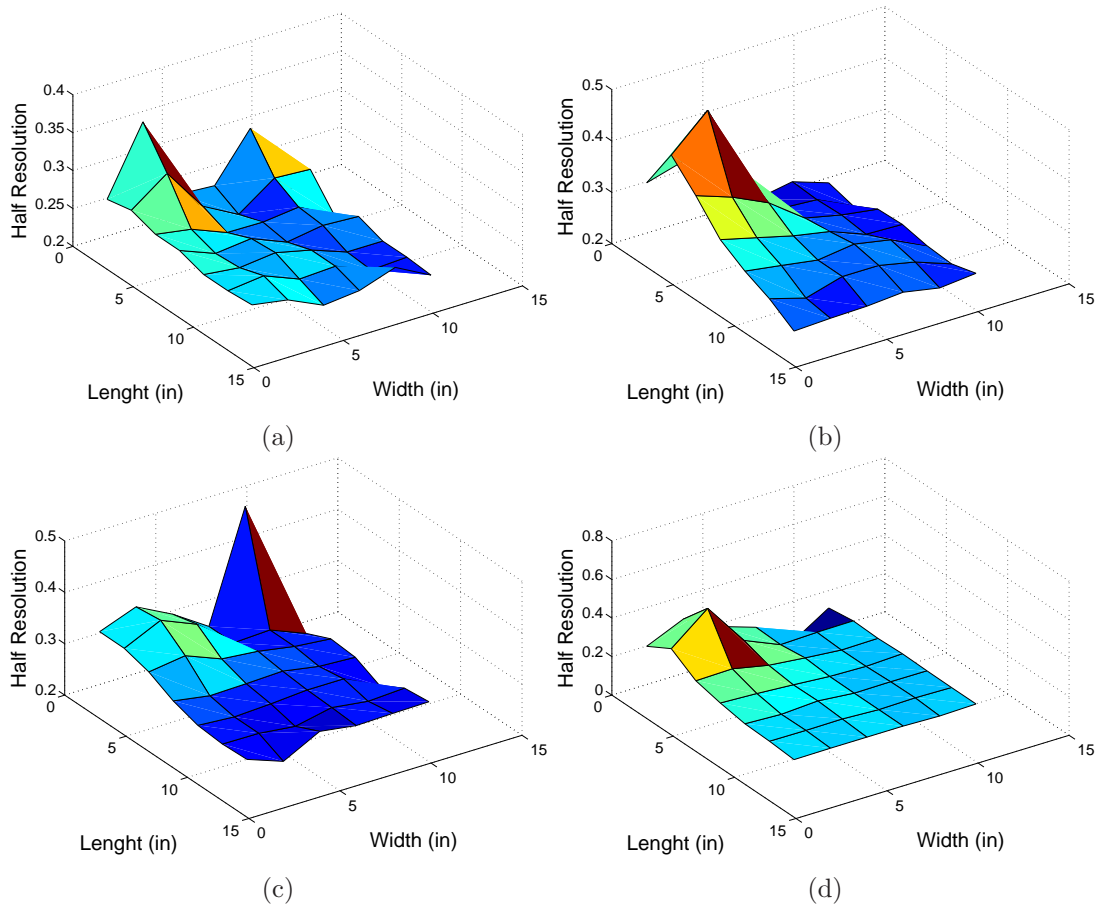
Figure 17: Fractional resolution of the Compton edge: (a) factory wrapped BC-408; (b) researcher wrapped BC-408; (c) factory wrapped EJ-200; and, (d) researcher wrapped EJ-200.
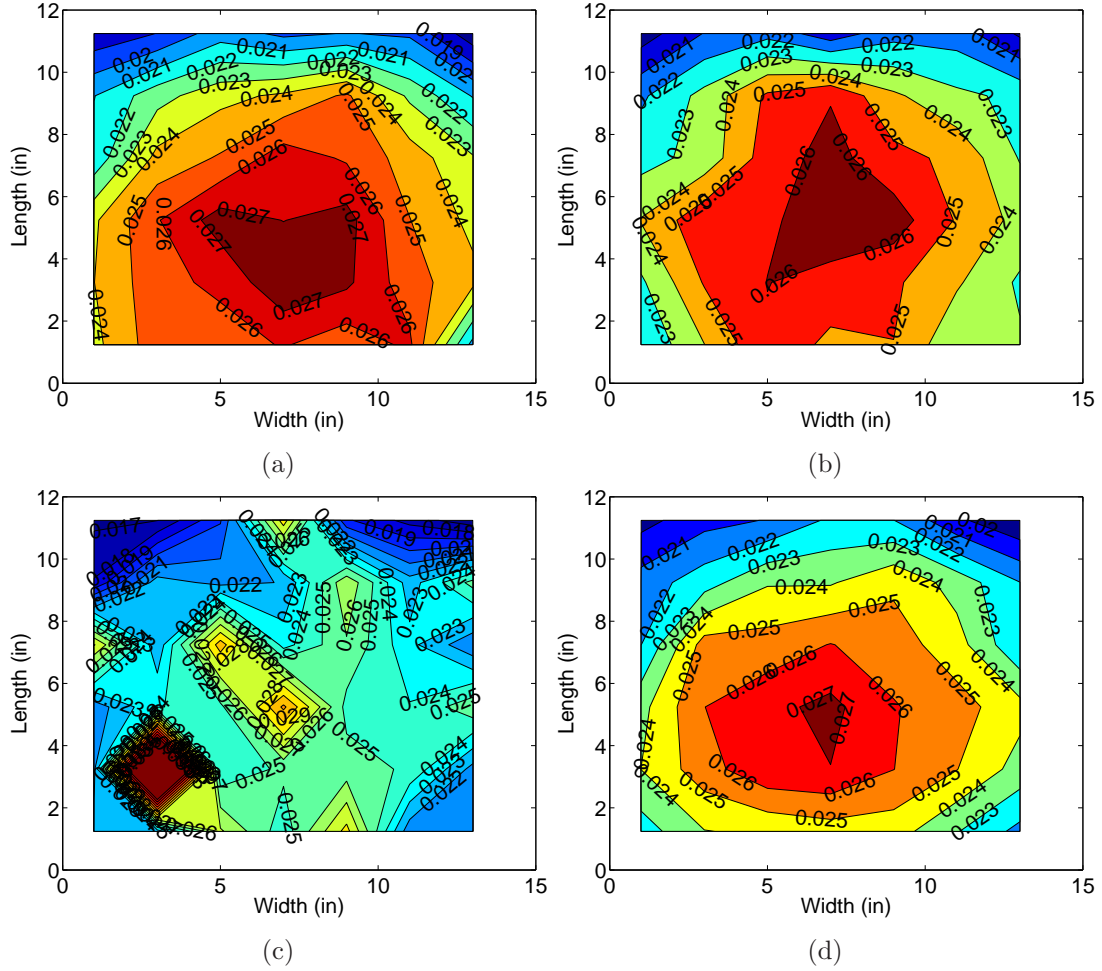
Figure 18:   Percent absolute efficiency of scintillator panels by position: (a) factory wrapped BC-408; (b) researcher wrapped BC-408; (c) factory wrapped EJ-200; and, (d) researcher wrapped EJ-200.
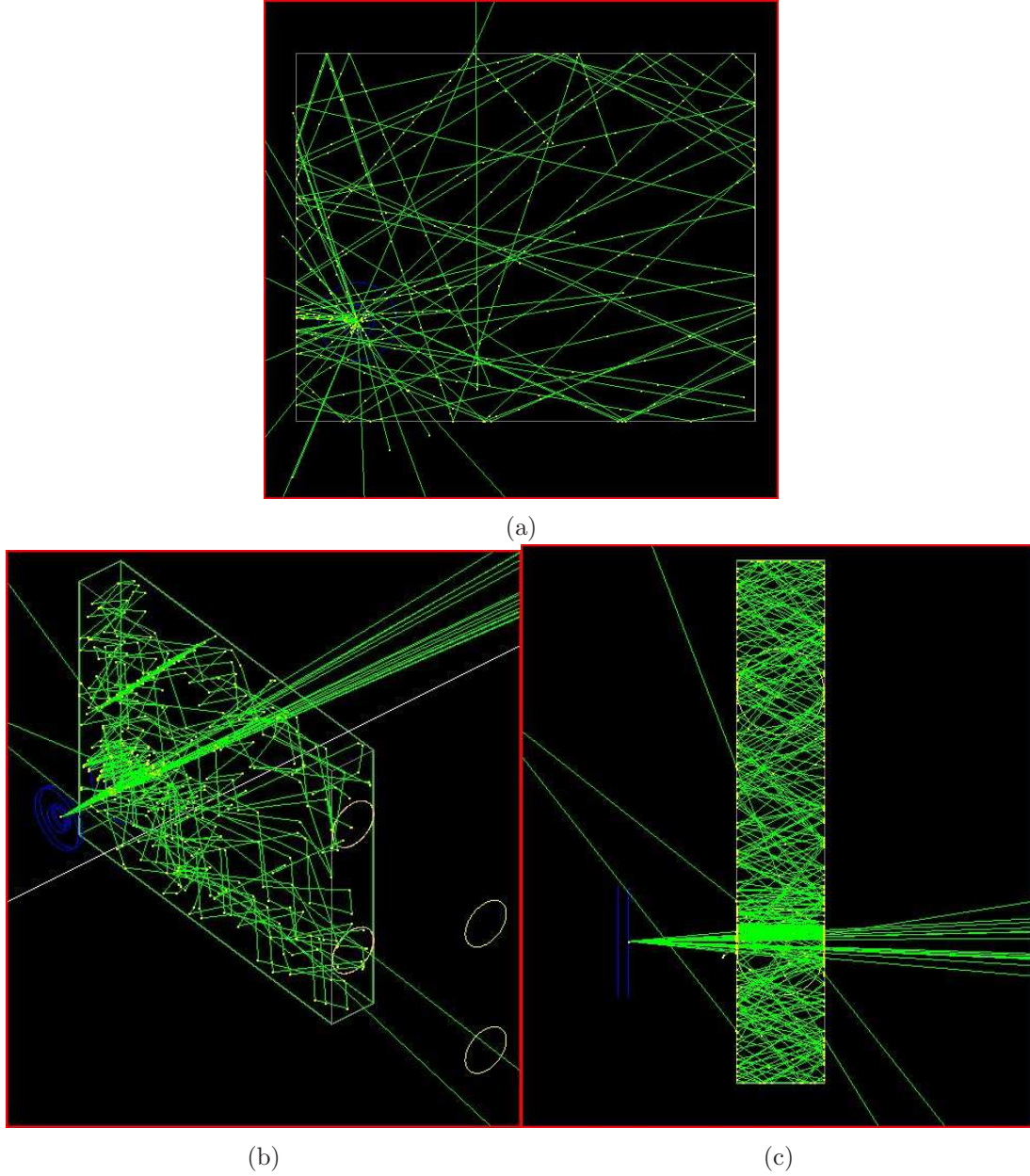
Figure 19: A visualization showing the tracks of twenty $\approx 662keV$ photons incident on a polyvinyl toluene detector: (a) top view; (b) oblique view; (c) side view.
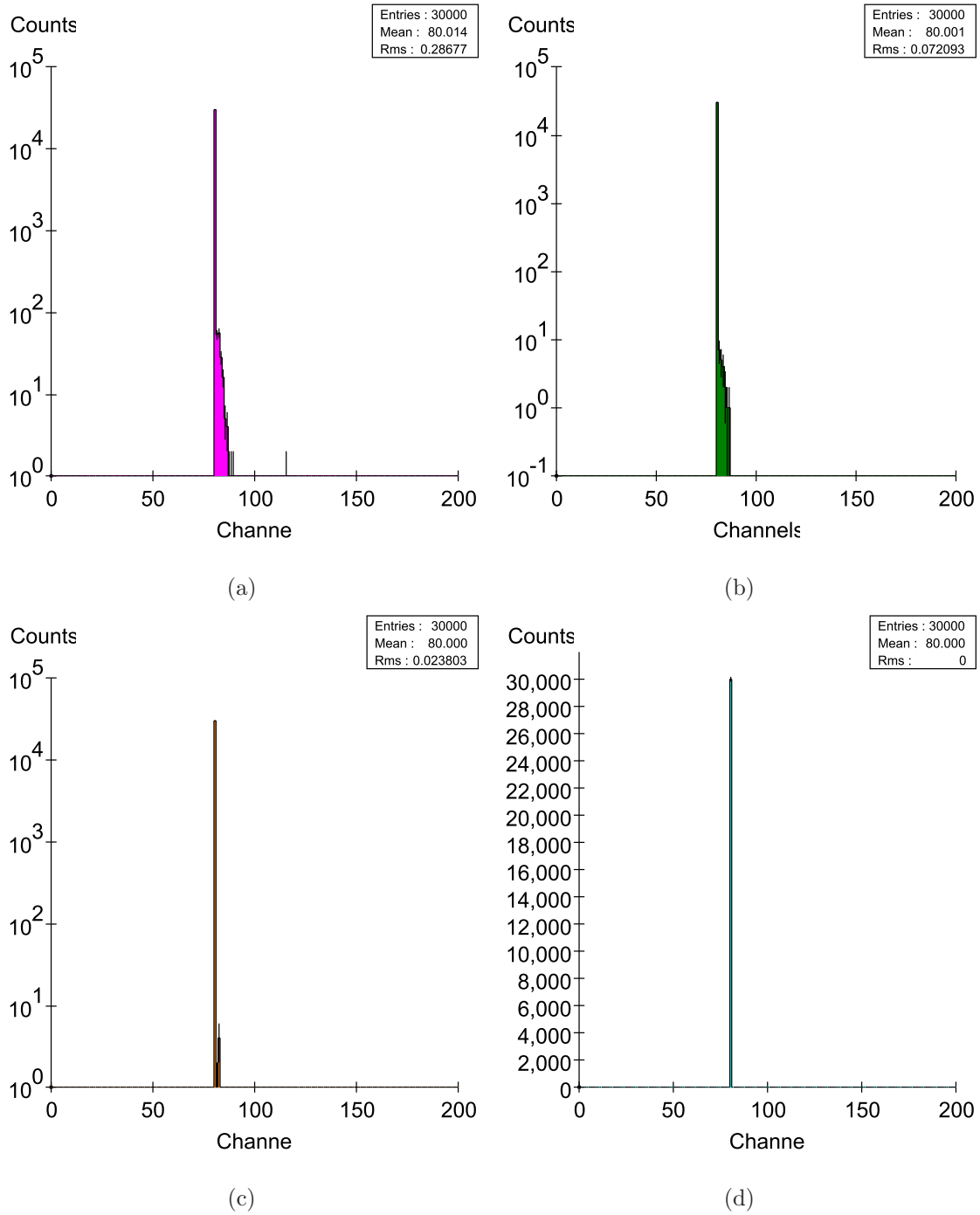
Figure 20: Pulse height spectrum from Geant4 simulations $30000 \approx 662 keV$ photons directed toward an aluminum wrapped PVT scintillator: (a) gun and collimator centered 1 in from the PMT; (b) gun and collimator centered 5 in from the PMT; (c) gun and collimator centered 9 in from the PMT; (d) gun and collimator centered 13 in from the PMT.

56

V. Discussion

5.1 The spectrum

An inspection of a typical pulse-height spectrum, such as the one depicted in Figure 21, reveals some notable features. The *low energy peak* located at channel 44. Then the Compton feature that is located between channel 52 and channel 200. Finally, the counts around channel 1900. The counts centered at about channel 1900 are removed when the background is subtracted. The peak located at about channel 44 peak dominates the data, its magnitude $\backsim 2.7 \times 10^5$ stifles information from the Compton area of the spectrum and shows significant variation with time.

5.2 The Compton Region

The Compton continuum area of the spectrum was considered to be from the end of the large low energy peak to the channel where the counts dropped below 40 per channel. The number of counts in each channel of the Compton region of the spectrum varied with position of the source for each panel. The summation of counts in the Compton region exhibited similar trends, as can be noted in Figure 12. The counts in the Compton region were greater in the center, and diminished closer to the side of the scintillator panel, with local minimums found in the corners. Further, the position that had the maximum counts in the Compton region was not centered on the panel, it was skewed to the side where the PMT was located.

The channel in the Compton region that best approximated the Compton edge was labeled the peak. The "peak" height of the Compton edge also varied across the scintillator panels. Similar to the total counts, the peak-height was higher in the center of the panel, and dropped approaching the sides. A feature of the peak height surface plots is a minimum just in front of the PMT. As stated earlier, although the shape of the Compton feature was fairly consistent, the magnitude of the feature differed. These differences are apparent when comparing the peak heights measured
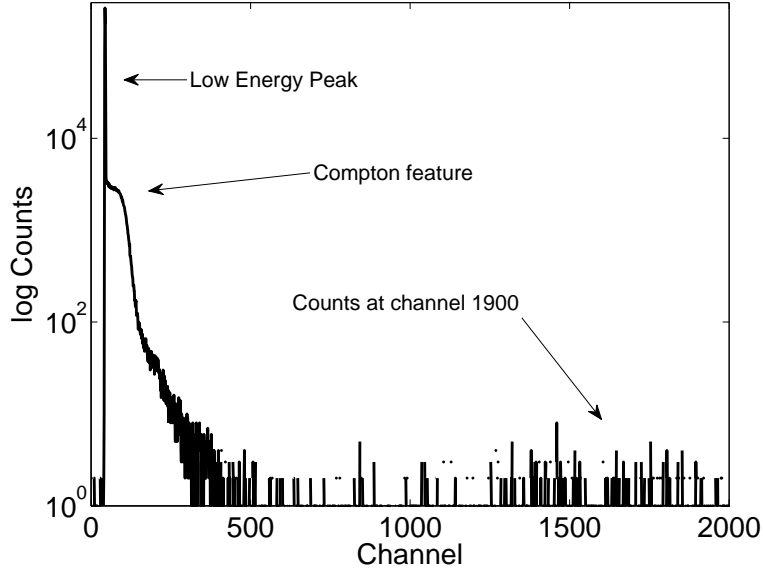
Figure 21:   Typical pulse height spectrum showing three distinct features.

from the researcher wrapped EJ-200 scintillator panel, Figure 14(d) and the peak heights across the other panels.

Resolution varied on the panels but was at its worse close to the PMT. Each panel had a maximum HWHM directly in front of the PMT face. For reference, the HWHM in front of the PMT tended to be 1.5 times that of the remainder of the panel.

The percent absolute efficiency followed similar trends as the Compton region except for the factory wrapped EJ-200 panel seen in Figure 18(c). The peaks measured in this panel can be partially attributed to a time dependant phenomenon. The time dependance is clear in the background subtracted spectra in Figure 22(a).

5.3   Fitting the Data

The features of the efficiency and counts in the Compton region are presumed to result from the PSTS rather than the source. For a sufficiently long half-life source the number of gamma rays are approximately constant. When the source

58
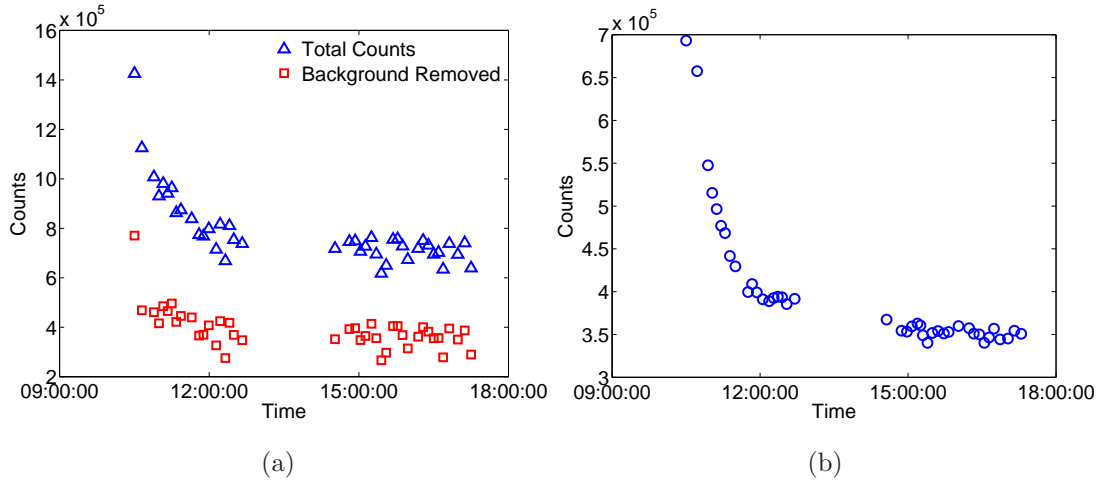
Figure 22:   Both the total counts in the pulse-height and background showed significant time dependant trends; (a) for the pulse-hight spectrum; (b) for the background.

and collimator where placed at different positions it was assumed that the number of counts recorded in the Compton region of the pulse-height spectrum were due to differences in the efficiency of the system rather than differences in the incident radiation.

Since the incident photons were assumed constant during the measurements, the trends in counts recorded must be due to differences in light collection or production. If the scintillation efficiency, in the form of photons produced per MeV of energy, is assumed constant, then the variations in the efficiency, and total counts, must be due to light losses.

The shape of the efficiency contour, Figure 18, and counts in the Compton region, Figure 12, are similar. To understand these loss mechanisms, a simple mathematical model was constructed, where two means of photon escape were considered. First, the light capture fraction was considered via a development that resembles that found in Knoll [21]. A gamma photon entering from one side of the panel is presumed to interact, on average, half way through the panel. If the gamma photon interacts, the scintillation photons are assumed to be emitted randomly over a 4π solid angle.

The assumption was made that the number of scintillation photons created by incident γ radiation was constant over time. The percentage of the emitted scintillation photons that escape the scintillator was presumed to be correlated to the fraction of photons that experienced total internal reflection, and ultimately the critical angle. The development of the light capture fraction in Knoll uses the critical angle to represent the probability of a photon being absorbed after being reflected back and forth numerous times, or escaping without reaching a PMT. The light capture fraction is characterized by the fraction of the solid angle greater than the critical angle, Equation 16,

$$\theta_C = sin^{-1}\left(\frac{n_1}{n_0}\right) \tag{16}$$

with n_1 and n_0 being the refractive indexes of the scintillator wrapper material and the PVT scintillator respectively. The critical angle in Equation 16 is defined with the zero angle normal to the surface.

The probability of a photon escaping the scintillator panel on a side is taken to be the *escape area*, defined by the integration between a positive to negative critical angle. As the collimator and source are moved around the scintillator panel the distance from each of the four sides change. The distance from a side defines not only the area of its projection onto the unit sphere, but the corresponding *escape area*. Therefore, as the collimator and source are moved around the scintillator the *escape area* changes as a function of distance, d. The area of a unit sphere that is covered by the projection of a side of the PVT panel onto a unit sphere is calculated by the ingegration of Equation 17 over the angles ϕ, and θ, with radius r representing the distance the side is from where the scintillation photon is created.

$$A = \int_{\phi o}^{\phi} \int_{\theta o}^{\theta} r^2 sin\theta \, d\theta \, d\phi. \tag{17}$$
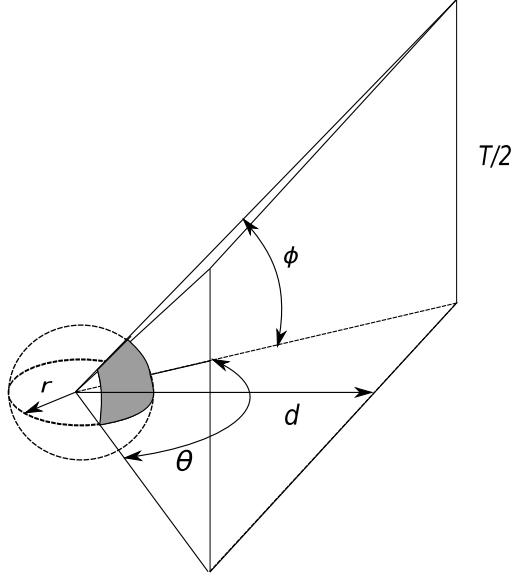
Figure 23:   The projection of a rectangle onto a unit sphere.

The limits of integration are then the angles represented by the edges of the rectangle and the critical angle. The edge of the rectangle is

$$\theta = tan^{-1}\left(\frac{T}{2d}\right) \tag{18}$$

where T is the thickness of the panel, and d is the distance from the side. The total probability of a photon escaping is the the sum of the *escape area* presented by each of the six sides.

The solid angle is defined as $\Omega = A/r^2$. The solid angle can be determined by integrating Equation 19, with the same limits of integration used previously.

$$\Omega = \int_{\phi_C}^{\phi} \int_{\theta_C}^{\theta} sin\theta \, d\theta \, d\phi. \tag{19}$$

The total solid angle presented by the *escape areas* from each side is the sum of the contributions from the individual sides.

$$\Omega_{escape} = \sum_{i=1}^{6} \Omega_i \tag{20}$$

61

The light capture fraction F then ends up being

$$F = 4\pi - \Omega_{escape}. \tag{21}$$

Though the majority of photon loss can be accounted for by the solid angle differences, an additional loss mechanism is apparent by the skewing of the total counts contours.

Some loss of light by attenuation is apparent through the skewed nature of the total counts contour. Considering only the Compton region of the spectrum, the proximity to the PMT seems to influence the total counts recorded. A widely used model of the attenuation by the bulk scintillator as a function of distance is

$$\frac{I}{I_0} = e^{-x/L}, \tag{22}$$

were I/I_0 is the fractional intensity, L is the attenuation length and x is the distance from the PMT.

The multiplicative effects of these two loss effects results in a contour that looks similar to those observed. A graphical representation of the two loss mechanisms is presented in Figure 24.

A second model was constructed to include quadratic and multiplicative effects of both the fractional solid angle and attenuation, as shown in Equation 23,

$$y = \beta_0 + \beta_1 F + \beta_2 \left(\frac{I}{I_0}\right) + \beta_3 F^2 + \beta_4 \left(\frac{I}{I_0}\right)^2 + \beta_5 F \left(\frac{I}{I_0}\right). \tag{23}$$

A fit to the data yielded regression coefficients values presented in Table 10. The R^2 was found to be 0.49 indicating that the model accounts for approximately 49% of the variation. The F statistic 8.891 with a p-value that is < 0.0001 indicates that it is highly unlikely that all of the regression coefficients are zero. A plot of the residuals is shown in Figure 26.
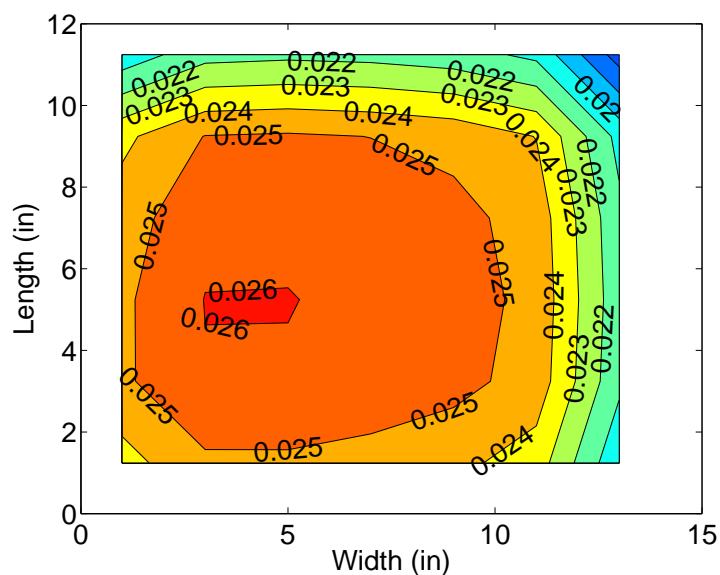
Figure 24:   Modeled effects of the self attenuation and loss of scintillated light.

Table 10:   Factors obtained from a linear multiple linear regression

Factor	Value
β_0	-2.1469
β_1	-0.0602
β_2	4.5821
β_3	0.0033
β_4	-2.4029
β_5	0.0481

5.4   Statistics

The statistics associated with the pulse-height spectrum do not support confident assertions of comparisons. The stated goal of this research was to make comparisons between different scintillator panels. Confidence and rigor regarding comparisons between panels need to be stated using commonly used statistics. Typical, comparison of spectroscopic quality or response efficiency are made with the aid of an assumed probability density function. Once a distribution is known or assumed, statistics based on the distribution allow for the development of assertions about the
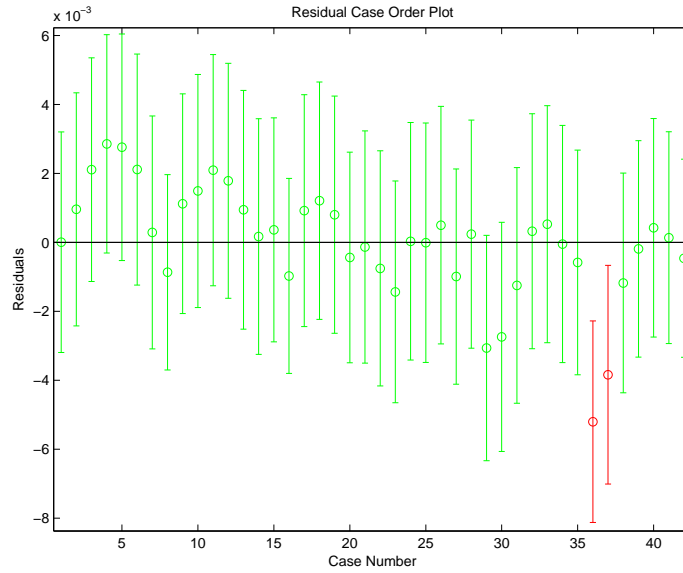
Figure 25:   The residuals from a multiple linear regression of model of total counts in Compton region of the spectrum.

Figure 26:   The residuals from a multiple linear regression of model of total counts in Compton region of the spectrum.

data. The theoretical probability distribution of a photo-electric peak is frequently assumed to be either Gaussian or Poisson.

If this is the case then the mean of the distribution is the mean of a single measurement [21]. The assumed distribution leads to a predicted variance σ^2 that is equal to the sample variance s^2. For a single measurement with n counts, the standard deviation is taken to be $\sqrt{n}$, such that the error associated with a single measurement is equivalently $\sqrt{n}$. Once the standard deviation is known it can be used to express confidence that the true mean is equal to the sample mean. Here, knowledge of the probability distribution function is used. In a Gaussian distribution 68% of the values are within one standard deviation of the mean. The probability that the mean would be inside the interval $\bar{x} + \sigma$ and $\bar{x} - \sigma$ is the 68% confidence interval. In addition to the single standard deviation confidence interval, (CI), the entirety of the Gaussian probability distribution is tabulated such that a confidence interval can be constructed for any probability using the standard deviation. Said

64

another way, if the probability distribution of data is Gaussian there is a 90% probability that the true mean lies within the interval $\bar{x} + 1.64\sigma$ and $\bar{x} - 1.64\sigma$. In this manner, a confidence in a particular measurement such as number of counts recorded in a peak is developed.

The *low energy peak* centered at channel 44 is the only feature of the pulse-height spectrum with a shape that fits a Gaussian or Poisson distribution. In an effort to validate the $\sqrt{n}$ assumption of the standard deviation, several experiments where preformed in which the source was placed at a given location and a pulse height spectrum recorded. After taking the spectrum with the source in place it was removed and a background spectrum recorded. Multiple iterations of this experiment were performed. The results of these experiments are shown in Table 11.

Table 11:   The variation in peak height

Peak Location	Mean Peak Height	$\sqrt{Mean}$	Standard Deviation
Channel 44	302915	550	124191
Channel 44	274308	523	48027
Channel 44	171327	413	82423

The error in the pulse-height spectrum was determined by recording multiple spectra with the source and collimator at the same position. The error was determined by taking the variance of each channel. Similarly, multiple background spectra where recorded and the variance was taken channel-by-channel, as

$$\sigma_{i,bs}^2 = \sigma_{i,p}^2 + \sigma_{i,b}^2, \tag{24}$$

were i is the channel, $\sigma_{i,bs}^2$ is the variance in the background subtracted pulse-height spectrum, and $\sigma_{i,p}^2$, and $\sigma_{i,b}^2$ are the variance in the spectrum and background respectively. The resulting error per channel was then used to determine the error in the background subtracted pulse-height spectrum. For summed data, the error is equal

to the sum of the error in the individual measurements,

$$\sigma_{bs}^2 = \sum_{i=1}^{N} \sigma_{i,bs}^2, \tag{25}$$

were the variance, σ_{bs}^2 is the variance in the summed counts per channel. The differences between the error in the measurement and what would be expected using standard counting statistics are shown in Table 12.

Table 12:   The variation in peak height

	Variance	Standard Deviation
Measured Pulse-Height	3.2×10^7	5720
Measured Background	1.5×10^7	3922
Gaussian Pulse-Height	7865	89
Gaussian Background	4793	69
Experimental Background Subtracted	3.2×10^7	6935
Gaussian Background Subtracted	12659	112

A z-test was completed for each channel in a set of experiments. A set of experiments being multiple 1 min spectrum and an accompanying background with the source and collimator are placed at the same position. The channels with a non-zero mean failed to reject the null hypothesis that the true mean of the set of experiments was different from the sample mean at an $\alpha=0.05$ or 95% confidence interval. Thus underscoring that none of the channels had statistics that matched Gaussian or Poisson counting statistics.

The error in the measurement deviated significantly from the error expected from a Poisson process, or variability in the decay of a radio nuclide. This points toward the need to identify other sources of variability in the measurements.

5.5   Simulated Pulse Height Spectrum

The simulations reinforced several of the key physical phenomenon. The dramatic peak at the lower end of the spectrum was present in the simulated pulse-height

spectra as well as the Compton scattering features. The presence of the Compton features diminished as the source was moved further from the PMT face, but the lower energy peak is maintained as a strong feature in the spectrum.

Though the main features of the pulse height spectrum where represented the simulation had a noticably smaller Compton region of the pulse height spectrum. The simulated spectrum is the combined effect of each of the parameters listed in Section 3.16.2, each of which could be manipulated to yield a pulse-height spectrum that was more representative of those recorded in the laboratory.

The effects of self attenuation were modeled using the photon absorption data from NIST [4]. The absence of a Compton region in the spectrum from the simulated source placed 13 inches from the PMT face indicates that the absorption lengths may be shorter than they are physically. More accurate pulse-height spectrum could be obtained with a more accurate attenuation length description.

5.6 Conclusion

The variability in the efficiency and resolution varied significantly across the panels. The trends that were observable were, by inspection, similar, though notably different in magnitude. Some of the variability in the counts, both of the total spectrum, and in the Compton feature can be accounted for using a variation on the *Light Capture Fraction* theme developed in Knoll [21] and elsewhere. The variability in the data was not effectively modeled by standard Poisson statistics. The magnitude of the variability makes assertions of quality, or comparisons between panels tenuous, if not imprudent.

VI. Recommendation

There are several issues with performing this type of analysis. It should be understood that the efficiency of the scintillator is expected to vary across the panel, simply by virtue of the geometry. The material is not-well suited for high resolution detection. The system used does not have sufficient resolution to ascertain differences in performance between panels.

The efficiency is expected to vary, based on the geometry. If scintillation photons are generated they are expected to have a certain probability of escape based on the fraction of the 4π solid angle that is covered by total internal reflection. To decrease the geometric losses the scintillator panel should be constructed to minimize these effects.

The best resolution available from the Compton region of the pulse-height spectrum does not allow for effective determination of Compton edge energy, and as such the spectroscopic information is limited.

The variability in the efficiency of the system was dramatic. The sources of this variability are uncertain and must be resolved to make any meaningful comparison between scintillator panels from different sources. The total counts recorded, both in the pulse-height spectrum and the background, had significant time dependance. Since the major changes in total counts happened in the first two hours (Figure 22), it may have been advantageous to turn on the system two or three hours before taking any measurements.

Several techniques are available that may improve the resolution of a similarly constructed system. Some of the techniques include using a coincidence timing circuit, stacking scintillator panels to use in a coincidence circuit, or using a combination of both.

A pulse-shape analyzer uses the shape of the pulse to generate a timing signal. If two PMT's where placed at opposite ends of the scintillator panel, a timing pick-off circuit could be constructed to record the leading pulse of a scintillation pulse rejecting any pulse with a different shape by means of a coincidence module. The value to this technique would be realized in the reduction of secondary and tertiary pulses from the internally reflected scintillation photons.

A second use of a coincidence circuit would be to place two identically wrapped scintillator panels back to back. If an appropriately shaped pulse from the first scintillator was used to produce a gate to the second scintillator, a reduced pulse-height spectrum would result. The pulse-height spectrum would have notably fewer total counts but a greater percentage of the counts would be from gamma interactions. Not all of the background would be removed with this technique, but the lower energy pulses would be dramatically reduced.

Further insight into the source of the interaction fluctuations in the pulse-height spectrum could be garnered from performing experiments on a shielded scintillator. One technique could be to wrap the scintillator with layers of appropriate material to attenuate lower energy photons. Another might be to perform the experiments in a lead coffer to attenuate all but the most energetic radiation in the background. Either of these techniques would help to decipher whether the tremendous variability in total counts is due to electronics, background, or scintillator.

Appendix A. Geant4 Simulation Primer

The Geant4 Toolkit is a resource for simulating particle movement through matter. Its applications range from high energy physics to nuclear and accelerator physics [5].

The Toolkit is a complete set of tools for simulating detectors. The physical processes that can be simulated using the Geant4 Toolkit read like a laundry list of high energy physics. Its utility derives from its common interface and provided utilities. It includes built in handling of all manner of particles Bosons, Leptons, Mesons and Baryons. It can handle all kinds of processes to include photoelectric effect; internal conversion; and Compton; Rayleigh; and multiple scattering; ionization; Bremsstrahlung; Cerenkov; scintillation; optical absorption; fluorescence; boundary processes and radioactive decay.

It provides built in resources for handling the detector geometry, material definition, event generation, and particle tracking through materials in the midst of electromagnetic fields, the visualization of geometry and particle tracks as well as recording and displaying of simulation data, with a convenient user interface. These features come in a well documented package with copious examples, easy to use random number generators, physics unit conversions, and particle management that is consistent with the Particle Data Group's practice [3]. In addition, it implements recent advances in software engineering with object-oriented structures designed to make the physics transparent to the user and separate the minutia of software development from the application developer. The architecture affords the user the ability to customize or extend the toolkit as well. Further the object oriented structure allows the user to cherry pick the components needed.

Its development was through the cooperation of approximately 100 scientists spread across Europe, Russia, Japan, Canada and the US. The source code is freely available and downloadable from the internet. Its installation is supported with detailed installation guides, and application development is supported with a User

Forum [1] and User Guide [2] that can guide the new application developer through any manner of difficulty.

A.1 Set Up

Since Geant4 is a C++ based tool kit it can be run on any of the major operating systems. The installation guides are located at

http://geant4.slac.stanford.edu/installation/.

The Unix/Linux operating systems make use of the GNU C++ compiler. The only approved C++ compiler for Geant4 on windows systems is the Microsoft® C++ compiler. The compiler is available either in the free Visual C++ Express Edition, or as a package in the the full blown Visual Studio suite.

Since the Geant4 Toolkit is designed to be cross-platform, making a consistent user interface is important. Linux and Unix users will be familiar with the interface presented by the shell commands used to install, compile, and run the Geant4 simulation. Windows users will need to download and install a Linux shell emulator *cygwin*. The Geant4 installation guide walks the user through all the required steps.

Before running the first example it is important to understand some of the structure behind Geant4. Geant4 is divided into two pieces, for purposes of this primer the pieces will be referred to at the Toolkit and the Simulation. The Toolkit is a mammoth application which is downloaded as source code and compiled as-is on the machine it will be used. Some advantages to compiling the code on the local machine are the ability to include the locally installed software and making code that is appropriately compiled for multi-processor execution. The user does not make changes to the Toolkit, except to indicate the location and type of local software. The Toolkit is where all the physics management occurs. The simulation is a separate application that "specifies" the detector and physical processes. Specifying the detector includes indicating the material composition, density, optical properties and physical processes. The Simulation is also compiled to produce a separate

application which calls the compiled Geant4 Toolkit as it executes, and feeds it the structure and physical processes of interest. In this way a wide variety of particle interactions are available to the user without worrying about how to write the code to model the process. The focus of this primmer is to aid the first time detector developer in implementing a new simulation.

The first step in making a functional simulation is to compile and run one that already exists. Veteran software developers may not need such practice, but the novice will find the instructions invaluable.

A.2 Making a Model

Making a simulation can be a daunting task for a beginner, so the Geant4 community has constructed several fully functional example simulations and made them available as source code to aid learning. The first step in setting up a model is to review the example simulations provided. The examples are located in the "examples" folder in the root Geant4 directory e.g. `C:\Geant4\geant4_9_1\examples` where `C:\Geant4` would be the users root Geant4 directory, and `geant4_9_1` would be the appropriate distribution. A short description of the included examples is available in Tables 13, 14, and 15. Beyond the cursory description given here, each example has a `README` text file. It explains what the example does and how to run it. Once an appropriate example is chosen one must construct a detector.

Table 13:   Geant4 Novice Examples

Example	Brief Description
ExampleN01	minimal set for geantino transportation
ExampleN02	fixed target tracker geometry
ExampleN03	EM shower in calorimeter
ExampleN04	simplified collider geometry
ExampleN05	parametrised shower example
ExampleN06	Optical photon example
ExampleN07	Cuts per region

Table 14:   Geant4 Extended Examples

Purpose	Example
Check basic quantities	
Total cross sections, mean free paths ...	Em0, Em13, Em14
Stopping power, particle range ...	Em0, Em1, Em5, Em11, Em12
Final state : energy spectra, angular distributions	Em14
Energy loss fluctuations	Em18
Multiple Coulomb scattering as an isolated mechanism	Em15
as a result of particle transport	Em5
More global verifications	
Single layer: transmission, absorption, reflexion	Em5
Bragg curve, tallies	Em7
Depth dose distribution	Em11, Em12
Shower shapes, Moliere radius	Em2
Sampling calorimeters, energy flow	Em3
Crystal calorimeters	Em9
Other specialized programs	
High energy muon physics	Em17
Other rare, high energy processes	Em6
Synchrotron radiation	Em16
Transition radiation	Em8
Photo-absorption-ionization model	Em10

A.2.1 Constructing the Detector. Geant4 simulations requires the construction of a detector. The detector is an instance of the `G4VUserDetectorConstruction` class. The key components of constructing a detector is first to develop a list of materials. Several techniques are available for defining the materials, and can be readily found in the Geant4 User Manual located at:

http://geant4.cern.ch/support/userdocuments.shtml.

Most materials can be described by first introducing the constituent elements and then describing their relative abundance. For gasses and liquids, it is convenient to define the material as shown below.

```
//---------------------------------------------------------------
// Water
//---------------------------------------------------------------
G4Material* Water =
    new G4Material("Water", density=1.0*g/cm3, nelements=2);
```

Table 15:   Geant4 Advanced Examples

Example	Short Description
`air_shower`	a simulation of the ULTRA detector with Fresnel lenses for UV and charged particles detection in cosmic rays.
`brachytherapy`	illustrating a typical medical physics application simulating energy deposit in a Phantom filled with soft tissue.
`hadrontherapy`	illustrating a application simulating an hadron therapy beam line for medical physics.
`human_phantom`	implementing an Anthropomorphic Phantom body built importing the description from a GDML representation.
`medical_linac`	illustrating a typical medical physics application simulating energy deposit in a Phantom filled with water for a typical linac used for intensity modulated radiation therapy. The experimental set-up is very similar to one used in clinical practice.
`microbeam`	simulates the cellular irradiation beam line installed on the AIFIRA electrostatic accelerator facility located at CENBG, Bordeaux-Gradignan, France.
`purging_magnet`	illustrating an application that simulates electrons traveling through a 3D magnetic field; used in a medical environment for simulating a strong purging magnet in a treatment head.
`radiation_monitor`	illustrating an application for the study of the effects of a chip carrier on silicon radiation monitoring devices used in the LHC environment.
`radioprotection`	illustrating an application to evaluate the dose in astronauts, in vehicle concepts and Moon surface habitat configurations, in a defined interplanetary space radiation environment.
`gammaray_telescope`	illustrating an application to typical gamma ray telescopes with a flexible configuration.
`xray_telescope`	illustrating an application for the study of the radiation background in a typical X-ray telescope.
`xray_fluorescence`	illustrating the emission of X-ray fluorescence and PIXE.
`underground_physics`	illustrating an underground detector for dark matter searches.
`cosmicray_charging`	illustrating an application aimed at simulating the electrostatic charging of isolated test masses in the LISA mission by galactic cosmic ray protons and helium nuclei.
`composite_calorimeter`	test-beam simulation of the CMS Hadron calorimeter at LHC.
`lAr_calorimeter`	simulating the Forward Liquid Argon Calorimeter (FCAL) of the ATLAS Detector at LHC.
`raredecay_calorimetry`	illustrating how to estimate importance of photonuclear reactions for photon inefficiency of calorimeters and compare effectiveness of different absorbers in order to reduce it.
`Rich`	simulating the TestBeam Setup of the Rich detector at the LHCb experiment, testing the performance of the aerogel radiator
`Tiara`	a simulation of the neutron shielding experiment TIARA providing a realistic example for applying geometrical importance sampling

```
        Water->AddElement(H, 2);
        Water->AddElement(O, 1);
```

In situations where percent composition is needed, the code would look like:

```
        //---------------------------------------------------------------------
        // Air
        //---------------------------------------------------------------------
        G4Element* N = new G4Element("Nitrogen", "N", z=7 , a=14.01*g/mole);
        G4Element* O = new G4Element("Oxygen"  , "O", z=8 , a=16.00*g/mole);

        G4Material* Air =
            new G4Material("Air", density=1.29*mg/cm3, nelements= 2);
        Air->AddElement(N, 70.*perCent);
        Air->AddElement(O, 30.*perCent);
```

The optical properties of a material are also described using an optical properties
table

```
        //
        // Emission spectrum from BC408 literature
        //
        const G4int PVTScint_NumEmissEntries = 30;
        G4double PVT_BC408_Emission_Energy[PVTScint_NumEmissEntries] = {
          2.3864*eV,  2.4819*eV,  2.5222*eV,  2.5853*eV,  2.6016*eV,  2.6403*eV,
          2.6516*eV,  2.6919*eV,  2.6977*eV,2.7394*eV,  2.7886*eV,  2.8076*eV,
          2.8203*eV,  2.8332*eV,  2.8593*eV,  2.8726*eV,  2.8859*eV,  2.9062*eV,
          2.9406*eV,  2.9546*eV,  2.9617*eV,  2.9759*eV,  3.0047*eV,  3.0267*eV,
          3.049*eV,  3.0793*eV,  3.1024*eV,  3.1983*eV,  3.2656*eV,  3.4471*eV};


        G4double PVT_BC408_Emission_Intensity[PVTScint_NumEmissEntries]={
          0.02,    0.07,    0.1,    0.17,    0.2,    0.25,    0.3,    0.4,    0.42,
           0.5,    0.6,    0.7,    0.85,    0.9,    0.97,    0.98,    0.995,    0.98,
           0.9,    0.85,    0.8,    0.7,    0.6,    0.5,    0.4,    0.3,    0.2,
           0.1,    0.07,    0.04};

        // Identify how many energy divisions you want to use to
        //    describe the light output from the scintillator
          const G4int PVTScint_NumEntries = 4;

          G4double PVTScintPhot_Energy[] = {2.00*eV,2.87*eV,2.90*eV,3.47*eV};

          G4double RIndexPVT[PVTScint_NumEntries]={ 1.5, 1.5, 1.5, 1.5};
          G4double AbsorptionPVT[PVTScint_NumEntries]=
          {210.*cm, 210.*cm, 210.*cm, 210.*cm};
          G4double ScintilFastPVT[PVTScint_NumEntries]={1.00, 1.00, 1.00, 1.00};
          G4double ScintilSlowPVT[PVTScint_NumEntries]={0.00, 0.00, 1.00, 1.00};

          G4MaterialPropertiesTable* PVTscintillator_mt = new
            G4MaterialPropertiesTable();
          PVTscintillator_mt->AddProperty("RINDEX",PVTScintPhot_Energy, RIndexPVT,
            PVTScint_NumEntries);
          PVTscintillator_mt->AddProperty("ABSLENGTH",PVTScintPhotAbsLength_Energy,
            PVT_Nist_Absorption_Length, PVTScint_NumPhotonEnergies);
          PVTscintillator_mt->AddProperty("FASTCOMPONENT",PVT_BC408_Emission_Energy,
            PVT_BC408_Emission_Intensity, PVTScint_NumEmissEntries);
          PVTscintillator_mt->AddProperty("SLOWCOMPONENT",PVT_BC408_Emission_Energy,
            PVT_BC408_Emission_Intensity, PVTScint_NumEmissEntries);
          PVTscintillator_mt->AddProperty("WLSCOMPONENT",PVT_BC408_Emission_Energy,
```

```
   PVT_BC408_Emission_Intensity,PVTScint_NumEmissEntries);
PVTscintillator_mt->AddConstProperty("WLSTIMECONSTANT", 0.5*ns);
PVTscintillator_mt->AddConstProperty("SCINTILLATIONYIELD",10.57/keV);
PVTscintillator_mt->AddConstProperty("RESOLUTIONSCALE",2.0);
PVTscintillator_mt->AddConstProperty("FASTTIMECONSTANT", 2.1*ns);
PVTscintillator_mt->AddConstProperty("SLOWTIMECONSTANT",10.*ns);
PVTscintillator_mt->AddConstProperty("YIELDRATIO",0.8);


PVTscintillator->SetMaterialPropertiesTable(PVTscintillator_mt);
```

Once the materials are defined, the geometry can be set up. First, the room where the detector will be located is defined.

```
//--------------------------------------------------------------------
// The experimental Hall
//--------------------------------------------------------------------
G4double expHall_x = 3*m;
G4double expHall_y = 3*m;
G4double expHall_z = 3*m;
G4Box* expHall_box = new G4Box("World",expHall_x,expHall_y,expHall_z);

G4String name;
G4Material *Air = G4Material::GetMaterial(name = "Air");

G4LogicalVolume* expHall_log
  = new G4LogicalVolume(expHall_box,Air,"World",0,0,0);

G4VPhysicalVolume* expHall_phys
  = new G4PVPlacement(0,G4ThreeVector(),expHall_log,"World",0,false,0);
```

Next the logical volume needs to be created.

```
//--------------------------------------------------------------------
// The Scintillator Panel
//--------------------------------------------------------------------
G4double panel_x = (0.381/2.0)*m;  // 15 inch
G4double panel_y = (0.3048/2.0)*m; // 12 inch
G4double panel_z = (0.0508/2.0)*m; // 2 inch
G4Box* PVTScintPanel_box = new G4Box("PVTScintPanel",
  panel_x,panel_y,panel_z);

G4Material *PVTScintillator = G4Material::GetMaterial(
  name = "PVTScintillator");
G4Material *PMMA = G4Material::GetMaterial(name = "PMMA");

// G4LogicalVolume* PVTScintPanel_log
//    = new G4LogicalVolume(PVTScintPanel_box,PVTscintillator,"PVTScintPanel",0,0,0);

G4LogicalVolume* PVTScintPanel_log
  = new G4LogicalVolume(PVTScintPanel_box,PMMA,"PVTScintPanel",0,0,0);
```

The physical volume needs to be constructed next. Note that in this case the physical PVT panel exists inside the `AlWrapper_log` logical volume.

```
G4double PVTPanelPos_x = Al_Thicknes;
G4double PVTPanelPos_y = 0.0;
```

```
G4double PVTPanelPos_z =0.0;

G4VPhysicalVolume* PVTScintPanel_phys
  = new G4PVPlacement(0,G4ThreeVector(PVTPanelPos_x*m,PVTPanelPos_y*m,
  PVTPanelPos_z*m),PVTPanelPos_log,"PVTScintPanel",AlWrapper_log,
  false,0);
```

Next the volumes that will record hits need to be identified by making them *sensitive detectors*.

```
G4SDManager* SDman = G4SDManager::GetSDMpointer();
G4String SDname;
KsDtrPMTSD* PMT1SD = new KsDtrPMTSD("PMT1");
SDman->AddNewDetector( PMT1SD );
PMT1_log->SetSensitiveDetector(PMT1SD);
KsDtrPMTSD* PMT2SD = new KsDtrPMTSD("PMT2");
SDman->AddNewDetector( PMT2SD );
PMT2_log->SetSensitiveDetector(PMT2SD);
```

It is convenient to add some color to the visualizations so different surfaces can be distinguished.

```
G4VisAttributes * lightGray= new G4VisAttributes(
  G4Colour(178/255. , 178/255. , 178/255. ));
Al_on_PMT_Side_log ->SetVisAttributes(gray);
```

Then the interaction between between two volumes needs to be described.

```
G4OpticalSurface* PMT1_PVT_OG_OpSurf = new G4OpticalSurface("PMT1_PVT_OG");

G4LogicalBorderSurface* PMT1_PVT_OG_BrdrSurf =
                        new G4LogicalBorderSurface(
                        "PMT1_PVT_OG_BrdrSurf", //name
                        PVTScintPanel_phys, //physical volume 1
                        PMT_Window1_phys, // physical volume 2
                        PMT1_PVT_OG_OpSurf); // surface

G4double sigma_alpha = 0.1 ;

PMT1_PVT_OG_OpSurf->SetType(dielectric_dielectric);
PMT1_PVT_OG_OpSurf->SetFinish(polished);
PMT1_PVT_OG_OpSurf->SetModel(unified);
PMT1_PVT_OG_OpSurf->SetSigmaAlpha(sigma_alpha);

const G4int NUM = 2;

G4double pp[NUM]              = {1.84*eV,4.08*eV};
G4double specularlobe[NUM]    = {1., 1.};
G4double specularspike[NUM]   = {0., 0.};
G4double backscatter[NUM]     = {0., 0.};
G4double rindex[NUM]          = {1., 1.};
G4double reflectivity[NUM]    = {0.95, 0.95};
G4double efficiency[NUM]      = {0.0, 0.0};

G4MaterialPropertiesTable* OptSurfTbl = new G4MaterialPropertiesTable();

OptSurfTbl->AddProperty("RINDEX",pp,rindex,NUM);
```

```
OptSurfTbl->AddProperty("SPECULARLOBECONSTANT",pp,specularlobe,NUM);
OptSurfTbl->AddProperty("SPECULARSPIKECONSTANT",pp,specularspike,NUM);
OptSurfTbl->AddProperty("BACKSCATTERCONSTANT",pp,backscatter,NUM);
OptSurfTbl->AddProperty("REFLECTIVITY",pp,reflectivity,NUM);
OptSurfTbl->AddProperty("EFFICIENCY",pp,efficiency,NUM);

PMT1_PVT_OG_OpSurf->SetMaterialPropertiesTable(OptSurfTbl);
```

A.2.2 Sensitive Detectors. Any object with a physical volume can be made into a sensitive detector. The sensitivity refers to its ability to register a hit from a particle. The sensitive detector is an instance of the `G4VSensitiveDetector` class. Its main features are the initialization of the hits collection, and what it does to respond to hits. The hits collection construction is as follows.

```
void KsDtrPMTSD::Initialize(G4HCofThisEvent* HCE)
{
G4cout << "Initialize Hits Collection" << G4endl;

// SensitiveDetectorName and collectionName are data members of G4VSensitiveDetector

OpticalHitsCollection =   new KsDtrOpticalHitsCollection
 (SensitiveDetectorName,collectionName[0]);

  if(HCID<0)
  { HCID = G4SDManager::GetSDMpointer()->GetCollectionID(OpticalHitsCollection); }
  HCE->AddHitsCollection(HCID,OpticalHitsCollection);

  // fill calorimeter hits with zero energy deposition
  for(int i=0;i<80;i++)
  {
    KsDtrOpticalHit* aHit = new KsDtrOpticalHit(i);
    OpticalHitsCollection->insert( aHit );
  }
}
```

Then the response to being hit by a particle is established.

```
G4bool KsDtrPMTSD::ProcessHits(G4Step* aStep,G4TouchableHistory*)
{

 G4cout << "Process Hits" << G4endl;
G4double  kineticEnergy = aStep->GetTrack()->GetKineticEnergy();
if(kineticEnergy==0.) return true;

G4StepPoint* preStepPoint = aStep->GetPreStepPoint();
G4ThreeVector HitPosition  = aStep->GetPreStepPoint()->GetPosition();
G4TouchableHistory* theTouchable
    = (G4TouchableHistory*)(preStepPoint->GetTouchable());
G4VPhysicalVolume* thePhysical = theTouchable->GetVolume();
G4int copyNo = thePhysical->GetCopyNo();
// Get Material

G4String thisVolume = aStep->GetTrack()->GetVolume()->GetName() ;
G4String particleName = aStep->GetTrack()->GetDefinition()->GetParticleName();
G4cout <<  thisVolume << "Hit " << kineticEnergy/MeV << " (MeV)" << G4endl;
```

```
//if (thisVolume != "PMT1" && thisVolume != "PMT2") return false;
//if (particleName != "opticalphoton" ) return false;

//if(particleName == "opticalphoton") aStep->GetTrack()->SetTrackStatus(fStopAndKill);

KsDtrOpticalHit* OpticalHit = new KsDtrOpticalHit ;
OpticalHit->SetEnergy(kineticEnergy);
OpticalHit->SetPosition(HitPosition);

OpticalHitsCollection->insert(OpticalHit);

#ifdef ULTRA_VERBOSE
 G4cout << "******************************" << G4endl;
 G4cout << "             PMT HIT          " << G4endl;
 G4cout << "  Volume:                     " << thisVolume << G4endl;
 G4cout << "  Photon energy (eV) :        " << kineticEnergy/KeV << G4endl;
 G4cout << "  POSITION (mm) :             "
       << HitPosition.x()/mm << " " << HitPosition.y()/mm << " " << HitPosition.z()/mm << G4endl;
 G4cout << "******************************" << G4endl;
#endif

 return true;
}
```

Once the sensitive detector is constructed the definition of a hit needs to be created.

A.2.3 Defining a Hit. Defining a hit requires the extension of the Geant4 class `G4VHit`. The hit class is where the information to be processed is defined, and constructed. An example of the definitions in the "OpticalHit" class follows. The definition section identifies the information that will be available when a hit is registered.

```
const std::map<G4String,G4AttDef>* KsDtrOpticalHit::GetAttDefs() const
{
  G4bool isNew;
  std::map<G4String,G4AttDef>* store
    = G4AttDefStore::GetInstance("KsDtrOpticalHit",isNew);
  if (isNew) {
    G4String HitType("HitType");
    (*store)[HitType] = G4AttDef(HitType,"Hit Type","Physics","","G4String");

    G4String ID("ID");
    (*store)[ID] = G4AttDef(ID,"ID","Physics","","G4int");

    G4String Energy("Energy");
    (*store)[Energy] = G4AttDef(Energy,"Energy Deposited","Physics","G4BestUnit","G4double");

    G4String Pos("Pos");
    (*store)[Pos] = G4AttDef(Pos, "Position",
      "Physics","G4BestUnit","G4ThreeVector");

    G4String LVol("LVol");
    (*store)[LVol] = G4AttDef(LVol,"Logical Volume","Physics","","G4String");
  }
  return store;
```

```
    }
```

Next, the values that where defined need to be created when a hit occurs.

```
std::vector<G4AttValue>* KsDtrOpticalHit::CreateAttValues() const
{
  std::vector<G4AttValue>* values = new std::vector<G4AttValue>;

  values->push_back(G4AttValue("HitType","PMT",""));

  values->push_back
    (G4AttValue("ID",G4UIcommand::ConvertToString(cellID),""));

  values->push_back
    (G4AttValue("Energy",G4BestUnit(edep,"Energy"),""));

  values->push_back
    (G4AttValue("Pos",G4BestUnit(pos,"Length"),""));

  if (pLogV)
    values->push_back
      (G4AttValue("LVol",pLogV->GetName(),""));
  else
    values->push_back
      (G4AttValue("LVol"," ",""));

   return values;
}
```

Once the hit has been defined the event action needs to be defined.

A.2.4   Event Action.   An event is registered when a particle "hits" a sensitive detector. The event action class is an instance of the `G4UserEventAction` class. It first creates a collection for each sensitive detector.

```
G4String colName;
G4SDManager* SDman = G4SDManager::GetSDMpointer();
PMTC1ID = SDman->GetCollectionID(colName="PMT1");
PMTC2ID = SDman->GetCollectionID(colName="PMT2");
verboseLevel = 1;
messenger = new KsDtrEventActionMessenger(this);
```

The next step is to set up the analysis. Below is an example of how to construct a histogram indicating the number of hits and the energy of the hit for two sensitive detectors. The histograms are labeled "`PMT 1 # Hits`", and "`PMT 2 # Hits`". The number of channels is set with the variables `MinChannelHits` and `MaxChannelHits`. A plotter is then constructed for each histogram.

```
if (hFactory)
  {
```

```
G4int MinChannelHits = 0;
G4int MaxChannelHits = 200;
G4int MinChannelEnergy = 0;
G4int MaxChannelEnergy = 1;
G4int Nbins = MaxChannelHits-MinChannelHits;

// Create some histograms
PMT1Hits = hFactory->createHistogram1D(
  "PMT 1 # Hits",Nbins,MinChannelHits,MaxChannelHits);
PMT2Hits = hFactory->createHistogram1D(
  "PMT 2 # Hits",Nbins,MinChannelHits,MaxChannelHits);
Nbins = 100;
PMT1Energy = hFactory->createHistogram1D(
  "PMT 1 Energy",Nbins,MinChannelEnergy,MaxChannelEnergy);
PMT2Energy = hFactory->createHistogram1D(
  "PMT 2 Energy",Nbins,MinChannelEnergy,MaxChannelEnergy);

plotter = analysisManager->getPlotter();
if (plotter)
{
  plotter->createRegions(2,2);
  plotter->region(0)->plot(*PMT1Hits);
  plotter->region(1)->plot(*PMT2Hits);
  plotter->region(2)->plot(*PMT1Energy);
  plotter->region(3)->plot(*PMT2Energy);
  plotter->show();
 }
}
```

Next a Tuple needs to be created to save the information. A Tuple is a generic way to hold data that has been developed by the physics community. Multiple applications can handle, and analyze the Tuple data. Perhaps the easiest to install on a windows based system is JAS3 available through the FreeHEP free ware site,

```
http://jas.freehep.org/jas3/.
```

JAS3 has the advantage over other applications like "OpenScientist" because it does not need to be compiled. Construction of the Tuple can be accomplished in the following way.

```
ITupleFactory* tFactory = analysisManager->getTupleFactory();
if (tFactory)
{
  tuple = tFactory->create("MyTuple","MyTuple","int PMT1Hits, PMT2Hits, double PMT1Energy, PMT2Energy, ","");
}
```

After constructing the necessary parts they can be used by the process hits function. When an event occurs it is placed into the hits collection using the code below.

```
G4HCofThisEvent * HCE = evt->GetHCofThisEvent();

KsDtrOpticalHitsCollection* PMTC1 = 0;
```

```
      KsDtrOpticalHitsCollection* PMTC2 = 0;
      G4int n_hit = 0;
      G4double totEnergyDetect=0., totEnergy=0., energyD=0.;
      if(HCE)
      {
  PMTC1 = (KsDtrOpticalHitsCollection*)(HCE->GetHC(PMTC1ID));
      PMTC2 = (KsDtrOpticalHitsCollection*)(HCE->GetHC(PMTC2ID));
      }
```

The hits then need to be added to the various histograms. One instance for adding
them to the display is shown here.

```
      if (PMTC1 && PMT1Hits) // If collection and hist. exist
      {
        G4int n_hit = PMTC1->entries(); // Get the entries from the PMT1 Hit Coll
        PMT1Hits->fill(n_hit);// This populates the hits histogram
        for(G4int i1=0;i1<n_hit;i1++) // Look at each Hit
        {
  G4double HitEnergy;
  HitEnergy = (*PMTC1)[i1]->GetEnergy() ;
        KsDtrOpticalHit* aHit = (*PMTC1)[i1];
      //  G4ThreeVector localPos = aHit->GetLocalPos();
        if (PMT1Energy) PMT1Energy->fill(HitEnergy/eV);
      }
      }
```

Adding the hit to the Tuple is similar.

```
      if (tuple)
      {
  if (PMTC1) tuple->fill(0,PMTC1->entries());
  if(PMTC1)
        {
          int iHit = 0;
          double totalE = 0.;
          for(int i1=0;i1<80;i1++)
          {
            KsDtrOpticalHit* aHit = (*PMTC1)[i1];
            double eDep = aHit->GetEdep();
            if(eDep>0.)
            {
              iHit++;
              totalE += eDep;
            }
          }
          tuple->fill(2,totalE);
  }
      }
```

A.2.5 The Physics List.   The applicable physics associated with the de-
tector are specified in the implementation of the `G4VUserPhysicsList` class. Con-
structing a physics list is performed via the physics list constructor shown below.

```
      KsDtrPhysicsList::KsDtrPhysicsList() :  G4VUserPhysicsList()
      {
```

```
    theCerenkovProcess            = 0;
    theScintillationProcess       = 0;
    theAbsorptionProcess          = 0;
    theRayleighScatteringProcess = 0;
    theBoundaryProcess            = 0;

    pMessenger = new KsDtrPhysicsListMessenger(this);
    SetVerboseLevel(0);
}
```

The particles of interest are then constructed via the particle constructor function.

```
void KsDtrPhysicsList::ConstructParticle()
{
  // In this method, static member functions should be called
  // for all particles which you want to use.
  // This ensures that objects of these particle types will be
  // created in the program.

  ConstructBosons();
  ConstructLeptons();
}
void KsDtrPhysicsList::ConstructBosons()
{
  // pseudo-particles
  G4Geantino::GeantinoDefinition();
  G4ChargedGeantino::ChargedGeantinoDefinition();

  // gamma
  G4Gamma::GammaDefinition();

  // optical photon
  G4OpticalPhoton::OpticalPhotonDefinition();
}
void KsDtrPhysicsList::ConstructLeptons()
{
  // leptons
  G4Electron::ElectronDefinition();
  G4Positron::PositronDefinition();
  G4NeutrinoE::NeutrinoEDefinition();
  G4AntiNeutrinoE::AntiNeutrinoEDefinition();
  G4MuonPlus::MuonPlusDefinition();
  G4MuonMinus::MuonMinusDefinition();
  G4NeutrinoMu::NeutrinoMuDefinition();
  G4AntiNeutrinoMu::AntiNeutrinoMuDefinition();
}
```

Only the constructors for the Bosons and Leptons are shown.

A.2.6 Particle Generation. The last remaining part is the generation of particles. The primary generator class performs this function. An example of a hard coded position and direction is shown in the KsDtrPrimaryGeneratorAction function.

```
KsDtrPrimaryGeneratorAction::KsDtrPrimaryGeneratorAction()
{
```

```
G4int n_particle = 1;
particleGun = new G4ParticleGun(n_particle);

//create a messenger for this class
gunMessenger = new KsDtrPrimaryGeneratorMessenger(this);

G4ParticleDefinition* particle
        = G4ParticleTable::GetParticleTable()->FindParticle("gamma");
particleGun->SetParticleDefinition(particle);
particleGun->SetParticleTime(0.0*ns);
particleGun->SetParticlePosition(G4ThreeVector(0.0*cm,0.0*cm,6.3*cm));
particleGun->SetParticleMomentumDirection(G4ThreeVector(0.,0.,-1.));
particleGun->SetParticleEnergy(661.7*keV);
}
```

The direction of the gun can be programmatically controlled to give a random gun direction over any solid angle using code like the `GeneratePrimaries` code listed below.

```
void KsDtrPrimaryGeneratorAction::GeneratePrimaries(G4Event* anEvent)
{
  //this function is called at the begining of event
  //distribution uniform in solid angle
  G4double theta = twopi*G4UniformRand(), phi = pi-atan(8./63.)*G4UniformRand();
  G4double sinphi = std::sin(phi);
  G4double ux = sinphi*std::cos(theta),
           uy = sinphi*std::sin(theta),
           uz = std::cos(phi);

  particleGun->SetParticleMomentumDirection(G4ThreeVector(ux,uy,uz));
  particleGun->GeneratePrimaryVertex(anEvent);
}
```

These code snippets by no means represent a complete presentation of the code.

A.3 Running a Simulation

First time users will find that compiling and running some of the example Simulations very useful for demonstrating how the Simulation operates. The installation guide also includes step-by-step instructions for compiling and running simulations. The installation guide can be found at the Stanford Linear Accelerator(SLAC) web site, at

http://geant4.slac.stanford.edu/installation/.

A.3.1 Setting Environmental Variables.   An experienced developer should not have any trouble developing a shell script to set the pertinent environmental

84

variables. For windows users just getting their feet wet with the *Bourne-Again shell* here is a convenient addition to the `env.sh` shell script. The `env.sh` shell script should have been made during the installation process, it should be located in the Geant4 directory e.g. `C:/Geant4/geant4_9_1/env.sh`.

```
G4WORKDIR="d:/g4work"
export G4WORKDIR

JDK_HOME="c:/Java/jdk1.7.0"
export JDK_HOME
echo "JDK_HOME will be set to c:/Java/jdk1.7.0"
JAIDA_HOME="c:/JAIDA/jaida-3.3.0-5"
export JAIDA_HOME
echo "JAIDA_HOME is set to c:/JAIDA/jaida-3.3.0-5"
AIDAJNI_HOME="c:/AIDAJNI/aidajni-3.2.6"
export AIDAJNI_HOME
echo "AIDAJNI_HOME is set to c:/AIDAJNI/aidajni-3.2.6"
source $JAIDA_HOME/bin/aida-setup.sh
echo "Sourced the $JAIDA_HOME/bin/aida-setup.sh"
source $AIDAJNI_HOME/bin/x86-Windows-msvc/aidajni-setup.sh
echo "Sourced the $AIDAJNI_HOME/bin/x86-Windows-msvc/aidajni-setup.sh"
echo "We are done here"
```

Though all of the example applications are located in the `\examples` directory of the Geant4 directory, the user will want to save their work in a "working directory" located elsewhere. For the example shell script, the working directory is located at `d:\g4work`. The Java development kit (jdk) is located at `c:/Java/jdk1.7.0`. "JAIDA" is a Java implementation of the Abstract Interfaces for Data and is available for free compliments of SLAC at

`http://java.freehep.org/jaida/`

as part of the Free HEP code. The JAIDA application resides at `c:/JAIDA/jaida-3.3.0-5`. The installation of AIDAJNI is located at `c:/AIDAJNI/aidajni-3.2.6`. It can be found at

`http://java.freehep.org/aidajni/index.html`.

The location of each of these applications will be different for the user, and are presented only as a reference.

A.3.2 Compiling. Before running a simulation it must be compiled. The installation instructions are very thorough, describing how to compile and run a simulation. The full installation instructions can be found at

http://geant4.slac.stanford.edu/installation/.

Make sure that the working directory is set by attempting to navigate to the `$G4WORKDIR` using the `cd` command. Next, go to the directory where the source code is stored, e.g. `cd KsDtr_like_A01`. The command line should look like `$G4WORKDIR/KsDtr_like_A01/`. Once in the appropriate folder, type `make` to compile the simulation. The shell session should look like the following.

```
kelly@r3-PC ~
$ cd $G4WORKDIR

kelly@r3-PC /cygdrive/d/g4work
$ cd KsDtr_like_A01

kelly@r3-PC /cygdrive/d/g4work/KsDtr_like_A01
$ make
```

Successful compilation will end up in a `... Done!` being displayed at the end. If no `... Done!` appears then something will need to be fixed. The reasons for the unsuccessful compile will be evident from the error messages. The compiled application will be placed in the `$G4WORKDIR/bin/WIN32-VC/` directory, were `WIN32` is a reference to the operating system, and `VC` is a reference to the compiler.

A.3.3 Running The Simulation. The simulation can be run once it is compiled, and while still in the source directory type `$G4WORKDIR/bin/WIN32-VC/KsDtr` where `KsDtr` is the name of the simulation. The application can be run either in interactive or batch mode. The batch mode bypasses the visualization, but executes the analysis. Running a batch file is accomplished by typing the name of the file after the application, as in the following,

$G4WORKDIR/bin/WIN32-VC/KsDtr KsDtr.in,

where `KsDtr.in` is the name of the batch file. The examples automatically place the user in interactive mode and start the visualization by running the `vis.mac` file located in the source directory.

A.3.4 Visualization. All of the example applications open to the interactive mode, then run the `vis.mac`. Note that the `vis.mac` file may need to be opened and updated to reflect the instance of OpenGL for example.

```
#/vis/open HepRepFile
#/vis/open DAWNFILE
/vis/open OGLSWin32
```

The `#` symbol at the beginning of the line indicates a commented line. The interactive mode allows the execution of batch files as well as manipulation of the visualization. Executing the `optPhoton.mac` batch file can be performed by typing the following code line, `/control/execute optPhoton.mac`.

The visualization parameters set in `vis.mac` will set the visualization environment for the "beamOn" command. Typing `/run/beamOn 5` while in the visualization mode will send five previously defined particles in the previously defined direction.

In the interactive mode there are several commands available to manipulate the visual environment. Some that may be useful are listed below.

```
Idle> /vis/viewer/set/viewpointThetaPhi 90 0
Idle> /vis/viewer/set/viewpointThetaPhi
Idle> /vis/viewer/set/viewpointThetaPhi 0 90
Idle> /vis/viewer/set/viewpointThetaPhi 70 20
Idle> /vis/viewer/zoom 8
Idle> /vis/viewer/flush
Idle> /vis/viewer/zoom 3
Idle> /vis/viewer/flush
#
# for drawing the tracks
# Draw trajectories at end of event, showing trajectory points as
# markers of size 2 pixels
Idle> /vis/scene/add/trajectories
Idle> /vis/modeling/trajectories/create/drawByCharge
Idle> /vis/modeling/trajectories/drawByCharge-0/default/setDrawStepPts true
Idle> /vis/modeling/trajectories/drawByCharge-0/default/setStepPtsSize 2
# (if too many tracks cause core dump => storeTrajectory 0)
#
Idle> /vis/scene/endOfEventAction accumulate
#
# Refresh ready for run
Idle> /vis/viewer/refresh
```

```
#/gun/direction 0 0 -1
Idle> /gun/position -13.97 -6.985 6.3 cm
Idle> /gun/particle gamma
Idle> /gun/energy 661.7 keV
Idle> /vis/viewer/refresh
Idle> /tracking/verbose 1
#
# Now ready for /run/beamOn./
Idle> /run/beamOn 5
```

A more complete tutorial of the visualization commands is given in Novice Example 3.

A.3.5   Source Code.   In the interest of brevity the entirety of the Simulation source code is not included in this document. The full set of code can be obtained by contacting:

Department of Nuclear Engineering
2950 Hobson Way
Air Force Institute of Technology
Wright-Patterson AFB, OH 45433-7765
Phone (937)255-3636.

Appendix B.   Scintillation Mechanism

A very thorough treatment of the organic scintillation mechanism is given by Birks [8]. An paraphrase of a significant portion of his chapter follows. The scintillation mechanism is divided into several processes. For ease of discussion they are enumerated as follows:

1 Excitation resulting in excited singlet π-electron states;

2 Ionization of π-electrons;

3 Exciting non-π-electrons (σ-electron and 1s carbon electrons)

4 Ionization of non-π-electron states

5 Internal conversion

6 Fluorescence emission (k_{fx}) of solute X leading to process 8, 11, or 13

7 Internal quenching (k_{ix})

8 Radiative migration ($a_{xx}k_{fx}$) to another solvent molecule X

9 Non-radiative migration (k_{txx}) to another molecule of X

10 Radiative transfer ($a_{xy}k_{fx}$) to a molecule of Y

11 Non-radiative transfer ($k_{txy}[Y]$) to a molecule of Y

12 Escape of solvent emission ($\{1 - a_{xx} - a_{xy}\}k_{fx}$)

13 Primary solute emission (k_{fy})

14 Internal quenching (k_{iy})

The scintillation mechanism can be broken down into two groups. The first grouping is the excitation and the second group is the loss of energy. The excitation group of processes includes the first four processes and can be thought of as the transfer of energy from the ionizing radiation to the solvent. The concentrations of the solutes

are typically too low to undergo direct excitation. The second group is the series of process competing for the energy in the excited solvent molecule. These processes include internal conversion, migration to another solvent molecule, transfer of energy to solute molecules, quenching and radiative emission. Studies by Birks and others have indicated that the scintillation mechanism is virtually independent of the excitation process. Ionizing radiation can result in excitation to excited electronic states,
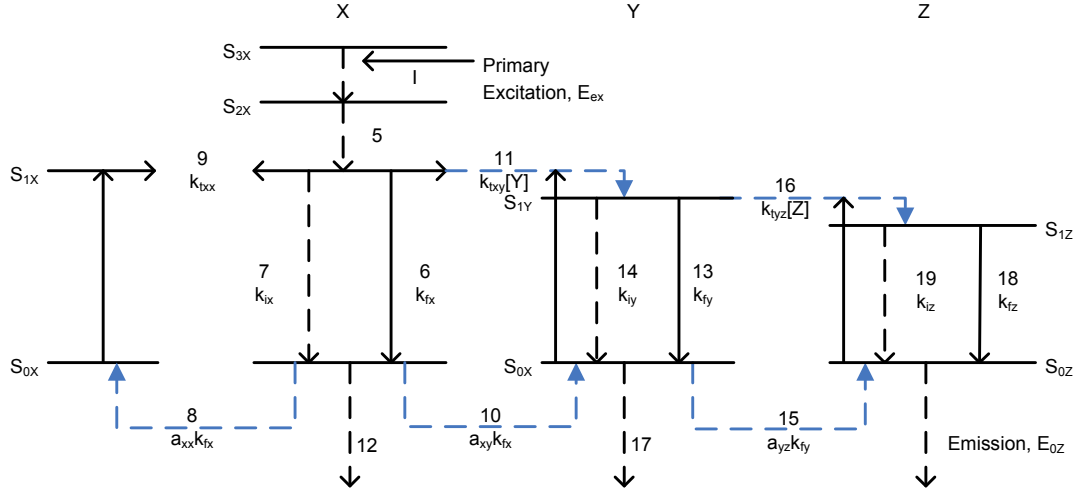

Figure 27:   Diagram of the scintillation process adapted from [8]

and ionization. Excitation into the π-electron excited state is the main source of fast scintillation, process 1. The creation of ions, process 2, results in ion-recombination and results in excited triplet states $\sim 75\%$ of the time, or π-electron excited states for the remainder. The excitation to triplet excited states is strongly forbidden according to quantum mechanical selection rules [25]. As excitation energy increases beyond the S_3 level, excitation of other electrons, i.e. σ-electron and carbon, 1s electrons, process 3, is more prevalent than excitation of π-electrons. The excess energy in the excited non-π-electron states is dissipated thermally without radiation. The ionization of non-π-electrons, process 4, damages the constituent molecules of the scintillator. The damage is dissipated by ion recombination, but when recombination does not occur the damage persists and results in impurity centers. The damage

90

associated with the large ion density along the track of heavier charged particles is believed to be the source of the ionization quenching effect. An effect of long term exposure to ionizing radiation is the gradual increase of impurity centers which diminish scintillation and fluorescence efficiency. A fraction of the energy, P, from a 1 MeV electron will result in the excitation of π-electronic singlet states. Though there are several researchers that suggest different methods of calculating excitation efficiency, Birks recommends a value of $P \sim 0.1$. Excitation typically produces the higher singlet π-excited states, S_{2n}, and S_{3n}. The mean excitation energy can be calculated by

$$E_{ex} = \frac{\mathbf{h} \int \varepsilon_x(\nu) d\nu}{\varepsilon_x(\nu) d\nu}, \tag{26}$$

where the molar extinction coefficient, $\varepsilon_x(\nu)$, at frequency ν while $\mathbf{h}$ is Plank's constant. A convenient approximation gathered through inspection of numerous absorption spectra leads to the approximation $E_{ex} \sim 1.5E_1$. The overall efficiency, Q, of converting the energy, E_{ex}, into fluorescence is then related to the absolute scintillation efficiency S by

$$S = PQ. \tag{27}$$

The first step in the loss of energy process is internal conversion. All organic scintillators undergo internal conversion, which is a non-radiative dissipation of energy of higher level singlet π-electron states to result in a the first excited π-state, S_{1n}. According to Birks it happens with efficiency

$$C = \frac{E_1}{E_{ex}} \sim \frac{2}{3}. \tag{28}$$

A measure of self-absorption is the self-absorption parameter, a_{xx}, and depends on the path length, d, and the amount of overlap of the fluorescence and absorption

spectrum, and is given by the quantity

$$a_{xx} = \frac{\int I_x(\nu)\left[1 - e^{-\varepsilon_x d}\right]}{\int I_x(\nu)d\nu},$$

(29)

where the extinction coefficient of X at frequency ν is ε_x. When the length gets large the absorption tends toward 1.

To facilitate convenient discussion, the solvent species is denoted as X, and the solute species as Y and Z. The mole fraction of the solute components is therefore [Y] and [Z]. The rate parameters, k_f, k_i, and k_t are the rates in $(\sec^{-1})$ of the fluorescence, internal quenching, and non-radiative transfer.

A crystal that is thin and transparent will have a small self-absorption parameter (a_{xx}), resulting in a molecular fluorescence quantum efficiency of X as

$$(q_0 x)_0 = \frac{k_{fx}}{k_{fx} + k_{ix}}.$$

(30)

The average energy of the fluorescence photons is

$$E_{0x} = \frac{\mathbf{h}\int I_x(\nu)d\nu}{I_x(\nu)d\nu},$$

(31)

with the relative quantum intensity, $I_x(\nu)$, of the X at frequency ν. The efficiency of the group of processes involved energy loss for a thin transparent scintillator can be expressed as

$$(Q_x)_0 = \frac{E_{0x}}{E_{ex}}(q_{0x})_0 = C\frac{E_{0x}}{E_{1x}}(q_{0x})_0.$$

(32)

For thick crystals, where absorption is appreciable, the overall efficiency is reduced to yield the technical fluorescence quantum efficiency, q_{px}

$$\begin{aligned}
q_{px} &= (q_{0x})_0(1 - a_{xx})[1 + (q_{0x})_0 a_{xx} + (q_{0x})_0^2 a_{xx}^2 + \cdots] \\
&= \frac{(q_{0x})_0(1 - a_{xx})}{1 - a_{xx}(q_{0x})_0}.
\end{aligned}$$

(33)

The net effect of self-absorption is to reduce the average energy fluorescence photon, $E_{px} < E_{0x}$. The overall efficiency for a thick crystal is then

$$Q_x = C \frac{E_{px}}{E_{1x}} q_{px}.$$

(34)

In addition to the previously defined self-absorption parameter, the absorption fraction absorbed by Y is

$$a_{xy} = 1 - exp(-\bar{\varepsilon}_{xy}[Y]d),$$

(35)

where ε_{xy} is the mean extinction coefficient. The fraction of photons that escape is the escaping fraction $(1 - a_{xx} - a_{xy})$. The low concentration of Y make the self-absorption, a_{yy}, improbable.

For plastics the radiative migration can be neglected $a_{xx}k_{fx}$ with little error. In a binary system the non-radiative transfer process is

$$q_{0x} = \frac{k_{fx}}{k_{fx} + k_{ix} + k_{txy}[Y]},$$

(36)

then producing the technical quantum efficiency of radiative transfer to the species Y as

$$f_{rxy} = a_{xy}q_{0x},$$

(37)

then the technical quantum efficiency of the non-radiative transfer to Y as

$$f_{txy} = \frac{k_{txy}[Y]}{k_{fx} + k_{ix} + k_{txy}[Y]}.$$

(38)

The total quantum efficiency of the energy associated with excitation is

$$f_{xy} = f_{rxy} + f_{txy} = \frac{a_{ax}(q_{0x})_0 + \sigma_{xy}[Y]}{1 + \sigma_{xy}[Y]},$$

(39)

93

with the parameter σ_{xy} defined by

$$\sigma_{xy} = \frac{k_{txy}}{k_{fx} + k_{ix}}. \tag{40}$$

Scintillators are designed to be have the excitation energy of the first singlet π-electron state of the solute lower than that of the solvent, or $E_{1y} < E_{1x}$. The addition of a third component Z requires the calculation of the total quantum efficiency of energy transfer from Y to Z as

$$f_{xy} = \frac{a_{yz}(q_{0y})_0 + \sigma_{yz}[Z]}{1 + \sigma_{yz}[Z]}, \tag{41}$$

with σ_{yz} given by

$$\sigma_{yz} = \frac{k_{tyz}}{k_{fy} + k_{iy}}. \tag{42}$$

The overall efficiency is then

$$Q_z = C\frac{E_{pz}}{E_{1x}}f_{xy}f_{yz}q_{0z}, \tag{43}$$

with q_0z being the fluorescence quantum efficiency of Z defined by

$$(q_{0z})_0 = \frac{k_{fz}}{k_{fz} + k_{iz}}, \tag{44}$$

and E_{pz} is defined by an equation similar to 31.

The absolute scintillation efficiency, S, can then be calculated by collecting equations 27 and 43 for the scintillator with two solute species,

$$S_z = PC\frac{E_{px}}{E_{1x}}f_{xy}f_{yz}q_{0z}. \tag{45}$$

94

Further, the number of fluorescence photons with an average energy E_p produced by a 1 MeV electron is

$$N_z = \frac{PC}{E_{1x}} f_{xy} f_{yz} q_{0z} \times 10^6,$$ (46)

with the value q_{0z} being

$$q_{0z} = \frac{k_{fz}}{k_{fz} + k_{iz} + k_{cz}[Z]} = \frac{(q_{0z})_0}{1 + \sigma_{cz}[Z]}.$$ (47)

Many solutes exhibit concentration quenching between the molecules of the solute, with the $k_{cy}[Y]$ being the concentration quenching rate parameter, and the value σ_{cz} being

$$\sigma_{cz} = \frac{k_{cz}}{k_{cz} + k_{iz}}.$$ (48)

Appendix C. Photon interaction with matter

Gamma radiation is difficult to measure directly, so typical measurement techniques use the effects of gamma interactions with matter. There are three major ways gamma radiation interacts with matter: photoelectric effect, Compton scattering, and pair production.

C.1 Probability Of An Interaction

The probability of an interaction occurring with columnated beam of photons over a distance d is given by

$$f = 1 - e^{-\mu d},\tag{49}$$

with μ being the linear attenuation coefficient in units of cm^{-1}. The terms that contribute to the linear attenuation coefficient are the linear photoelectric coefficient τ, Compton linear attenuation coefficient σ, and pair production attenuation coefficient χ, such that

$$\mu = \tau + \sigma + \chi \quad [cm^{-1}].\tag{50}$$

Each of the attenuation coefficients depend on energy of the photon and the material. The mass attenuation coefficient μ/ρ in units of cm^2/g, is the sum the individual contributions of the atomic cross-sections, $_a\sigma$, $_a\tau$, and $_a\chi$. The total mass attenuation coefficient is related to the total cross-section $_a\mu$ in $cm^2/atom$ by equation 51 [8].

$$\frac{\mu}{\rho} = \frac{N_0}{A}\,_a\mu\tag{51}$$

In Equation 51 N_0 is Avogadro's number, and A is the atomic weight of the material. If the material is a mixture of several components, the mass attenuation coefficient is the sum of weighted mass attenuation coefficients as in Equation 52.

$$\frac{\mu}{\rho} = \frac{\mu_1}{\rho_1}w_1 + \frac{\mu_2}{\rho_2}w_2 + \cdots + \frac{\mu_n}{\rho_n}w_n\tag{52}$$

where w_1 is the weight fraction of the element in the compound or mixture.

C.2   The Photoelectric Effect

The photoelectric effect is dominant below 250 keV, but continues to be influential up to 2 MeV. It occurs by the interaction of the gamma-ray photons primarily with a K shell electron [21]. All of the gamma ray's energy is transferred to the electron. If the incident gamma ray carried more energy than the electron binding energy, E_b, the interaction will result in the emission of a *photoelectron*. The energy of the photoelectron, E_{e-} is equal to that of the photon, $h\nu$, less the electron binding energy.

$$E_{e-} = h\nu - E_b \tag{53}$$

The atom recoils because momentum is conserved, but the recoil energy is quite small and can be neglected with little error. As the photoelectron is ejected, a vacancy is produced in the electron shell which is then filled with an electron from a higher level shell. The conservation of energy requires that the transition from the higher to the lower energy shell is accompanied by an equivalent release of energy. Energy released from the transition can be either in the form of a characteristic x-ray or an Auger electron. The x-ray is frequently reabsorbed through interactions with nearby atoms, but, occasionally the x-ray escapes the material. The Auger electron deposits its energy in the material because it has a very short range in the material.

The probability of photoelectric absorption varies approximately with the atomic number, Z, of the material, and inversely with the energy of the incident photon, $h\nu$. An approximation of the relationship for the partial mass attenuation coefficient is

$$\frac{\tau}{\rho} = \frac{N_0}{AE^p}CZ^n \quad [cm^2/g], \tag{54}$$

where E is the Energy of the photon, C is a constant of correlation, N_0 is Avogadro's number, and A is the atomic weight of the material. The value of n can

have values from 4 to 5 [21]; p decreases with increasing E between 3 and 1 [8]. The relation between atomic number and mass attenuation coefficient implies that materials with high atomic weights are effective at stopping photons, but are less effective at stopping them as the energy of the photon increases.

C.3 Compton Scattering

A second way that gamma radiation interacts with matter is Compton scattering. The incident gamma photon interacts with an electron in a material. The photon changes direction and causes the electron to scatter. In the interaction the photon can transfer substantial fractions of its energy to the scattered electron. If the electron is assumed to be initially at rest, the energy of the scattered photon $h\nu'$ is related to the angle of photon scatter by

$$h\nu' = \frac{h\nu}{1 + \frac{h\nu}{m_0 c^2}(1 - \cos\theta)}, \tag{55}$$

where θ is the angle of photon scatter and $m_0 c^2$ is the rest-mass of an electron $\simeq 0.511 MeV$ [21], and $h\nu$ is the energy of the photon. The energy transfered to the electron is then

$$E_{e^-} = h\nu - h\nu' = h\nu \left(\frac{(2h\nu/m_0 c^2)(1 - \cos\theta)}{1 + (2h\nu/m_0 c^2)(1 - \cos\theta)} \right). \tag{56}$$

The maximum energy of the Compton-scattered electron then occurs when $\theta = 0$ or $\theta = \pi$, which yields an expression for the maximum energy transfer to the electron

$$E_{max,e^-} = h\nu - h\nu' = h\nu \left(\frac{2h\nu/m_0 c^2}{1 + 2h\nu/m_0 c^2} \right). \tag{57}$$

The maximum energy of a Compton-scattered electron marks a key feature in many pulse-height spectra, the Compton-edge. Though commonly referred to as the Compton-edge, the electron binding energy results in a rounding off of the edge, and

a slope instead of an abrupt drop off. Often it is convenient to reference the location of the Compton-edge by its offset from the full energy peak, it is given by Equation 58.

$$E_c = h\nu - E_{e^-}|_{\theta=\pi} = \frac{h\nu}{1 + 2h\nu/m_0 c^2} \tag{58}$$

Since the interaction is between the photon and an electron, an abundance of electrons increases the probability of a Compton scatter event. This relationship is expressed in the form of the mass attenuation coefficient as

$$\frac{\sigma}{\rho} = N_0 \frac{Z}{A} \sigma_c \quad [cm^2/g], \tag{59}$$

where σ_c is the sum of the Compton absorption and Compton scattering cross-section. The mass attenuation cross-section does not show significant variation with material because the relationship Z/A is approximately 0.45 for all elements other than hydrogen.

The Klein-Nishina formula relates the probability of Compton-scatter to a particular angle. The probability of a photon absorption can be determined through the integration of the Klien-Nishina formula over all angles to yield Equation 60,

$$\sigma_c = \frac{\pi r_0^2}{\alpha} \left\{ \left[1 - \frac{2(\alpha+1)}{\alpha^2} \right] ln(2\alpha+1) + \frac{1}{2} + \frac{4}{\alpha} - \frac{1}{2(2\alpha+1)^2} \right\} \tag{60}$$

where the *classical electron radius*, $r_0 = e^2/4\pi\epsilon_0 mc^2 = 2.818$ fm, and α is the photon energy in terms of the electron rest mass, $\alpha = E_\gamma/mc^2$ [22].

C.4 Pair Production

A third type of interaction is pair production. Pair Production can occur when an incident photon inside the coulomb field of the nucleus and energy has more than 1.02 MeV [21]. The photon is completely absorbed, and results in a positron and electron plus kinetic energy. The kinetic energy of the newly created particles is

correlated to the initial energy of the photon by

$$E_\gamma = T_- + m_0c^2 + T_+ + m_0c^2 \tag{61}$$

where m_0c^2 is the rest mass of an electron, $\simeq 0.511MeV$, and T_- and T_+ represents the kinetic energy of the electron and positron respectively [22]. As energy increases above the 1.02 MeV minimum, the probability of pair production increases. However pair production only becomes a significant part of the total absorption when the energy of the photon gets to be two or three MeV, and it becomes the dominant mode of interaction when photon energies exceed 5 MeV.

Since the pair production mass attenuation coefficient is proportional to Z^2/A, the pair production mass attenuation coefficient of any material can be determined through knowledge of a known mass attenuation coefficient, such as lead [8].

$$\frac{\chi}{\rho} = \frac{A_n}{A} \left(\frac{Z}{Z_n}\right)^2 \left(\frac{\chi}{\rho}\right)_n \frac{Z^2}{A} \tag{62}$$

C.5 Secondary Interactions

The combined effect of the three primary interactions produce electrons. As electrons travel through matter they loose energy as they change directions or collide with other particles. The energy loss per unit path length of electrons is described by the Bethe formula, Equation 63, with the subscripts c and r for collision and radiation loss respectively [22].

$$\frac{dE}{dx} = \left(\frac{dE}{dx}\right)_c + \left(\frac{dE}{dx}\right)_r \tag{63}$$

100

$$\left(\frac{dE}{dx}\right)_c = \left(\frac{e^2}{4\pi\epsilon_0}\right)\frac{2\pi N_0 Z\rho}{mc^2\beta^2 A}\left[ln\frac{T(T+mc^2)\beta^2}{2I^2mc^2} + (1-\beta^2)\right.$$
$$\left. -(2\sqrt{1-\beta^2} - 1 + \beta^2)ln2 + \frac{1}{8}(1-\sqrt{1-\beta^2})^2\right] \qquad (64)$$

$$\left(\frac{dE}{dx}\right)_r = \left(\frac{e^2}{4\pi\epsilon_0}\right)\frac{Z^2 N_0(T+mc^2)\rho}{137m^2c^4 A}\left[4ln\frac{2(T+mc^2)\beta^2}{mc^2} - \frac{4}{3}\right] \qquad (65)$$

In Equations 63, 64 and 65, $\beta = v/c$, e is the electric charge of an electron and m is the mass of an electron. The empirical constant, I, is the average excitation energy for the atomic electrons with order of magnitude 10Z.

Appendix D. Experimental Settings

Table 16:   The settings for the spectroscopy circuit

Parameter	Value
High Voltage Supply	
HV	-1500 V
Pre Amplifier	
Input Capacitance	0 pf
Amplifier	
Fine Gain	10.40
Course Gain	200
Pulse Shaping Time	$0.25\mu s$
Base Line Reject	Auto

Appendix E. Equipment

Table 17:   Equipment list

Item	Manufacturer	Model	ID Number
Photomultiplier Tube	Hamamatsu	R329-02	RC4765
PMT Base	Ortec	265	1976
*Photomultiplier Tube	RCA	8575	P39014
*PMT Base	Ortec	265	2086
*High Voltage Supply	Ortec	478	41982
High Voltage Supply	Ortec	478	041980
Preamplifier	Ortec	113	7950
*Preamplifier	Ortec	113	7140
*Amplifier	Ortec	572A	253A
Amplifier	Ortec	572A	325
Multi-Channel Analyzer	Ortec	926	06171866F
Oscilloscope	Tektronix	TDS5104D	B023145

*System receiving signal from PMT1
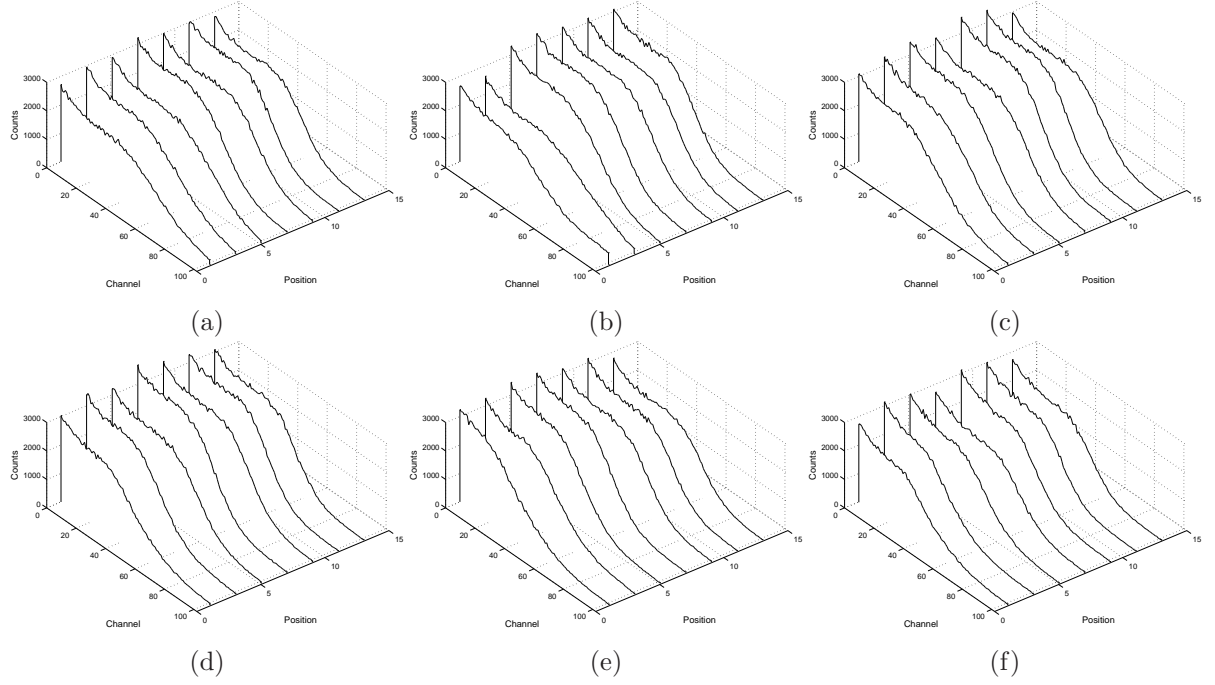
Figure 28:   Stacked spectrum from factory wrapped EJ-200 scintillator panel for each position in row: (a) 1.24 in from the bottom; (b) 3.24 in from the bottom; (c) 5.24 in from the bottom; (d) 7.24 in from the bottom; (e) 9.24 in from the bottom; and, (f) 11.24 in from the bottom.
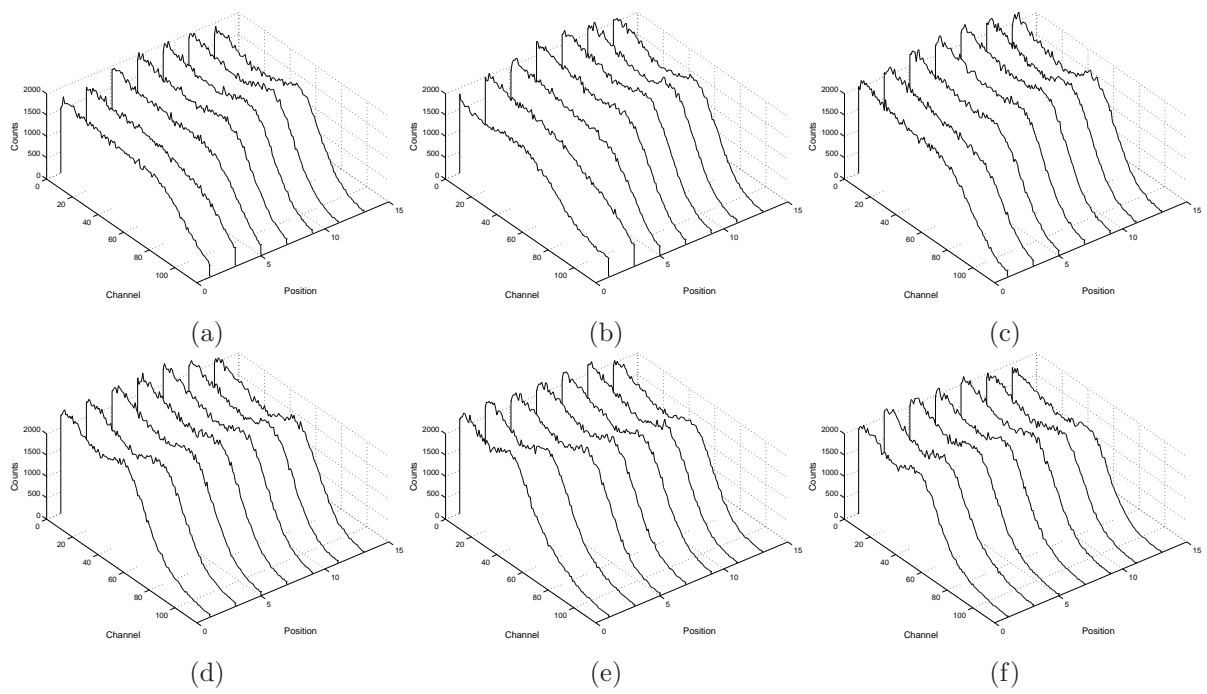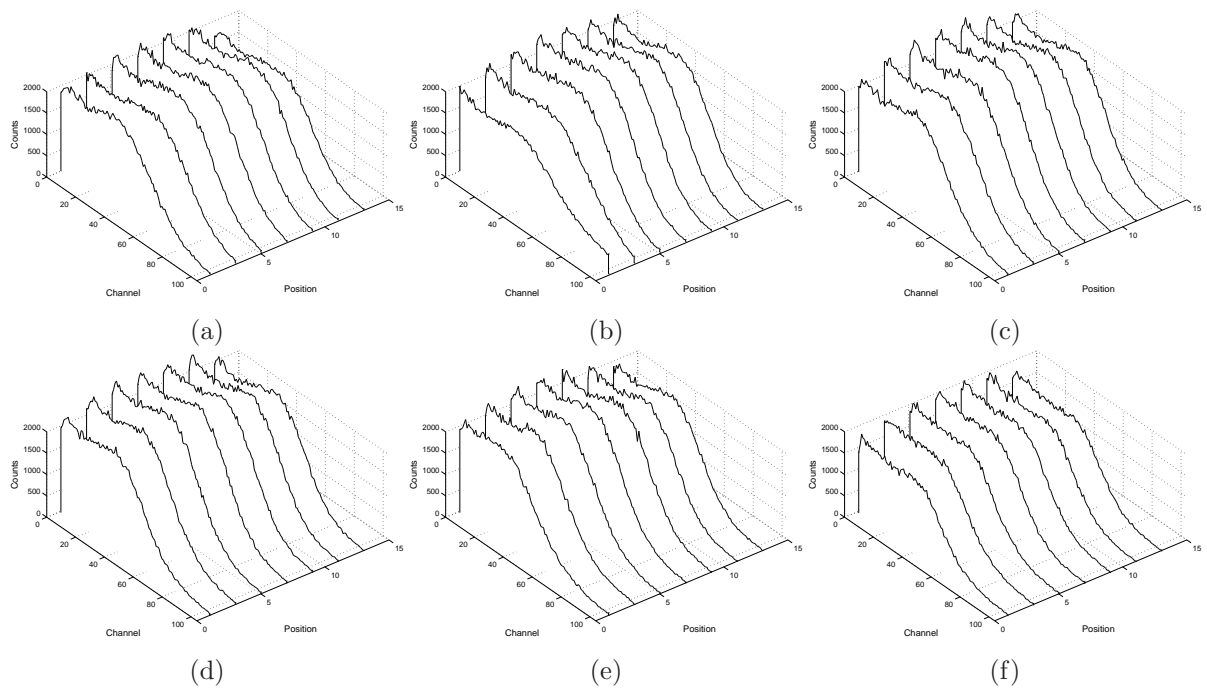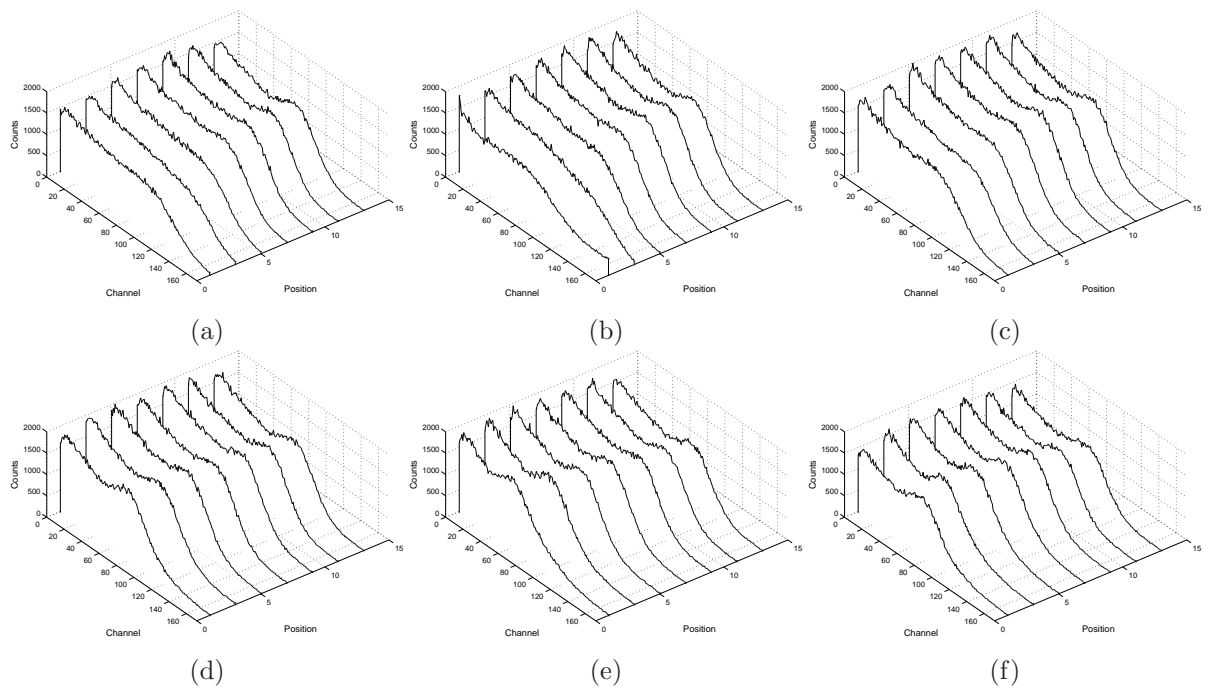
Figure 29: Stacked spectrum from researcher wrapped EJ-200 scintillator panel for each position in row: (a) 1.24 in from the bottom; (b) 3.24 in from the bottom; (c) 5.24 in from the bottom; (d) 7.24 in from the bottom; (e) 9.24 in from the bottom; and, (f) 11.24 in from the bottom.

(a) (b) (c)

(d) (e) (f)

Figure 30:   Stacked spectrum from factory wrapped BC-408 scintillator panel for each position in row: (a) 1.24 in from the bottom; (b) 3.24 in from the bottom; (c) 5.24 in from the bottom; (d) 7.24 in from the bottom; (e) 9.24 in from the bottom; and, (f) 11.24 in from the bottom.

(a) (b) (c)

(d) (e) (f)

Figure 31:   Stacked spectrum from researcher wrapped BC-408 scintillator panel for each position in row: (a) 1.24 in from the bottom; (b) 3.24 in from the bottom; (c) 5.24 in from the bottom; (d) 7.24 in from the bottom; (e) 9.24 in from the bottom; and, (f) 11.24 in from the bottom.

107

Appendix G. Simulation Pulse Height Spectra

The results for the simulations performed with the collimator and gamma source placed at each of the seven positions from one to thirteen inches from the PMT face. The position of the collimator shown in figure 8 corresponds to placing the collimator and source thirteen inches from the PMT face.
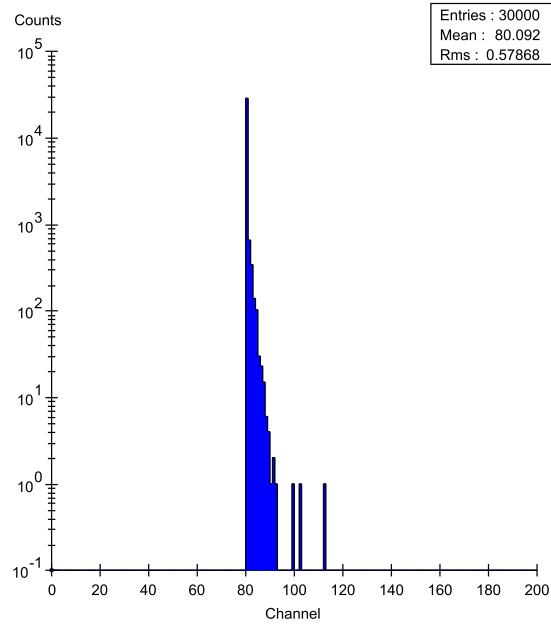
Figure 32:   A visualization showing the pulse height spectrum generated with the gun and collimator centered 1 in from the PMT.
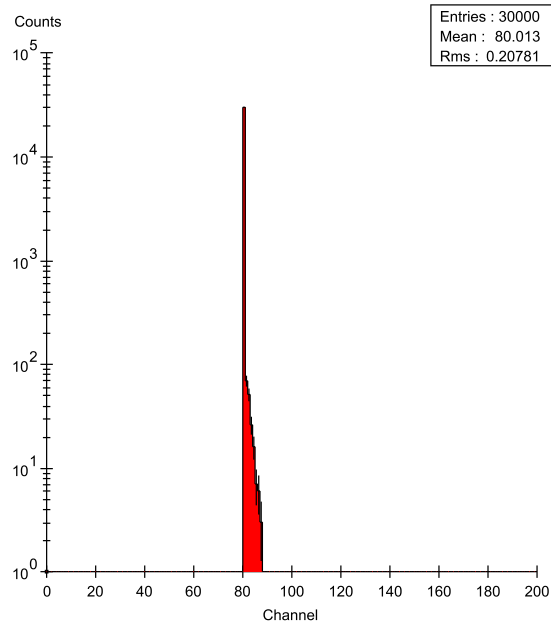
Figure 33: A visualization showing the pulse height spectrum generated with the gun and collimator centered 3 in from the PMT.
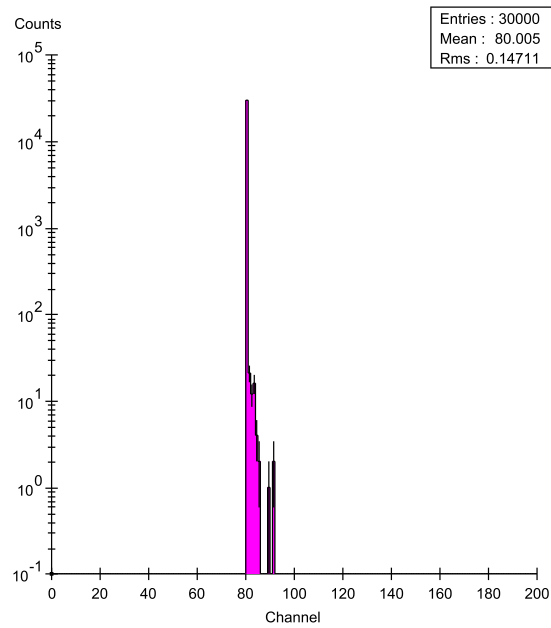

Figure 34: A visualization showing the pulse height spectrum generated with the gun and collimator centered 5 in from the PMT.
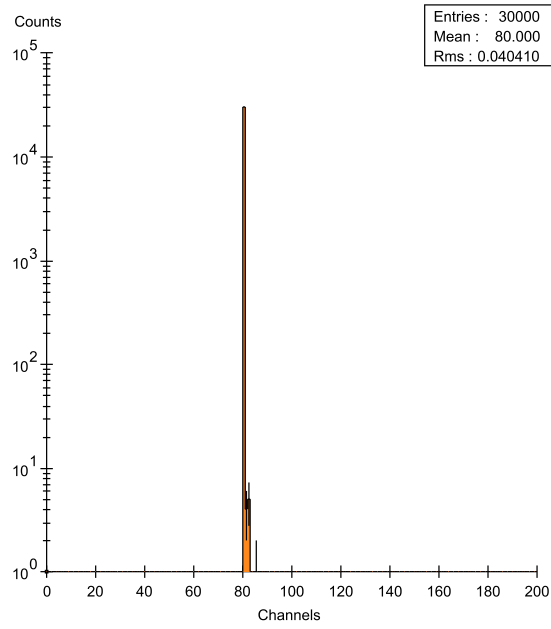
Figure 35: A visualization showing the pulse height spectrum generated with the gun and collimator centered 9 in from the PMT.
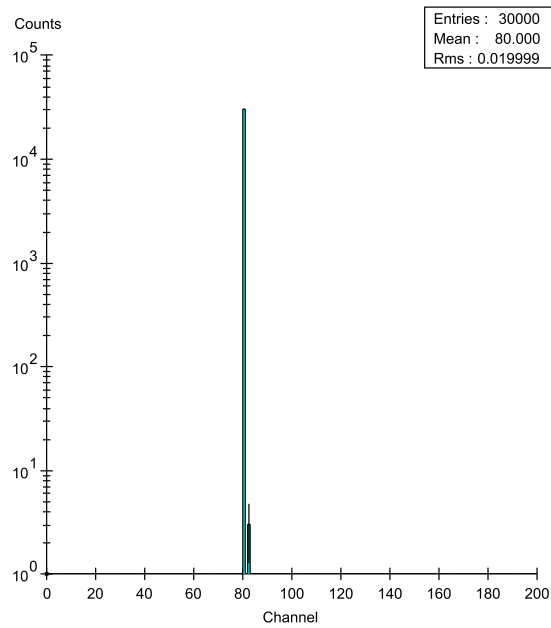

Figure 36: A visualization showing the pulse height spectrum generated with the gun and collimator centered 11 in from the PMT.
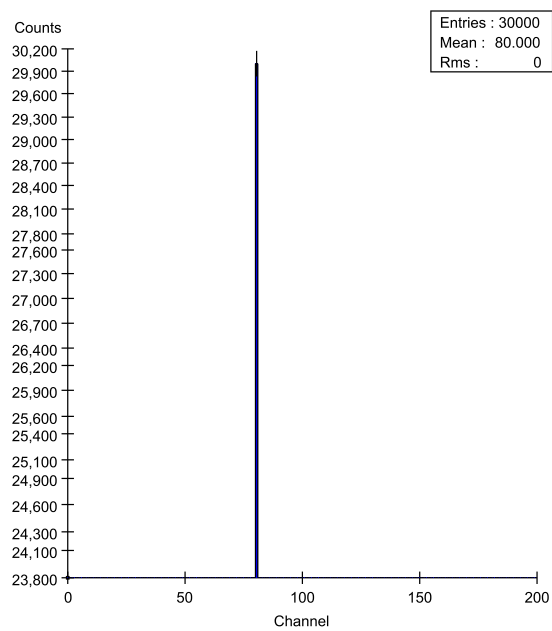
Figure 37: A visualization showing the pulse height spectrum generated with the gun and collimator centered 13 in from the PMT.

Appendix H. Component Absorption and Emission Spectra

The absorption and emission spectrum identified in Figures 38, 39, and 40, are taken from Berlman's Handbook of Fluorescence Spectra of Aromatic Molecules [7].
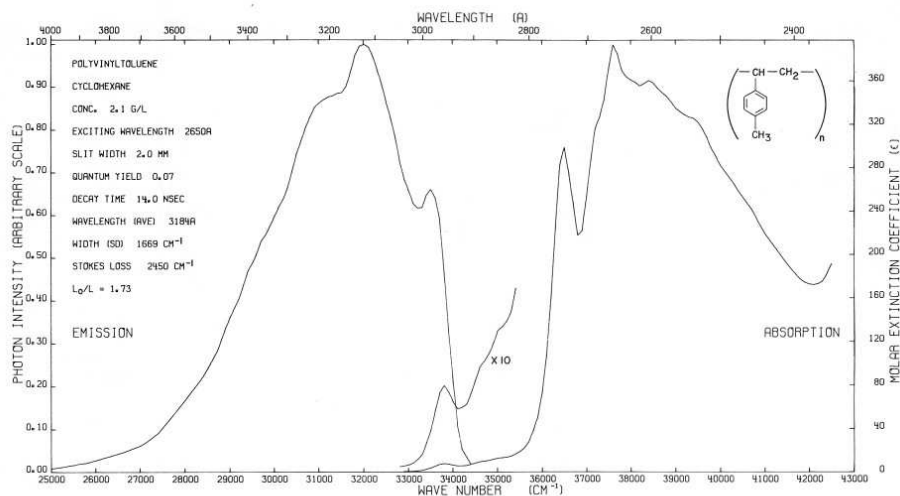

Figure 38:   Absorption and emission spectra from polyvinyl toluene.
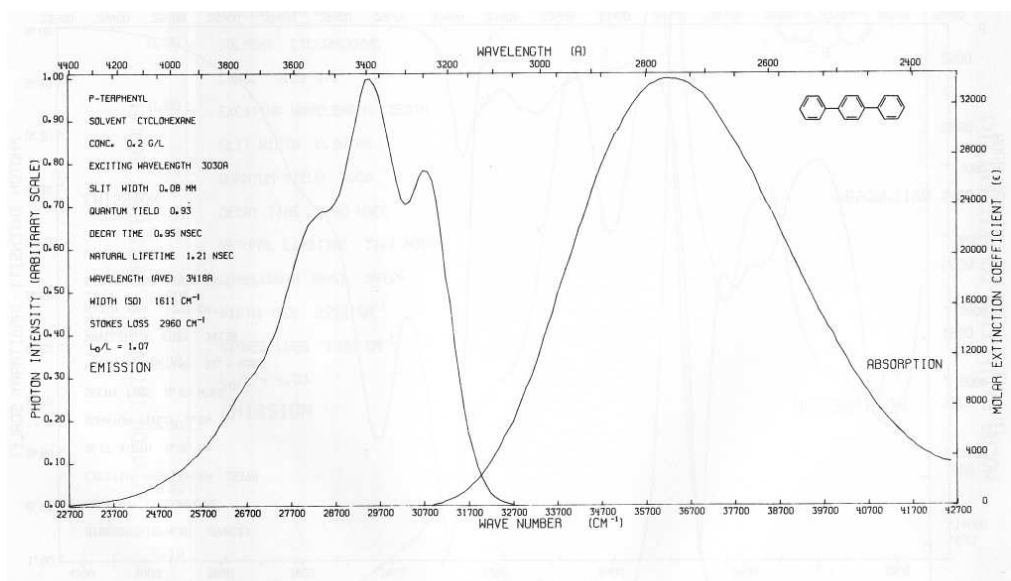
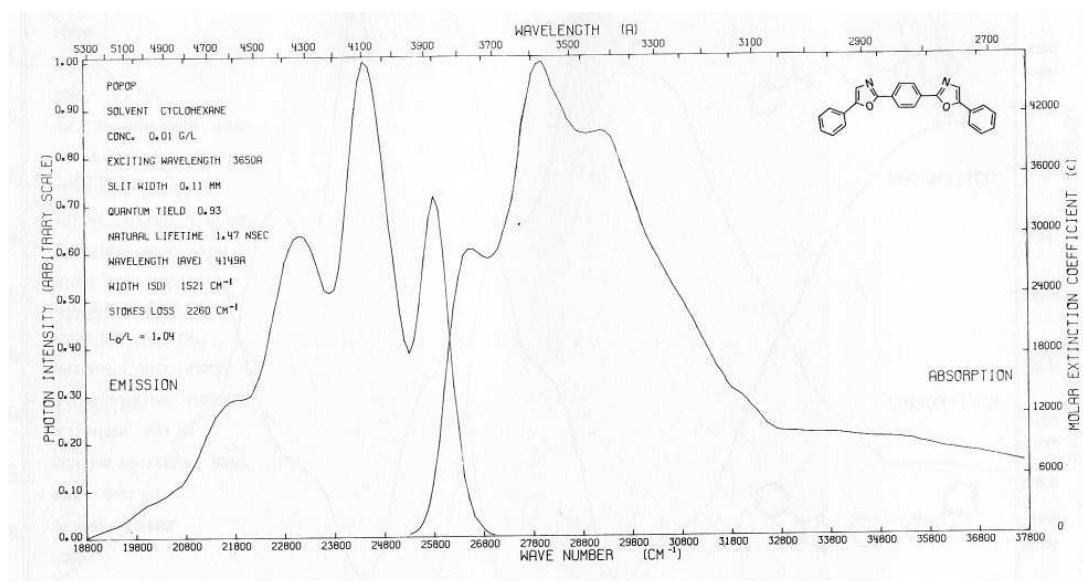Figure 39:   Absorption and emission spectra from p-terphenyl.

Figure 40:   Absorption and emission spectra from POPOP.

Bibliography

1. "Geant4 User Forum."
   http://geant4-hn.slac.stanford.edu:5090/Geant4-HyperNews/index.

2. "Geant4 User Guide." http://geant4.cern.ch/support/userdocuments.shtml.

3. "Particle Data Group." http://pdg.lbl.gov/.

4. "Tabls of X-Ray Mass Attenuation Coefficients and Mass Energy-Absorption
   Coefficients." http://physics.nist.gov/PhysRefData/XrayMassCoef/cover.html.

5. "About Geant4." http://geant4.cern.ch/support/about.shtml, 8 July 2006.

6. Albrecht, M., et al. *Scintillators and Wavelength Shifters for the Detection of
   Ionizing Radiation*. Technical Report, Notre Dame, Indiana 46556, USA:
   Department of Phhysics and QarkNet Center.

7. Berlman, Isadore B. *Handbook of Fluorscence Spectra of Aromatic Molecules*.
   New York, NY: Achademic Press, 1971.

8. Birks, J. B. *The Theory and Practice of Scintillation Counting*. New York,
   NY: The Macmillan Company, 1964.

9. Campbell, I. H. and B. K. Crone. "Efficient plastic scintillators utilizing
   phosphorescent dopants," *Applied Physics Letters*, **90**:647–651 (January 2007).

10. Crystals, Saint-Gobain, "Premium Plastic Scintillators."
    http://www.detectors.saint-gobain.com, January 2005.

11. Czjkowski, Carl. *Technological Challenges in Radiological Detection in
    Homeland Security Applications*. Technical Report, P.O. Box 5000, Bldg 197C,
    Upton, NY 11973-5000: Brookhaven National Laboratory.

12. Dyshkant, A., et al. "Towards a Scintillator Based Digital Hadron Calorimeter
    for Linear Collider Detector," *IEEE* (Septermber 2004).

13. Ely, J. H., et al. "Discrimination of Naturally Occurring Radioactive Material
    in Plastic Scintillator Material,"

14. Eric, Christian, "TIGER Questions and Answers about the TIGER
    Instrument." http://tiger.gsfc.nasa.gov/qa-tiger.html, 6 January 2004.

15. Forster, Th. and Z. Naturfosch. "Organic Scintillators," *European Physical
    Jounal*, **4a** (1949).

16. Geoghegan, Tom. "The mystery of Litvinenko's death," *BBC News*, 647–651
    (24 November 2006).

17. Gobain, Saint, "BC-408: Premium Plastic Scintillators." http://www.detectors.saint-gobin.com, January 2007.

18. Hall, A. W. and G. R. Friggens. *Evaluating Plastic Scintillators for Detecting Prompt Gamma Rays in Continuous Analysis of Bulk Materials*. Report of Investigations 7920, Morgantown, W. Va: Morgatown Energy Research Center, 1974.

19. Johnson, K. F. "Organic Scintillators," *European Physical Jounal*, **C15** (2000).

20. Jordan, D. V., et al. *Progress Report on the Advanced Large-Area Plastic Scintillators(ALPS) Project*. Contract DE-AC06-76RL01830, Richland, Washington: Pacific Northwest National Laboratory, May 2003.

21. Knoll, G.F. *Radiation detection and Measurement.*. John Wilsey & Sons, 2000.

22. Krane, Kenneth S. *Intruductory Nuclear Physics*. John Wilsey & Sons, 1988.

23. Li, Zao, et al. "Properties of Plastic Scintillators After Irradiation," *Nuclear Instruments and Measurments in Physics Research A*, **552** (July 2005).

24. LoPresti, Charles A., et al. "Baseline suppression of vehicle portal monitor gamma count profiles: A characterization study,"

25. Lumb, Michael D. *Luminescence Spectroscopy*. New York: Academic Press, 1978.

26. Madey, R., et al. "Large volume neutron detectors with sub-nanosecond time dispersions,"

27. Miyajima, M., et al. "Number of Scintillation Photons Emitted in NaI(Tl) and Plastic Scintillaotrs by Gamma-Rays," *Nuclear Instruments and Methods in Physics Research*

28. Mukhopadhyay, Sanjoy. *Plastic gamma sensors: an application in detection of radioisotopes*. Technical Report, P.O. Box 98521-8521, M/S RSL-11 Las Vegas, NV 89193-8521: Bechtel Nevada.

29. Neal, J. S., et al. *Large Plastic Scintillation for the Nuclear Materials Identification System*. Hosted Paper, http://www.ornl.gov/ webworks/cppr/y2001/pres/120726.pdf, P.O. Box 2008, Oak Ridge, Tennessee 37831-6010, USA: Oak Ridge National Laboratory.

30. Onge, R. St., et al. "Organic-Scintillator Pulse-Shape Discrimination Signatures Associated With High-Eergy Neutrons," *Nuclear Instruments and Methods in Physics Research*, **126**:391 (1975).

31. Pope, James E. *Construction and Testing of a Neutron and Gamma Spectrometry System using Pulse Shape Discrimination with an Organic Scintillator*. MS thesis, AFIT/GNE/ENP/93M-6, Air Force Institute of Technolgy, Wright-Patterson AFB OH, March 1993.

32. Sciciliano, E.R., et al. "Compparison of PVT and NaI(Tl) scintillators for vehicle protal monitor applications," *Nuclear Instruments and Methods in Physics Research A*, **550** (2005).

33. Swank, Robert K. and Warren L. Buck. "The Scintillation Process in Plastic Solid Solutions," *Physics Review*, **91**(4):927–933 (Aug 1953).

34. TECHNOLOGY, ELJEN, "Plastic Scintillators." http://www.eljentechnology.com/products.html-Plastic2006.

35. Torrisi, F. D. "Development of Organic Scintillators," *Nuclear Instruments and Methods*, **162** (1979).

36. Torrisi, Lorenzo. "Radiation damage in polyvinyltoluene (PVT)," *Radiation Physics and Chemistry*, **63** (2002).

37. Tsirlin, Yu. A., et al. "Light yield of plastic scintillators in relation to the energy of external electrons," *Zhurnal Prikladnoi Spektroskopii*, **3** (1965).

38. Williams, J. F., et al. "Plastic scintillator response to low-energy photons,"

REPORT DOCUMENTATION PAGE

The public reporting burden for this collection of information is estimated to average 1 hour per response, including the time for reviewing instructions, searching existing data sources, gathering and maintaining the data needed, and completing and reviewing the collection of information. Send comments regarding this burden estimate or any other aspect of this collection of information, including suggestions for reducing the burden, to the Department of Defense, Executive Services and Communications Directorate (0704-0188). Respondents should be aware that notwithstanding any other provision of law, no person shall be subject to any penalty for failing to comply with a collection of information if it does not display a currently valid OMB control number.
PLEASE DO NOT RETURN YOUR FORM TO THE ABOVE ORGANIZATION.

1. REPORT DATE *(DD-MM-YYYY)*	2. REPORT TYPE	3. DATES COVERED *(From - To)*

4. TITLE AND SUBTITLE	5a. CONTRACT NUMBER
	5b. GRANT NUMBER
	5c. PROGRAM ELEMENT NUMBER

6. AUTHOR(S)	5d. PROJECT NUMBER
	5e. TASK NUMBER
	5f. WORK UNIT NUMBER

7. PERFORMING ORGANIZATION NAME(S) AND ADDRESS(ES)	8. PERFORMING ORGANIZATION REPORT NUMBER

9. SPONSORING/MONITORING AGENCY NAME(S) AND ADDRESS(ES)	10. SPONSOR/MONITOR'S ACRONYM(S)
	11. SPONSOR/MONITOR'S REPORT NUMBER(S)

12. DISTRIBUTION/AVAILABILITY STATEMENT

13. SUPPLEMENTARY NOTES

14. ABSTRACT

15. SUBJECT TERMS

16. SECURITY CLASSIFICATION OF:			17. LIMITATION OF ABSTRACT	18. NUMBER OF PAGES	19a. NAME OF RESPONSIBLE PERSON
a. REPORT	b. ABSTRACT	c. THIS PAGE			
					19b. TELEPHONE NUMBER *(Include area code)*